INFORMATION TO USERS

This manuscript has been reproduced from the microfilm master. UMI films the text directly from the original or copy submitted. Thus, some thesis and dissertation copies are in typewriter face, while others may be from any type of computer printer.

The quality of this reproduction is dependent upon the quality of the copy submitted. Broken or indistinct print, colored or poor quality illustrations and photographs, print bleedthrough, substandard margins, and improper alignment can adversely affect reproduction.

In the unlikely event that the author did not send UMI a complete manuscript and there are missing pages, these will be noted. Also, if unauthorized copyright material had to be removed, a note will indicate the deletion.

Oversize materials (e.g., maps, drawings, charts) are reproduced by sectioning the original, beginning at the upper left-hand corner and continuing from left to right in equal sections with small overlaps. Each original is also photographed in one exposure and is included in reduced form at the back of the book.

Photographs included in the original manuscript have been reproduced xerographically in this copy. Higher quality 6" x 9" black and white photographic prints are available for any photographs or illustrations appearing in this copy for an additional charge. Contact UMI directly to order.

UMI

A Bell & Howell Information Company
300 North Zeeb Road, Ann Arbor, MI 48106-1346 USA
313/761-4700 800/521-0600

EXPERIMENTAL STUDY OF THE LIQUID-GLASS TRANSITION IN PROPYLENE CARBONATE

by

Weimin Du

A dissertation submitted to the Graduate Faculty in Physics in partial
fulfillment of the requirements for the degree of Doctor of Philosophy

The City University of New York.

1996

UMI
300 North Zeeb Road
Ann Arbor, MI 48103

This manuscript has been read and accepted for the Graduate Faculty in Physics in satisfaction of the dissertation requirement for the degree of Doctor of Philosophy.

Dec 18, 1995
Date

Chair of Examining Committee

Jan 4, 1996
Date

Joseph B. Krieger
Executive Officer

Joseph L. Birman

Steven G. Greenbaum

Frederick W. Smith

Jean Toulouse

Supervisory Committee

The City University of New York

ABSTRACT

EXPERIMENTAL STUDY OF THE LIQUID-GLASS TRANSITION IN PROPYLENE CARBONATE

by

Weimin Du

Advisor: Professor Herman Z. Cummins

Depolarized light-scattering spectra of propylene carbonate were obtained in the frequency range of 0.2 GHz to 4 GHz at temperatures in the liquid-glass transition region. Analysis of the resulting susceptibility spectra revealed reasonable agreement with the predictions of the idealized mode coupling theory. An extended mode coupling theory analysis corroborated and improved the results obtained with the idealized version. Polarized Brillouin spectra were also obtained, and were analyzed with generalized hydrodynamics. The results indicate that the Cole-Davidson function is not an adequate model for structural relaxation. A simultaneous photon correlation measurement and dielectric susceptibility measurement were carried out on salol to study the α-relaxation time-scale universality. The result shows that the relaxation times determined from these two techniques have similar temperature dependence, differing only by a constant factor.

ACKNOWLEDGMENTS

First, I want to express my deep gratitude to my adviser Professor Herman Z. Cummins for his encouragement, practical tutelage, patient guidance, and continued support throughout my research at the City College.

I express my grateful acknowledgment to Professor Wolfgang Götze and Professor Robert M. Pick in developing crucial theoretical aspects of this research and for their invaluable guidance, suggestions, and discussions.

I thank Professor Jean Toulouse for letting me to use his lab and for his guidance in the collaboration for part of this research. I thank the other members of my thesis committee, Professor Joseph L. Birman, Professor Steven G. Greenbaum, and Professor Frederick W. Smith for their guidance and help.

I gratefully thank Dr. Gen. Li for his generous help on experiments and benefice discussions during these years. I also thank Dr. Matthias Fuchs for providing his computer program and for his contributions on data fitting.

Thanks also go to the people in our group, Dr. Nongjian Tao, Dr. Xiaoke. Chen, Dr. Yoon-Hwae Hwang, Joel Hernandez, and Guoqing P. Shen for their friendly help and collaborations on these studies. I also thank Dr. Lee A Knauss, Dr. Catherine Dreyfus and our visitor Prof. A. Sakai for discussion and collaboration.

Many thanks to Tracy Turner and all the people in our pattern formation subgroup for their assistance, collaboration, and friendship that contribute a helpful and pleasant working environment in our Lab.

I thank the people in the Machine shop, Glass shop, and electronics shop for their professional help in construction and maintenance of our apparatus and equipment.

I also thank all my former advisors, teachers, and colleagues, my family and friends. Through their encouragement and help, they have contributed to this dissertation.

DEDICATION

I dedicate this thesis to my father,

my family,

and memorable friends.

TABLE OF CONTENTS

LIST OF TABLES

LIST OF FIGURES

I. INTRODUCTION

A. OVERVIEW OF THE LIQUID GLASS TRANSITION

1. Characteristics of the liquid-glass transition

a) Transition from liquid to glass and the viscosity

Many materials can be melted and then cooled below their bulk melting temperature Tm to form a glass, if the system is sufficiently complex or the cooling rate is fast enough to avoid crystallization. Both liquid and glass are amorphous in structure and lack long-range spatial order. The principal difference between them is in their viscosities. The viscosity presumably characterizes the structural relaxation process by which the local molecular organization reorganizes following a change of density or temperature. The calorimetric glass transition temperature T_g is conventionally defined by $h(T_g) = 10^{13}$ poise.

b) Vogel-Fulcher Law

From the Maxwell relation, $\tau=\eta/G_\infty$ (where G_∞ is the high-frequency shear modulus) the structural relaxation time τ is proportional to the viscosity η. The viscosity η or the relaxation time τ is generally found to depend on the temperature T in a non-Arrhenius fashion. The Vogel-Fulcher law $\eta(T) \propto \exp[B/(T-T_0)]$ is widely used, with B and T_0 as constants. The Arrhenius law $\eta(T) \propto \exp(E_A/T)$ is obtained from the Vogel-Fulcher law by setting $T_0=0$. E_A is the activation energy.

c) Angell plot and the fragility m

The famous "Angell plot", shown in Fig. 1.1, illustrates the concept of strong and fragile glasses.

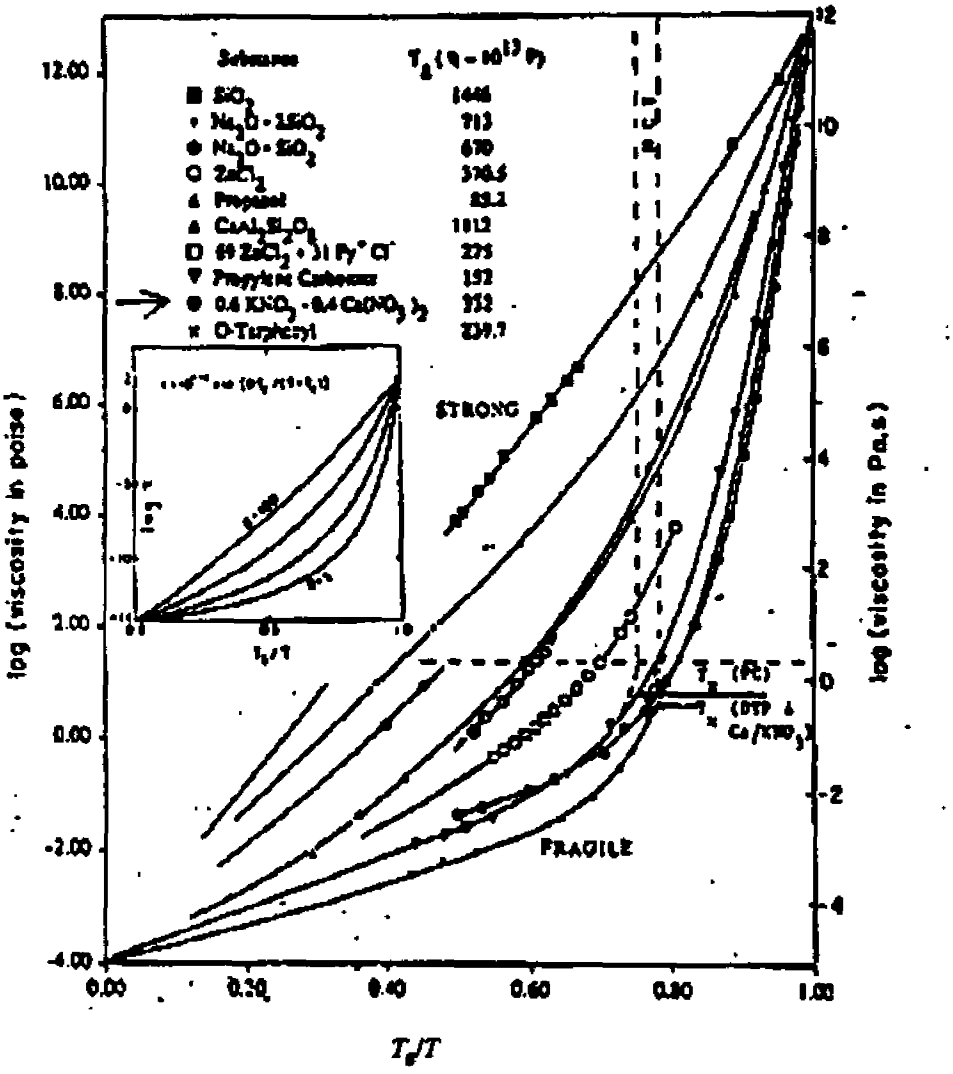

Fig. 1.1. Angell plot of the viscosity $\eta(T_g/T)$ as a function of T_g/T [1]. The η of strong glassforming materials follows the Arrhenius law, while the materials with the most non-Arrhenius behavior are the most fragile glassforming materials.

In the strong glassforming materials, such as SiO_2, the molecules are connected by a network of strong covalent bonds. In the fragile glassforming materials the interactions between particles are weak chemical bonds, such as the van der Waals interaction.

The departure from Arrhenius behavior is indicated by the fragility m, which is a convenient measurement to classify glassforming materials. m is defined as the initial slope of the viscosity (or relaxation time $<\tau>$) by Böhmer et al. [2]

$$\begin{aligned} m &= d \log <\eta> / d\,(T_g/T)\,|_{T=T_g} \\ &\propto d \log <\tau> / d\,(T_g/T)\,|_{T=T_g} \end{aligned} \tag{1.1}$$

and ranges from ~20 for strong glassformers like SiO_2 up to ~200 for the most fragile materials such as poly (vinyl chloride).

2. Traditional studies of LGT

a) Traditional studies of viscosity etc. and the question of T_g

Traditionally, investigations of the liquid-glass transition (LGT) concentrated on the vicinity of T_g to study the divergence of the shear and bulk viscosities [3]. Several theoretical models have been proposed [4]. Various thermodynamic quantities such as compressibility, specific heat [5], [6], and thermal expansion etc. were also studied. Anomalies in these quantities were observed [7].

These studies also found that T_g depends on the cooling rate, and the temperature at which anomalous behavior shows up depends on the duration of the experiments. The transition temperature in short time-duration measurements is higher than that found in long time-duration measurements. For these reasons the use of T_g to define the crossover of LGT cannot be justified.

The dynamic transition cannot be defined by an abrupt change of an order parameter at a transition temperature as in the case of crystallization, because of the lack of long range spatial order in the glass state. Furthermore, glasses are non-equilibrium amorphous solids; there is no precise distinction between the glassy state and the supercooled liquid state.

The central themes of most contemporary liquid-glass transition studies are (i) What is the detailed time dependence of structural relaxation functions? (ii) What is the specific signature of the LGT in the corresponding spectra, and what is their temperature dependence? (iii) What is the microscopic origin of the relaxation processes in supercooled liquids?

b) Dielectric and Brillouin scattering studies

Many early and recent studies of the relaxation dynamics of supercooled liquids employed dielectric susceptibility spectroscopy. The prominent feature found in these studies is a peak in the imaginary part of the susceptibility spectra $\chi''(\omega)$, called the α-relaxation (or primary relaxation) peak. In the supercooled temperature region, the α-peak frequency is much lower than the molecular vibrational modes, and is very sensitive to temperature. The peak width is usually considerably larger than the 1.14 decades predicted by the Debye model. This indicates that fluctuations in supercooled liquids decay nonexponentially. (It has also been suggested that the decay may be exponential, but inhomogeneous).

Numerous conventional Brillouin scattering studies of supercooled liquids have been reported in the past, with analyses based on the generalized hydrodynamic approach [8], [9]. In most cases, only the frequency shifts and linewidths of the Brillouin peaks were analyzed, while the additional information contained in the detailed spectral shape was ignored. Soltwisch et al. analyzed the full spectrum of $ZnCl_2$ which showed that generalized hydrodynamics can provide a reasonable fit to the complete experimental data [10].

However, until recently there was no generally accepted theoretical model to give a comprehensive and satisfactory description of the dynamical processes in supercooled liquids. The situation changed in 1984 with the appearance of the mode coupling theory (MCT).

B. INTRODUCTION TO MODE COUPLING THEORY AND ITS RECENT TESTS

1. Initial "Idealized" version of MCT and its predictions

The appearance of two publications in 1984, by Bengtzelius et al. [11] and by Leutheusser [12], marks the beginning of research on MCT as a theory of the LGT. In the

MCT, the system is described by a set of dynamical equations for the density fluctuation modes. The nonlinear effects of mode coupling and retardation in these equations results in a dynamic phase transition from an ergodic liquid-like state to a nonergodic glass-like state at a crossover temperature T_c. Around this singularity, the spectra change rapidly from ones that can be considered as typical for a normal liquid to ones which can be considered as typical for a glass.

The MCT predictions include (i) the development of a two-step β-relaxation process near T_c (power-law critical decay of the fast β-relaxation and slower von Schweidler power-law decay as the beginning of the α-relaxation); (ii) structural arrest at the critical temperature T_c with a non-zero infinite-time asymptote of the density fluctuation correlation function: $\Phi_q(t \rightarrow \infty) = f_q^c$; (iii) scaling behavior of α-relaxation above T_c; (iv) factorization of t- and q- dependence in the β-relaxation region, and (v) scaling behavior of β-relaxation both above and below T_c. These detailed predictions stimulated much of the recent attempts to experimentally test this theory.

2. Recent tests of MCT

a) Neutron scattering

Mezei, Knaak, and Farago carried out neutron spin-echo and Time-of-flight (TOF) experiments on CKN in 1987 [13]. The result shows the dynamics of the relaxation process extending over nearly three decades. The TOF spectra follow the MCT critical decay law

$S(q,\omega) \propto \omega^{-(1-a)}$ with $a = 0.3$. The spin-echo data show that for $t/\tau_\alpha \ll 1$ the von Schweidler law is a good approximation to the α-relaxation. The middle region of $\chi''(\omega)$ from the combined data is higher than that obtained by simple superposition of the α-peak with the liquid excitation peak, indicating the existence of the intermediate β-relaxation process.

b) Depolarized light scattering

Dynamic light-scattering spectroscopy has also provided a powerful approach to study the supercooled liquids. Experiments on CKN [14] and salol [15] illustrated this clearly. Data collected by using a Tandem FP interferometer and a Raman spectrometer are spliced together to form large frequency range spectra spanning over 4 decades which can reveal the full form of the spectra. A set of such spectra for temperatures from above T_m to lower than T_g were obtained, which showed the evolution of the system dynamics from liquid state to glass state. Fitting the susceptibility spectra with predictions of MCT revealed the two-step relaxation process near the transition, confirmed the power law predictions, and determined the crossover temperature T_c.

c) Brillouin light scattering

MCT suggests that the transition singularity could be studied by generalized hydrodynamic theory [16]. Three experiments exploiting this approach have been previously reported: Elmroth et al. [17] studied PC. The T_c they determined was not consistent with neutron and viscosity results. Dreyfus et al. [18] studied salol. The sound velocity C_0 was determined independently from ultrasonic data and the anisotropic contributions were subtracted. Their experiment produced a T_c in reasonable agreement with that found from the depolarized light scattering experiments [15]. In the CKN experiment of Li et al. [19], a memory function was constructed which includes the full relaxation dynamics. The T_c determined from this study was also consistent with other determinations.

d) Viscosity test of power law

The primary relaxation times τ_α of some materials derived from early viscosity and dielectric measurements were reexamined by fitting with the power-law prediction of MCT [20]. When experimental data were analyzed this way, it was found that such power-law behavior does occur, but the resulting T_c occurs well above the calorimetric glass transition temperature T_g. In many cases, the estimated T_cs agree with the results from neutron scattering and depolarized light scattering.

The outcomes of these studies have stimulated much of the current interest to further test the predictions of MCT. The extended version of MCT also includes hopping effects, which results in a transition region between the liquid state and glass state. This prediction has been tested so far only on CKN and salol [21]. An extended MCT analysis of PC data will be presented in this thesis.

C. EXPERIMENTAL STUDIES OF PROPYLENE CARBONATE (PC)

1. Propylene Carbonate

a) Reasons for studying PC

The reasons for selecting PC for this study are the following.

MCT is a theory of the dynamics of weakly interacting glassforming materials. It has been found that PC is a very fragile glassforming material [2], [22] (see Angell plot Fig.1.1) with m=104 and it thus is a suitable candidate to test the predictions of MCT. It is also a material which has been studied extensively so that a large mount of experimental PC data is available.

b) Structure and properties of PC

PC (4-methy-1,3-diaxolan-2-one, $C_4H_6O_3$) is a polar cyclic carbonate. It is a colorless liquid at room temperature and supercools easily [22]. Fig. 2 shows its structure. PC is a small asymmetric rotor molecule with the following physical and chemical properties. Its formula weight is 102.09 and specific gravity is 1.189. The glass transition temperature T_g, melting temperature T_m, and boiling temperature T_b are 160 °K, 218 °K, and 513 °K respectively. The vapor pressure is 0.13 mm at 20 °C. The Density of PC $\rho(T) = 1.541\text{-}1.148 \times 10^{-3}\ T$, was measured by Simeral and Amey [23]. They also found that the refractive index at the sodium D line is $n_D(T) = 1.5314\text{-}3.752 \times 10^{-4}\ T$.

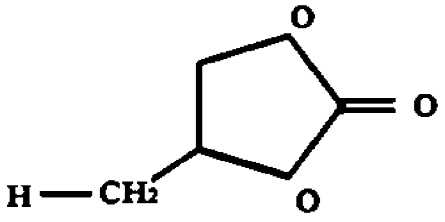

Fig. 1.2. The molecular structure of PC.

The supercooled temperature region of PC located between T_g=160 °K and T_m=218 °K is easily accessible using liquid nitrogen cooling with an optical access cryostat for light scattering studies.

PC's liquid-glass transition properties have been studied by viscosity measurements, dielectric susceptibility spectroscopy, neutron scattering, and conventional Brillouin light scattering etc..

2. Experimental studies of PC

a) Viscosity measurments by Bondeau and Huck, and the problem of T_0

Bondeau and Huck measured the viscosity of PC from 343 K to 157 K [24]. The data was fitted with a Vogel-Fulcher law in three different temperature intervals. They found that T_0 depends on the temperature range used in the fitting. This effect is frequently found for glassforming liquids with T_0 usually decreasing with decreasing T.

b) Dielectric measurements, the stretched relaxation process, evidence for the existence of a secondary relaxation process, and Schonhals's T_A.

Dielectric properties of PC have been reported extensively due to its importance in electrochemical and secondary battery applications. Most results were analyzed using Cole-Davidson or Cole-Cole models [25], [26], [27], [28], [22], [29]. In all cases the primary α-relaxation was found to be stretched, with reported values of the Kohlrausch exponent β_K (converted from the Cole-Davidson value β_{CD} by following the prescription of Lindsay and Patterson [30]) falling in the range from 0.61 to 0.93.

Payne et al. studied the dielectric properties of PC from 1 MHz to 9000 MHz. Dielectric constant and loss data at 78 °C were fitted with the Debye model. They concluded that the fitting parameter $\varepsilon_\infty = 10$ implies the existence of a second dispersion region at a frequency higher than 9000 MHz.

Johari et al. measured the dielectric loss factor $\Delta\tan\delta(T)$ of PC from 77 K to 175 K. A shoulder was observed at a temperature below T_g. Johari et al. consider it as evidence for the existence of a slow β-relaxation process in PC [26]. (This is different from the β-relaxation of MCT)

Submillimeter dielectric properties were obtained from far IR spectra by Masood et al [31]. The absorption coefficient from 10 to 70 cm^{-1} was calculated. Combined with dielectric data from 1MHz to 9000 MHz [28], the spectra clearly revealed the existence of a secondary relaxation process. This result confirmed the observation of Johari.

Recently, Schonhals et al. measured the complex dielectric function of PC over 15 decades in frequency to study the scaling of α-relaxation. [32] . They concluded that the temperature dependence of the α peak frequency f_p displays two dynamical regions separated by a crossover temperature T_A=216.6 K. At low temperature, f_p obeys the Vogel-Fulcher law. At sufficiently high temperature, f_p is governed by the Arrhenius law. The data was also fitted with the power law prediction of MCT and it was found T_c = 186.6 K. Based on the model function of Havriliak and Negami (HN function) [33] given by $\varepsilon^*-\varepsilon_\infty = \Delta\varepsilon[1+(i\omega\tau)^\alpha]^{-\beta}$, where α and β are shape parameters, they found α=1 and β is a constant for $T > T_c$ and decreases linearly with T for $T < T_c$. This is in contradiction with the light scattering study of Borjesson et al [34] .Subsequently, however, it was noted that the crossover at T_A is an artifact of the data analysis procedure, and the claimed crossover to high-temperature Addhenius behavior is incorrect [35] , [36] .

The correlation between the dielectric relaxation time and viscosity was explored by Payne and Theodorou in 1972 [28] . Vogel-Fulcher law fits for the dielectric relaxation time produced T_0=140 K, while fits for the viscosity produced T_0=150 K.

c) Neutron scattering by Borjesson et al.: the study of τ_α, f_q and T_c

An incoherent quasielastic neutron scattering study of PC was performed by Borjesson and Howell [37] . The work concentrated on the temperature dependence of the quasielastic peak width and the integrated peak intensity in order to study the α-relaxation process. There was no analysis of the dynamic spectrum of the α- or β-relaxation processes.

The temperature dependence of the α-relaxation time $\tau_\alpha = \tau_\alpha(T)$ was determined from the width Γ of the quasielastic peak at $q = 1.6$ A^{-1} and 1.0 A^{-1}. The Power-law fits for $\tau_\alpha = 1/\Gamma \propto (T-T_c)^{-\alpha}$ determined $T_c = 180$ K. The exponent $\alpha = 2.3$ was determined from the viscosity data of Bondeau et al.

MCT predicts a cusp anomaly of the nonergodicity factor f_q at T_c This prediction is tested by studying the integrated quasielastic neutron scattering peak intensity. A cusp was observed by Borjesson et al at 210 K [38].

d) Brillouin scattering by Torell et al: T_c, β_k, Determination of f_q from C_0 and C_∞

Torell and coworkers carried out a series of conventional Brillouin scattering studies of PC by fitting the Brillouin spectra with generalized hydrodynamic theory with the Cole-Davidson model for the relaxation dynamics [34], [17]. The sound velocities C_0 and C_∞ were treated as fitting parameters. An anomalous increase of C_0 around $T = 270$ K was found for $C_0(T)$. A cusp in the nonergodicity parameter $f_0(T)$ was found at $T_c = 270$ K. This value of T_c is a very surprising result because it is far above the estimates obtained from viscosity and neutron scattering studies and is even 50 degrees above melting temperature

T_m (218 K) of PC. The Cole-Davidson relaxation model used in this study yielded a stretching parameter β_k=0.5 for this system in both the liquid and glass states.

e) Sound velocity C_o: Masood's measurement

Masood measured the sound velocity C_0 and attenuation α in the temperature range from 330 K down to 253 K using the pules-echo technique [31]. The ultrasonic frequency used was 15 to 65 MHz. The velocity and attenuation in this range were found to be independent of frequency. $C_0(T)$ followed the linear equation

$$C_0=1524.4-3.14(T/K-273)\ \text{(m/sec)} \tag{1.2}$$

The attenuation increases with decreasing temperature.

f) Crystallization observation by Huck et al.

Despite the fact that PC can easily be supercooled into a glass, it may still crystallize during thermal cycling or if kept in the supercooled temperature region too long. Huck et al observed the crystallization process of PC [39].

3. Salol

Salol was used in the simultaneous PCS and dielectric susceptibility spectroscopy experiment discussed in the section 4.G. This experiment was designed to study PC, but it was found that a vacuum-sealed sample cell required for PC which includes a pair of electrodes could not be made to perform satisfactorily. Therefore salol was used to study the α-relaxation time-scale universality prediction of MCT.

II. THEORY

A. LIGHT SCATTERING FROM DENSITY FLUCTUATIONS

1. Density correlation function and the fluctuation-dissipation theorem

a) Scattered field E(r, t), density fluctuation δρ(q, t) and the fluctuation-dissipation theorem

The fluctuation theory of light scattering was developed by Einstein [40]. According to his theory the intensity of scattered light can be calculated from the mean-square fluctuations in particle density. The first-order scattered field is produced by dielectric fluctuations $\delta\varepsilon(q, t)$

$$E \propto \delta\varepsilon(q, t) = (\partial\varepsilon/\partial\rho)\delta\rho(q, t) + (\partial\varepsilon/\partial T)\delta T(q, t) \qquad (2.1)$$

where $\delta\rho(q, t)$ is the qth Fourier component of the density fluctuation. In most systems it is found that $(\partial\varepsilon/\partial T) \ll (\partial\varepsilon/\partial\rho)$. Starting with eq. (2.1), one can use the laws of macroscopic continuum physics to describe the scattering from the collective motions of large numbers of individual particles in the long-wavelength limit. The scattered intensity $I(q, \omega)$ is

$$I(q, \omega) \propto \int_0^\infty dt \exp(-i\omega t) \langle E^*(q, 0)E(q, t)\rangle$$

$$\propto \int_0^\infty dt \exp(-i\omega t) \langle \delta\rho^*(q, 0)\delta\rho(q, t)\rangle$$

$$\propto \int_0^\infty dt \exp(-i\omega t)\, \Phi(q,\, t)$$

$$\propto S(q,\, \omega) \qquad (2.2)$$

where $\Phi(q,\, t)$ is the density correlation function, and $S(q,\, \omega)$ is the density fluctuation spectrum or dynamic structure factor. The spectrum of eq. (2.2) is completely polarized.

The fluctuation-dissipation theorem provides a connection between the intensity spectrum $I(\omega)$ and the susceptibility spectrum $\chi(\omega)$ [41] .

$$I(\omega)=[n(\omega,\, T)+1]\ \mathrm{Im}\ \chi(\omega), \qquad (2.3)$$

where $n(\omega,\, T)$ is the Bose factor and (from the fluctuation-dissipation theorem)

$\mathrm{Im}\ \chi(\omega) \propto \omega S(q,\omega)$.

B. MODE COUPLING THEORY AND SCHEMATIC MODELS

1. Equation of motion and parameter space

a) Kinetic equation of $\Phi_q(t)$

MCT analyses the nonlinear interactions between different density fluctuation modes self-consistently [4], [42] . The theory shows that the dynamical features of LGT are caused by the interplay of non-linearities and retardation effects, via the memory function integral in Eq. (2.4) below.

The basic quantity of the theory is the normalized density correlation function $\Phi_q(t)=<\delta\rho(q,\ 0)\delta\rho(q,\ t)>/S(q)$, with static structure factor $S(q)=<|\delta\rho_q|^2>$. The starting point of MCT is a set of closed generalized kinetic equations for $\Phi_q(t)$ for different modes

$$\Phi''_q(t)+\Omega_q^2\Phi_q(t)+\Omega_q^2\int_0^t dt'\,M_q(t-t')\Phi'_q(t')=0 \tag{2.4}$$

where (from second moment sum rule) the $\Omega_q = (v^2q^2/S(q))^{1/2}$ is the microscopic excitation frequency, and $v = (k_BT/m)^{1/2}$ is the thermal velocity of the particles (Φ'_q and Φ''_q are first and second time derivatives). Equations (2.4) is similar to the equation of motion for a harmonic oscillator, but with a generalized damping term expressed as an integral which includes the mode coupling and retardation effect. The initial conditions required to solve the eqs. (2.4) are $\Phi_q(t = 0) = 1$ and $\Phi'_q(t = 0) = 0$.

b) Memory function M_q(t-t')

In a simplified version of the theory, called idealized MCT, the memory function (or kernel) $M_q(t-t')$ has two parts

$$M_q(t-t')=\Omega_q^2[\gamma_q\delta(t-t')+m_q(t-t')] \tag{2.5}$$

γ_q represents the regular "fast" relaxation processes in the liquid and $m_q(t-t')$ represents the slow relaxation processes. The function $m_q(t)$ is approximated by

$$m_q(t)=\Sigma_{q_1}V^{(1)}(q,q_1)\Phi_{q_1}(t)+(1/2)\Sigma_{q_1,q_2}V^{(2)}(q,q_1,q_2)\Phi_{q_1}(t)\Phi_{q_2}(t)+.. \quad (2.6).$$

The terms in eq. (2.6) represent the interactions among density fluctuation modes. The $V^{(i)}$s are the coupling coefficients (vertices) which are given solely in terms of the static structure factors S(q). The function $m_q(t)$ represents the cage effect in which a particle is temporarily trapped in the cage formed by its neighbors.

c) Major contribution to $M_q(t-t')$ at $q=q_0$, $V^{(2)}$

The eqs (2.4), (2.5), and (2.6) can be solved numerically for a set of q values if the vertices $V^{(i)}$ are known [43]. The S(q) and $V^{(i)}$ can be evaluated from the interatomic potential [44]. In idealized MCT, the major term in $m_q(t)$ is the two-mode coupling, $m_q(t)=(1/2)\Sigma_{q_1,q_2}V^{(2)}(q,q_1,q_2)\Phi_{q_1}(t)\Phi_{q_2}(t)$, with $q_1 + q_2 = q$. The largest contribution comes from q-values close to the peak of the static structure factor S($q=q_0$), q_0^{-1} corresponds to the separation between nearest neighbors or "first coordination shell".

2. Schematic model of idealized MCT

a) Schematic F_2 model

A schematic version of the idealized MCT, the F_2 model, restricts q to a thin spherical shell in q space at $q=q_0$. All modes in this shell must have identical $\Phi_q(t)$ by symmetry. The eqs. (2.4) therefore reduces to a single schematic equation:

$$\Phi''(t)+\gamma\Omega^2\Phi'(t)+\Omega^2\Phi(t)+\Omega^2\int_0^t V^{(2)}(\sigma)\Phi(t')^2\Phi'(t')\,dt'=0 \qquad (2.7)$$

which can easily be solved numerically on a computer.

b) Early studies of the F_2 model by Bengtzlius et al. and Leutheusser

Leutheusser reported numerical solutions of eq. (2.7) showing the evolution of the two peak structure of the susceptibility spectra as $V^{(2)}$ increases. Under certain approximations, Leutheusser [12] and Bengtzelius et al. [11] carried out expansions around the transition point and reported a set of self-consistent asymptotic solutions of the F_2 model. Although, the results were preliminary and couldn't be compared quantitatively with the experiments, they illustrate clearly the basic concepts and predictions of MCT.

c) Control parameter σ, behavior of $\Phi_q(t, \sigma)$, and critical point $V^{(2)}{}_c = 4$

It was found, as the coupling constant $V^{(2)}(q,q_1,q_2)$ increases, the system transforms from an ergodic liquid state to a nonergodic glass state. This is shown by the $\Phi(\infty)$ jump to f_q^c at V=4. This behavior suggests that MCT could be a model of LGT. MCT assumes that the transition occurred at T_c when coupling constant V increases to a value sufficient to induce the nonergodic behavior. Therefore MCT assumes that V increases linearly when T passes though the critical value at $T=T_c$. MCT only describes the system behavior when V changes. The temperature is introduced into theory only when V is taken as a function of T. This assumption can be justified from numerical analysis of the MCT equations for Hard-Sphere or Lennard-Jones potentials.

In their analyses, the coupling constant $V^{(2)}$ is assumed to be a function of the separation parameter $\sigma \propto (T_c-T)/T_c$, where T_c is the critical temperature and σ measures the distance to this transition singularity. The solution of the F_2 model is obtained for small σ values. With σ approaching zero, the dynamical transition from ergodicity to nonergodicity occurs at T_c. For $T > T_c$. The strength of the coupling constant $V^{(2)}$ increases with decreasing temperature and $\Phi(t)$ decays towards zero more and more slowly. A critical value of $V^{(2)}_c = 4$ is reached at $T=T_c$ and the $\Phi(t \rightarrow \infty)$ asymptotic value increases abruptly from 0 to a finite constant value f^c which is called the Debye-Waller factor. Structural arrest occurs and the system shows an ergodic to nonergodic transition.

d) Cage model

The model of MCT considers the formation of cages in the supercooled region [45]. For $T < T_c$, the particles of the fluid are permanently trapped in the cages, which are formed by their neighbors, without any chance to escape so that density fluctuations no longer decay totally, but decay to a constant value. Above T_c, the cage only localizes the captured particle for a finite time before it finds a path to escape, and the density fluctuations always decay to zero. The α-relaxation corresponds to the long-time decay. The β-relaxation which occurs on a shorter time scale is attributed to atomic motions within the transient cages.

e) Schematic F_{12} model gives non-exponential decay of α-relaxation.

The schematic F_2 model predicts exponential decay of the α-relaxation which does not agree with the observations in many experiments where stretched exponential decay is found. This is due to ignoring the coupling of $\Phi_q(t)$ with other $q_1 \neq q$ modes.

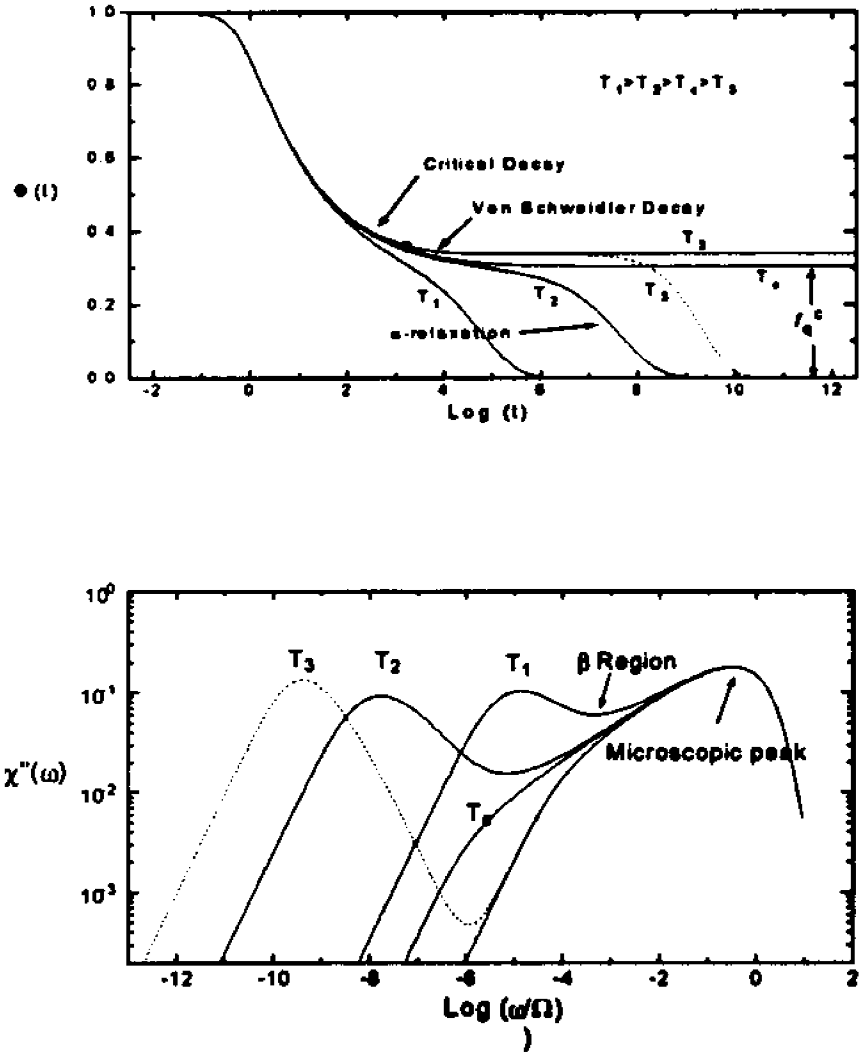

Fig. 2.1. Numerical solution of the F_{12} schematic models. The temperature T_1 and T_2 are in the ergodic liquid state and T_3 is in the non-ergodic glass state. The dash line section of T_3 is the result of the extended MCT which includes ergodicity-restoring hopping processes. The circle between the critical decay and the von Schweidler decay on correlation function $\Phi(t)$ is the inflection point.

A schematic F_{12} model [46]

$$m(t)=V^{(1)}\Phi(t)+V^{(2)}\Phi^2(t) \qquad (2.8)$$

with: $V^{(1)}\neq0$ and $V^{(2)}\neq0$ was found to produce stretched exponential decay. Fig. (2.1) is a numerical solution of the F_{12} model for the correlation function $\Phi(t)$ and the corresponding susceptibility spectrum $\chi''(\omega)$. These results possess several crucial properties independent of the details of the microscopic nonlinear interactions. At $T = T_1$ or T_2 ($\gg T_c$), the system is in the liquid state. The correlation function $\Phi(t)$ first experiences a fast decay, called the critical decay, followed by a slow decay, called the von Schweidler decay, which is the beginning of the slow α-relaxation process. The corresponding susceptibility spectrum $\chi''(\omega)$ is predicted to display three regions: a high-frequency microscopic peak at Ω corresponding to microscopic phonon-like excitations which may be the Boson peak, a low-frequency primary α-relaxation peak which moves towards lower frequencies with decreasing temperature, and between these two an intermediate β-relaxation region surrounding a minimum. At $T = T_c$, $\Phi(t)|_{t\to\infty}$ jumps from zero to f_c. For $T < T_c$, ($T = T_3$), the system enters the nonergodic state. The correlation function $\Phi(t)$ reaches a plateau, via the fast critical decay, and then stays there forever. The value of the plateau increases with decreasing temperature. In the $\chi''(\omega)$ spectrum, the α peak disappears, and the β-relaxation region changes from concave upwards to concave downwards (the so called "knee"). The temperature dependence of $f_q(T)$ is plotted in Fig. (2.2).

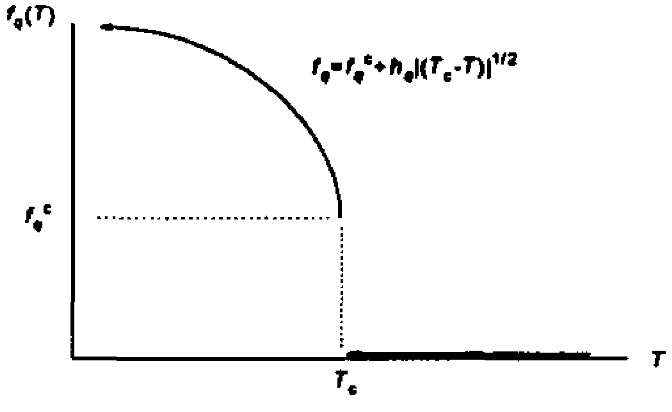

Fig. 2.2. The $f_q(T)$ factor. For $T = T_c$, $\Phi_q(t)|_{t\to\infty}$ arrests at the constant value of f_q^c. With decreasing temperature $f_q(T)$ increases following the relation of $f_q(T) = f_q^c + h_q|T_c - T|^{1/2}$.

3. Schematic Model of Extended MCT

a) Extended MCT, Hopping effect, and δ(T) term in M(z)

The idealized MCT is a convenient but incomplete approximation to the full MCT. The idealized version contains only nonlinear interactions among density fluctuation modes in the memory kernel, representing the cage effect, and predicts a complete structural arrest at T_c. However, experimental results indicate that α-relaxation process still exists even when the system is in the glass state. Following a suggestion by Das and Mazenko [47], Gotze and Sjogren [48] identified the leading correction terms to the memory kernel and developed the extended MCT. These new terms, given as a temperature-dependent hopping parameter $\delta(T)$, represent ergodicity-restoring activated transport processes.

In extended MCT the Laplace transform of the memory function $M(t)$

$$M(z)=\mathrm{L.T.}[M(t)]=i\int_0^\infty \exp^{izt} M(t)\,dt$$

is given by

$$M(z)=\Omega q^2[i\gamma_q+m_q(z)]/\{1-\delta_q(z)\Omega_q{}^2[i\gamma_q+m_q(z)]\}. \tag{2.9}$$

The $m_q(z)$ is the Laplace transform of $m_q(t)$ of eq. (2.6) and $\delta_q(z)$ is the Laplace transform of $\delta_q(t)$ with

$$\delta_q(t)=\Sigma_{q_1,q_2}V'(q,q_1,q_2)\Phi_{q_1}{}'(t)\Phi_{q_2}{}'(t)+\cdots. \tag{2.10}$$

Eqs.(2.4), (2.6), (2.9) and (2.10) constitute the extended MCT. The $\delta_q(t)$ which formally represents coupling to currents is described as an activated transport or hopping effect when a molecule trapped in the cage jumps to another position by overcoming the barrier of its cage via thermal excitation. This hopping effect restores the collective motion of particles and therefore preserves α-relaxation for $T < T_c$. In the extended theory the sudden structural arrest at T_c is replaced by a gradual crossover from liquid dynamics to glassy dynamics; the α peak and susceptibility minimum both exist at all temperatures. There is a transition region between the ergodic liquid state and nonergodic glassy state. Also, the cusp in $f_q(T)$ shown in Fig. (2.2) is rounded when $\delta \neq 0$. The extended theory reduces to the idealized version in the limit $\delta_q = 0$.

b) Schematic model of extended MCT

In the schematic extended F_{12} MCT model [48],

$$\Phi''(t)+\Omega^2\Phi(t)+\Omega^2\int_0^t dt'\, M(t-t')\Phi'(t')=0 \qquad (2.11)$$

with M(z) given by eq. (2.9), and m(t) and δ(t) given by

$$m(t)=V^{(1)}\Phi(t)+V^{(2)}\Phi^2(t), \qquad \delta(t)=V'\Phi'^2(t). \qquad (2.12)$$

The numerical solutions of this schematic models is also shown in Fig. (2.1). For temperature well above T_c, the dynamics predicted by the two versions of the theory are basically the same. At temperatures close to or below T_c, $\Phi(t)|_{t\to\infty}$ reaches a constant value of f_q^c and then increases for the idealized MCT, but decays to zero for extended MCT (the dashed T_3 line). The α peak in $\chi''(\omega)$ still exists for $T < T_c$, i.e. the hopping process restores the α-relaxation.

C. THE SOLUTION OF IDEALIZED MCT AND ITS PREDICTIONS

1. Asymptotic solution of MCT

a) Asymptotic expansion of $\Phi_q(t)$ around the inflection point

This section summarizes the central predictions of idealized MCT. The predictions are derived by solving the full equation of motion (2.4) of $\Phi_q(t)$ around the glass transition singularity for the separation parameter $|\sigma| << 1$ where $\sigma \propto (T_c-T)/T_c$. These asymptotic solutions comprise the essential qualitative features of MCT. The details of the interaction potential control the system-dependent parameters f_q^c, h_q, and λ. For complex materials like PC where the potential is unknown, they are treated as adjustable parameters.

Around the inflection point (see Fig. (2.1)), $\Phi_q(t)$ obeys the following factorization rule.

$$\Phi_q(t)=f_q^c+h_q G(t). \tag{2.13}$$

The q dependence is included in f_q^c and h_q, and all time dependence is included in the q-independent β-correlator $G(t)$.

2. Nonergodicity factor f_c

a) Nonergodicity parameter $f_q(T)$, T_c

The non-ergodicity parameter $f_q(T)$ characterizes the ergodic-to-nonergodic transition of the system dynamics. In idealized MCT $f_q(T)$ is defined as the value of $\Phi_q(t\rightarrow\infty)$. It is the height of the plateau. The $f_q(T)$ factor follows a square root increase of σ from f_q^c for $T < T_c$:

$$\begin{aligned} f_q(T) &= 0 & T &> T_c \\ f_q(T) &= f_q^C + h_q|\sigma|^{1/2} & T &< T_c \qquad (2.14) \end{aligned}$$

The square root cusp in $f_q(T)$ predicted by eq. (2.14) is a primary signature of T_c in MCT. In the extended theory, since $f_q(T)|_{t\rightarrow\infty} = 0$, f_q^c is defined by the inflection point of $\Phi_q(t)$.

The Fourier transform of the constant part of $\Phi_q(t)$ is a $\delta(\omega)$ function with integrated intensity proportional to $f_q(T)$. In neutron scattering experiments, the frozen density fluctuation would produce elastic scattering. Therefore $f_q(T)$ is also called the Debye-Waller factor.

3. β-relaxation

a) *Equation of motion of the β correlator. G(t), g(t) and scaling time t_σ.*

The β-relaxation occurs on the mesoscopic time scale of 10^{-9} to 10^{-5} sec. between the microscopic and α-relaxation processes. In the idealized theory, the equation of motion of the β correlator $G(t)$ is [49], [50]

$$\sigma+\lambda G^2(t)-d/dt \int_0^t G(t-t')G(t')dt' = 0 \qquad (2.15)$$

where the λ is a system-dependent exponent parameter. The β correlator satisfies the scaling law

$$G(t)=|\sigma|^{1/2}\, g_\pm(t/t_\sigma) \qquad (\sigma <> 0) \qquad (2.16)$$

The scaling time is given by $t_\sigma = t_0\, |\sigma|^{1/2a}$. t_0 is a microscopic matching time and ± signs refer to the sign of σ, σ_+ for $T < T_c$, σ_- for $T > T_c$.

b) *The solution of $g_\pm(t)$ and power laws*

The asymptotic solutions of $g\pm(t)$ follow the power laws

$$g_{\pm}(t) = t^{a} \qquad (t_0 << t << t_\sigma) \qquad (2.17)$$

$$g_{-}(t) = -B(t)^{b} \qquad (t_\sigma << t) \qquad T > T_c \qquad (2.18)$$

$$g_{+}(t) = (1-\lambda)^{-1/2} \qquad (t_\sigma << t) \qquad T < T_c \qquad (2.19)$$

The two critical exponents a and b are determined by the exponent parameter λ

$$\lambda=\Gamma^2(1-a)/\Gamma(1-2a)=\Gamma^2(1+b)/\Gamma(1+2b) \qquad (2.20)$$

with ($0 \leq a < 0.4$, $0 < b \leq 1$). Γ is the gamma function. The relaxation function $\Phi_q(t)$ for the β-relaxation region can be constructed from these asymptotic solutions of $g_{\pm}(t)$, or by numerical solution of eq. (2.15).

c) Critical decay, von Schweidler decay, and interpolation approximation at T > T$_c$

For $T > T_c$ $\Phi_q(t)$ follows the critical decay towards the plateau f_q^c

$$\Phi_q(t)=f_q^c + h_q G(t) = f_q^c + h_q(t/t_\sigma)^{-a} \qquad (t < t_\sigma) \qquad (2.21)$$

followed by the von Schweidler decay from the plateau

$$\Phi_q(t)=f_q^c + h_q G(t) = f_q^c - B h_q(t/t_\sigma)^{b} \qquad (t > t_\sigma). \qquad (2.22)$$

which is the beginning of the α-relaxation process.

The two power-law regions of $\Phi_q(t)$ result in two power-law regions in $S_q(\omega)$: $S_q(\omega) \propto \omega^{-(1+b)}$ at low frequencies and $S_q(\omega) \propto \omega^{-(1-a)}$ at high frequencies. The susceptibility spectrum $\chi''(\omega) = \omega S_q(\omega)$ therefore exhibits a minimum between these two regions which asymptotically approaches

$$\chi''(\omega). \propto \omega^{-b} \qquad \omega << \omega_\sigma \tag{2.23}$$

and

$$\chi''.(\omega) \propto \omega^{a} \qquad \omega >> \omega_\sigma \tag{2.24}$$

where $\omega_\sigma = 1/t_\sigma$.

The susceptibility minimum can be approximated by an interpolation equation

$$\chi''(\omega)= \chi''_{\min} [b(\omega/\omega_{\min})^a+a(\omega_{\min}/\omega)^b]/(a+b) \tag{2.25}$$

with

$$\chi''_{\min} \propto |\sigma|^{1/2} \tag{2.26}$$

$$\omega_{\min} \propto |\sigma|^{1/2a}. \tag{2.27}$$

Eqs (2.26) and (2.27) follow directly from the scaling law for $\chi''(\omega)$:

$$\chi''(\omega) = h_q|\sigma|^{1/2}\chi_{\pm}''(\omega/\omega_\sigma) \tag{2.28}$$

and $\omega_\sigma = \omega_0|\sigma|^{-1/2a}$ if one assumes that h_q is independent of T.

d) *Critical decay, von Schweidler decay and α-relaxation at* $T < T_c$

For $T < T_c$, both α-relaxation and von Schweidler decay arrest. The critical decay ends at the plateau $f_q(T)$. $S(\omega) \propto \omega^{-(1-a)}$ on the high frequency side ($\omega > \omega_\sigma$) but there is no spectrum on the low frequency side except for the frequency-independent "white noise". The susceptibility $\chi''_+(\omega)$ is

$$\chi''_+(\omega) \propto \omega^a \tag{2.29}$$

at high frequency and

$$\chi''_+(\omega) \propto \omega \tag{2.30}$$

in the low frequency white-noise region, which results in a knee at the crossover $1/t_\sigma$. This crossover point also scales according to $|\sigma|^{1/2a}$.

e) *Numerically calculated master function*

The two susceptibility master functions $\chi''_+(\omega)$ for the glass state and $\chi''_-(\omega)$ for the liquid state can be calculated numerically by solving eq. (2.15) once λ is know. Eq.

(2.15) predicts that for either $T > T_c$ or $T < T_c$, all susceptibility spectra should scale onto a single master curve [43].

These power-law decays of eqs. (2.23), (2.24), (2.29), and (2.30) imply that there is no characteristic time scale and there is no peak in the $\chi''_+(\omega)$ spectrum.

4. α-relaxation

a) The characteristics of α-relaxation

The long-time part of the correlation function $\Phi(t)$ is the α-relaxation which corresponds to the low frequency peak in the susceptibility spectrum. Experiments have shown that α-relaxation has strong temperature dependence and non-exponential decay. MCT does not predict a general functional form for this process. It only predicts some of the properties of α-relaxation.

b) Scaling law $\Phi_q(\omega/\omega_\alpha)$

In the region of the α-relaxation peak, for $T > T_c$, MCT predicts a scaling relation:

$$\chi''_q(\omega, T) = \Phi_q(\omega/\omega_\alpha(T)) \qquad (2.31)$$

where ω_α is the position of the α-relaxation peak. This scaling is also known as the time-temperature superposition principle.

c) Stretched exponential model

Although the form of $\Phi_q(t)$ is not generic, it was shown by Gotze and Sjogren [51] that the stretched exponential (Kohlrausch) function:

$$\Phi_q(t) \propto \exp[-(t/\tau_\alpha)^{\beta_k}] \qquad (2.32)$$

is a good approximation solution to the MCT equations in the α-relaxation region. If the stretching exponent β_k is temperature independent, then eq. (2.32) automatically satisfies the scaling prediction eq. (2.31). τ_α is the α-relaxation time. There is a general relation $\omega_\alpha\tau_\alpha \leq 1$ for stretched exponential decay.

d) Power law of τ_α and crossover temperature T_c

In MCT the α-relaxation time τ_α follows a power law [52]

$$\tau_\alpha \propto |\sigma|^{-\gamma} \propto |T_c - T|^{-\gamma} \qquad (2.33)$$

with $\gamma = 1/(2a) + 1/(2b)$. T_c can be determined by fitting $\tau_\alpha(T)^{-1/\gamma}$ with a linear function.

D. PREDICTIONS OF EXTENDED MCT

1. Equation of g(t) with $\delta \neq 0$

a) The difference of β correlator equations in the two versions of the theory

The α-relaxation peak and β-relaxation minimum still exist in extended MCT for $T < T_c$. The correlation function $\Phi_q(t)$ in the β-relaxation region can be factorized as in eq. (2.13). The β correlator G(t) is determined by:

$$\sigma-\delta t+\lambda G^2(t)-d/dt\int_0^t G(t-t')G(t')dt'=0 \qquad (2.34)$$

with one additional control parameter δt. δ is the temperature-dependent hopping rate defined in eq. (2.10). $\Phi_q(t)$ eventually decays to zero because at long times the term-δt becomes dominant even for very small values of δ.

2. Two parameter scaling law

a) *Scaling function χ"(ω,σ,δ), δ=0 and δ≠0 Trajectory in δ - σ space.*

In the extended MCT, the one-parameter scaling law for $\chi''(\omega, \sigma)$ of eq. (2.28) is replaced by a two-parameter scaling law $\chi''(\omega, \sigma, \delta t_0)$ where t_0 is a microscopic matching time that makes the hopping parameter δt_0 dimensionless. As T decreases, the system trajectory (C) follows a path in the $(\sigma, \delta t_0)$ parameter space. $\chi''(\omega)$ in the β-relaxation region is a generalized homogeneous function of its arguments:

$$\chi''(y\omega t_0, y^{2a}\sigma, y^{1+2a}\delta t_0)=y^a\chi''(\omega t_0, \sigma, \delta t_0) \qquad (2.35)$$

Choosing $y^{2a}=|\sigma|^{-1}$:

$$\chi''(\omega t_0, \sigma, \delta t_0) = |\sigma|^{1/2}\chi''(\omega/\omega_\sigma, \pm 1, |\sigma|^{-(1+2a)/(2a)}\delta t_0) \tag{2.36}$$

where $\omega_\sigma = |\sigma|^{1/2a}(1/t_0)$. At $\delta = 0$, eq. (2.36) is just eq. (2.28) and the extended version reduces to the idealized version. For $\delta \neq 0$, one parameter scaling is not valid. But, if δt_0 and σ both change with T so that $|\sigma|^{-(1+2a)/(2a)}\delta t_0 = s$ where s is a constant, the simple one parameter scaling still holds as temperature changes. In practice, the simple one parameter scaling only holds for T well above T_c; in general, two-parameter scaling must be used.

The extended MCT predicts that h_q also depends on temperature [21].

E. GENERALIZED HYDRODYNAMIC THEORY

1. Rayleigh-Brillouin spectroscopy

The conventional theory of Brillouin scattering of simple liquids is based on the linearized continuum equations of hydrodynamics [53], [9]. The generalized kinetic equation (2-4) of $\Phi_q(t)$ describes the dynamics of the visco-elastic system. By Laplace transforming eq. (2-4), the normalized spectrum $S(q,\omega)/S(q) = (1/\pi)\,\mathrm{Im}\,[\Phi(z)]|_{z=\omega}$ becomes

$$\frac{S(q,\omega)}{S(q)} \propto I(\omega) = I_0 \frac{\gamma_0 + m''(\omega)}{\{[\omega^2 - \omega_0^2 + \omega m'(\omega)]^2 + [\omega(\gamma_0 + m''(\omega))]^2\}} \tag{2.37}$$

with $\omega_0 = C_0 q$. γ_0 is the regular damping constant, and C_0 is the $\omega \rightarrow 0$ sound velocity. The dynamics of structural relaxation enters eq. (2-37) via the complex memory function m(ω).

The slow structural relaxation process is often described by the single relaxation time (Maxwell-Debye) model. Mountain assumed that the memory function is Lorentzian:

$$m(\omega) = \Delta^2/(1+i\omega\tau) \qquad (2.38),$$

corresponding to simple exponential decay where Δ^2 is the coupling intensity of the interaction between the acoustic phonon and density fluctuation. Frequently, m(ω) is modeled by a Kohlrausch function or the closely related Cole-Davidson (CD) model

$$m(\omega) = \Delta^2/[(1-i\omega\tau_{CD})^{-\beta_{CD}}-1] \qquad (2.39)$$

where β_{CD} characterizes the broadening of the relaxation peak.

The single-relaxation approximation leads to the following well-know results: (i) The Brillouin peak occurs at $\omega_B = \pm\omega_0$ if $\omega_0\tau << 1$, and at $\omega_B = \pm(\omega_0{}^2+\Delta^2)^{1/2} \equiv \omega_{-}$ if $\omega_0\tau >> 1$. (ii) The Brillouin linewidth is a maximum at $\omega_B\tau = 1$. (iii) The denominator of the normalized spectrum in eq. (2-37) can be factored if the poles are well separated, and the spectrum is then the sum of three Lorentzians. Two of them are the Brillouin modes and the third is the Mountain mode or central peak. The integrated intensity I_i of the central peak relative to the full spectrum is

$$I_i = \Delta^2/(\omega_0^2+\Delta^2). \tag{2.40}$$

2. Non-ergodicity parameter f_0

Since the central peak intensity (2-40) is just $f_0(T)$ of MCT [the long-wavelength ($q \rightarrow 0$) limit of $f_q(T)$], by identifying $\omega_0^2 = C_0^2q^2$ and $\omega_0^2 + \Delta^2 = C_\infty^2q^2$, we obtain the result

$$I_i = f(T) = 1 - C_0^2/C_\infty^2. \tag{2.41}$$

Eq. (2-41) applies to Debye relaxation but can be generalized by taking $m(t) = \Sigma_j \Delta_j^2\exp[-t/\tau_j]$. It has been shown by Fuchs et al. [16] that if structural relaxation consisted only of the α-peak, then eq. (2-37) could be used to determine the non-ergodicity parameter $f_0(T)$

$$1 - C_0^2/C_\infty^2 = f_0(T) = f_q^c + h_q|\sigma|^{1/2}. \tag{2.42}$$

F. DIELECTRIC RESPONSE MEASUREMENT

The imaginary part of the dielectric susceptibility, $\varepsilon''(\omega)$, is closely related to the dielectric relaxation process. The relation between the relaxation function, dielectric susceptibility, and macroscopic measured quantities are listed here. [54]

The electric displacement $\mathbf{D}(t)$ is

$$\mathbf{D}(t) = \varepsilon_\infty \mathbf{E}(t) + (\varepsilon_s - \varepsilon_\infty)\int_{-\infty}^{t} \Phi(t-t')\mathbf{E}(t')\, dt' \tag{2.43}$$

where $\Phi(t)$ is the relaxation function and the $\mathbf{E}(t)$ is the electric field. With $u=t-t'$ and $dt' = -du$ we have

$$\mathbf{D}(t) = \varepsilon_\infty \mathbf{E}(t) + (\varepsilon_s - \varepsilon_\infty)\int_0^{\infty} \Phi(u)\mathbf{E}(t-u)\, du. \tag{2.44}$$

By the convolution theorem of Fourier transforms we have

$$\begin{aligned} \mathbf{D}(\omega) &= \varepsilon_\infty \mathbf{E}(\omega) + (\varepsilon_s - \varepsilon_\infty)\Phi(\omega)\mathbf{E}(\omega) \\ &= [\varepsilon_\infty + (\varepsilon_s - \varepsilon_\infty)\Phi(\omega)]\mathbf{E}(\omega) \\ &\equiv \varepsilon^*(\omega)\, \mathbf{E}(\omega). \end{aligned} \tag{2.45}$$

Assuming the relaxation is single exponential decay, we have

$$\begin{aligned} \Phi(\omega) &= \int_0^{\infty} \Phi(t)\exp[i\omega t]dt = \int_0^{\infty} \exp[-(t/\tau)]\exp[i\omega t]dt \\ &= \tau/(1-i\omega\tau) = \tau/(1+(\omega\tau)^2) + i\omega\tau^2/(1+(\omega\tau)^2), \end{aligned} \tag{2.46}$$

and

$$\varepsilon''(\omega) = \mathrm{Im}\,\varepsilon^*(\omega) = (\varepsilon_s - \varepsilon_\infty)[\omega\tau^2/(1+(\omega\tau)^2)]. \tag{2.47}$$

The relation between conductivity G, dielectric loss factor D, and capacitance C is

$$I_t = I_l + I_c = (G + j\omega C)V \tag{2.48}$$

where I_t is the total current, I_l is the loss or conductive current, I_c is the charging current, and V is the voltage.

$$D_l = I_l/I_c = G/(\omega C) \tag{2.49}$$

The imaginary part of dielectric constant ε^* can be deduced from Maxwell theory

$$\nabla \times \mathbf{H} = \mathbf{J}_l + \partial \mathbf{D}_c = \mathbf{J}_t = \varepsilon^* \partial \mathbf{E}. \tag{2.50}$$

In a harmonic field we have

$$i\omega\varepsilon^*\mathbf{E} = \sigma\mathbf{E} + i\omega\varepsilon\mathbf{E} = (\sigma + i\omega\varepsilon)\mathbf{E}. \tag{2.51}$$

It gives

$$\varepsilon' = \mathrm{Re}\,\varepsilon^* = \varepsilon$$

and

$$\varepsilon'' = \mathrm{Im}\ \varepsilon^{*} = -\sigma/\omega \propto G/\omega = CD. \qquad (2.52)$$

For single exponential decay, the eqs. (2-47) and (2-52) result in

$$C\ D = G/\omega \propto \varepsilon'' = \mathrm{Im}\ \varepsilon^{*} = (\varepsilon_s - \varepsilon_\infty)[\omega\tau^2/(1+(\omega\tau)^2)]. \qquad (2.53)$$

G. PHOTON CORRELATION SPECTROSCOPY

In a PCS experiment, temporal fluctuations in the scattered light intensity are recorded.

The autocorrelation function of the scattered light intensity is

$$\begin{aligned} C(\tau) &= \langle I(t)I(t+\tau)\rangle \\ &= s\langle E^{*}(t)E(t)E^{*}(t+\tau)E(t+\tau)\rangle \\ &= s\langle E^{*}(t)E(t)\rangle^2 g^{(2)}(\tau) \\ &= s\langle I(t)\rangle^2\, g^{(2)}(\tau) \qquad (2.54) \end{aligned}$$

where

$$g^{(2)}(\tau) = \langle E^{*}(t)E(t)E^{*}(t+\tau)E(t+\tau)\rangle / \langle E^{*}(t)E(t)\rangle^2 \qquad (2.55)$$

is the normalized intensity correlation function and s is a proportionality constant.

If the field $E(t)$ is a random variable with a Gaussian distribution

$$<E^*(t)E(t)E^*(t+\tau)E(t+\tau)> = |E(t)|^4 + |<E^*(t)E^*(t+\tau)>|^2$$

or

$$g^{(2)}(\tau) = |\, g^{(1)}(0)|^2 + |\, g^{(1)}(\tau)|^2. \qquad (2.56)$$

The first order correlator

$$g^{(1)}(\tau) = |<E^*(t)E^*(t+\tau)>| \qquad (2.57)$$

is the correlation function of the electric field.

In practice $C(\tau)$ is found to be

$$C(\tau) = B(1 + A\, |g^{(1)}(\tau)|^2) \qquad (2.58)$$

where B is the amplitude, and A is a constant < 1 related to the spatial coherence properties of the optical system.

For stretched exponential decay, $g^{(1)}(t)$ is

$$g^{(1)}(t) = \exp[-(t/\tau)^{\beta}] \qquad (2.59).$$

The intensity autocorrelation function is therefore

$$C(t)=B(1+A\exp[-2(t/\tau)^{\beta}]). \qquad (2.60)$$

If the system consists of anisotropic molecules the scattered electric field can include contributions from (i) orientational dynamics of optically anisotropic scatters, (ii) first order scattering from density fluctuations, and (iii) dipole-induced-dipole (DID) second order scattering from pairs of density fluctuations. The scattered electric field $E(t)$ from rotational motion and second order scattering is fully depolarized, i.e. $I_{VH}/I_{VV} = 3/4$. It was recently found that orientational dynamics is the principle scattering mechanism (apart from the Brillouin components) in salol. This results is likely to also apply to other molecular glassformers such as PC [55] .

III. EXPERIMENTS AND DATA PROCESSING

A. SAMPLE PREPARATION

a) Undesired scattering from frozen water in sample

PC of 99+% purity with water content < 0.005% was purchased from Aldrich Chemical. PC is hygroscopic, and absorbed water will freeze below 0 °C producing small ice particles. These ice particles could result in undesired strong light scattering that interferes with the measurement of scattered light from the dynamic processes of LGT.

b) Sample preparation using a molecular sieve.

In preparing the sample for the depolarized light scattering experiment, PC was therefore handled in a dry nitrogen environment to avoid the absorption of moisture. It was first dried with a type 4Å molecular sieve for 24 hours. Subsequently, the dried material was transferred through a 0.1 mm MSI (Micron Separations Inc.) microfilter into the glass sample cell and flame sealed under vacuum.

c) Sample preparation by distillation.

Samples used in the ultrasonic sound velocity measurement and polarized LA mode Brillouin scattering study were further purified by fractional distillation under reduced pressure. Fig. 3.1 shows the distillation set-up. The boiling point of PC is 240 °C. During the distillation process, the pressure was maintained at 0.1 torr. The kettle temperature of undistilled sample was kept at 110 °C to avoid decomposition. The distilled material is at room temperature. Both the top 10% and the bottom 10% of the sample were discarded to eliminate the residual water and impurities, respectively. The distillation process was repeated three times. For the lasr pass, the PC was distilled directly into the sample cell. The sample cell was flame sealed while it was still on the distillation apparatus to avoid contamination. The salol sample was distilled by the same procedure. The boiling point of salol is $T_b = 172$ °C. The undistilled sample is at $T = 100$ °C.

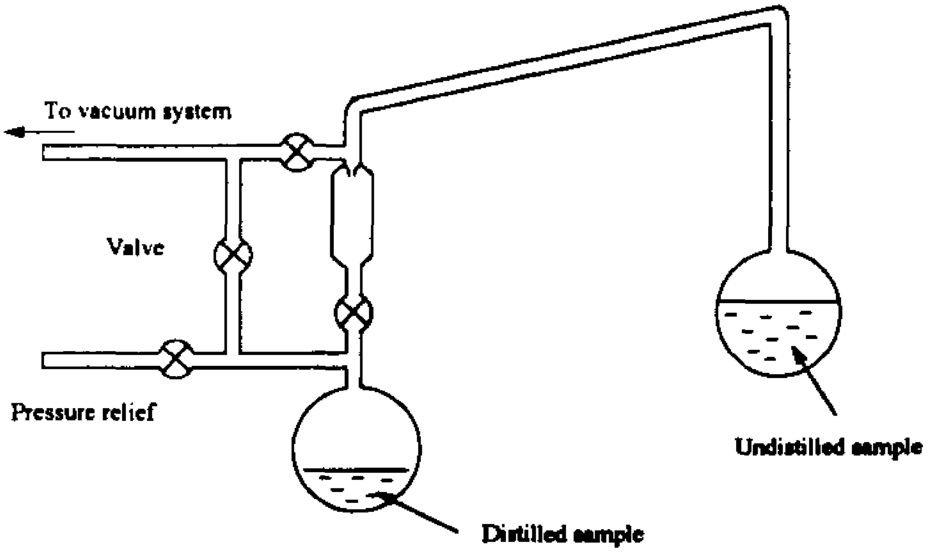

Fig. 3.1. Schematic diagram of distillation set-up used in preparing PC and salol samples. The undistilled sample is at temperature 110°C and the distilled sample is at room temperature.

d) Sample cell and holder for light scattering studies.

The sample cell in the light scattering experiments is a cylindrical glass cell. It is 1.6 cm in diameter by 1.5 cm high made of pyrex glass tubing. Before filling the sample, the cell was immersed in a chromerge solution for three hours and then flushed with distilled water to ensure that it was free from contamination. The sample holder is made of copper with four windows for light access. The assembly of cell and holder is shown in Fig. 3.2.

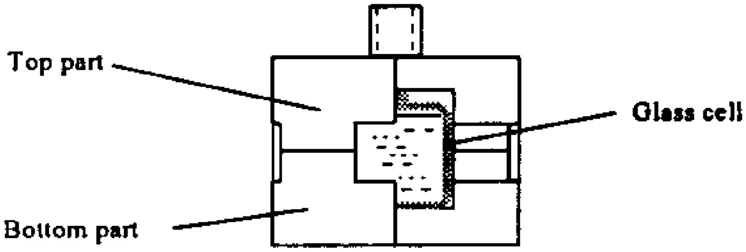

Fig. 3.2. Sample cell and holder for light scattering experiments.

B. EXPERIMENTAL CONSIDERATIONS AND APPARATUS

1. Light Scattering Spectroscopy of LGT

a) Large time/frequency measurement range and elimination of the strong LA mode

The relaxation process in a glassforming material occurs over a wide range of time scales, with different parts the relaxation exhibiting different temperature dependence. To study the dynamics of supercooled liquids, one needs to probe a large time/frequency range. Most conventional spectroscopies cannot reveal these dynamics due to their limited measurement range. New techniques have to be developed.

Viscosity studies indicate that in the crossover region from liquid to glass, the viscosity (and therefore the characteristic time scale) increases by over ten decades. To test the predictions of MCT, the study of LGT should concentrate on the dynamics in the mesoscopic time scale. Unfortunately, the LA and TA phonon excitations are also located in this region. Therefore one needs to differentiate the LGT dynamics from the acoustic phonons.

b) Near back-scattering depolarized Brillouin scattering and its composite spectrum

In the last few years a wide frequency range depolarized near-backscattering Brillouin scattering spectroscopy has been developed in our laboratory. The spectrum is a combination of several Tandem Fabry-Perot Interferometer (TFPI) spectra taken at different free spectral ranges (FSR) and one Raman spectrum. The composite spectra cover over four decades in frequency. The development of this technique has led to the discovery of self-similar spectra of CKN [56] and successful MCT studies of CKN [14] and Salol [15].

To avoid interference from the acoustic phonons, the interferometric and Raman spectra were collected in the VH geometry at a near backscattering angle of $\theta = 172°$. Scattering from the LA mode is vertically polarized (with respect to the scattering plane).

The intensity of the TA mode decreases with increasing scattering angle. Therefore the VH geometry and large scattering angle effectively eliminate the longitudinal and transverse acoustic modes, allowing the weaker scattering due to orientational dynamics and second order DID scattering to be observed. The large scattering angle also increases the effective scattering volume leading to enhancement of the signal-to-noise ratio.

2. Tandem Fabry-Perot Interferometer principle

a) Principle of single pass FP interferometer

The principle of the Fabry-Perot Interferometer (FPI) can be found in many optics textbooks [57]. The principal results are summarized here. For a plane mirror FPI with mirror separation L, The resonance condition is:

$$m\lambda/2=L \tag{3.1}$$

where m is the interference order and λ is the wavelength of the transmitted light. The system transmission function is

$$T=T_o/\{1+(2F/\pi)^2\sin^2[2\pi L/\lambda]\} \tag{3.2}$$

where T_o is the maximum transmission. The finesse F is defined as $\nu/\delta\nu$. ν is the free spectral range and $\delta\nu$ is the full width at half maximum. The finesse is determined by

$$1/F^2=1/F_r^2 + 1/F_S^2+ 1/F_P^2 \tag{3.3}$$

with $F_r = \pi(R/(1-R))^{1/2}$, $F_s = M/2$, and $F_p = 4\lambda(f/d)^2L$. R is the reflectivity of the mirror and M is a measure of the departure of the mirror surfaces from an ideal plane. In a practical set-up, the incident beam first passes a pinhole of size d. Then the beam is collimated by a lens of focal length f before it enters the etalon. The range of angles transmitted by the pinhole results in additional broadening of the spectrum. This pinhole size effect is characterized by F_P. The contrast of the system is

$$C=T_{max}/T_{min}=1+4F^2/\pi^2. \tag{3.4}$$

b) Problems of single and n pass FPI. The principle of Tandem FPI

A typical single-pass system generally has a finesse of about 50 and a contrast of about 1000. Use of such a system to observe the weak LGT signal is difficult due to the presence of the extremely strong LA and TA Brillouin modes and elastic light scattering.

Another problem of the FPI is the overlapping of spectra of neighboring orders. As has been pointed out before, the spectrum of LGT has broad features. The overlapping of neighboring interference orders introduces difficulties for analysis of the spectrum.

The transmission T_n, the finesse F_n, and the contrast C_n of an n-pass FPI are

$$T_n = (T_1)n \tag{3.5a}$$

$$F_n = F_1/(2^{1/n}-1)^{1/2} \tag{3.5b}$$

$$C_n = (C_1)^n \tag{3.5c}$$

respectively. Although the use of n identical FPIs, or equivalently, having the light pass one FPI n times will greatly improve the contrast, it cannot solve the overlapping order problem [58] , [59] . An interferometer consisting of two etalons with unequal spacings in tandem operation provides a solution. The resonance conditions for light to be transmitted through both etalons are

$$m_1\lambda/2=L_1 \qquad \text{and} \qquad m_2\lambda/2=L_2. \tag{3.6}$$

m_1 and m_2 are integers, and L_1 and L_2 are the mirrors spacing of etalon 1 and etalon 2. The synchronization condition is

$$L_1/L_2=\delta L_1/\delta L_2. \tag{3.7}$$

δL_1 and δL_2 are the changes of L_1 and L_2 respectively, produced by the scan.

Sandercock developed a practical design to achieve the synchronization of two etalons [60] . Fig. 3.3 shows the layout of his Tandem Fabry-Perot Interferometer (TFPI).

The axis of the second etalon is rotated by an angle ψ relative to the axis of the first etalon which is also the scanning axis. The spacings of the two etalons is related by

$$L_2=L_1\cos(\psi). \tag{3.8}$$

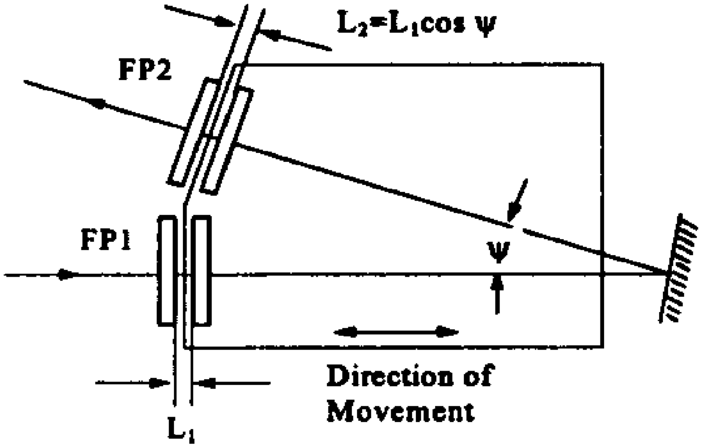

Fig. 3.3. The scanning stage of the Sandercock TFPI which automatically satisfied the synchronization condition of eq. (3.7).

The scan mirrors of the two etalons are mounted on a single translation stage that moves in the direction of the first etalon axis. This design automatically satisfies the resonance and synchronization conditions. (In practice each etalon is multipassed).

The transmission function of this TFPI is

$$T_{tot}=T_1T_2 \tag{3.9}$$

with T_1 and T_2 given by

$$T_1=T_o/\{1+(2F_1/\pi)^2\sin^2[2\pi L_1/\lambda]\} \quad (3.10a)$$

$$T_2=T_o/\{1+(2F_2/\pi)^2\sin^2[2\pi L_1\cos(\psi)/\lambda]\}. \quad (3.10b)$$

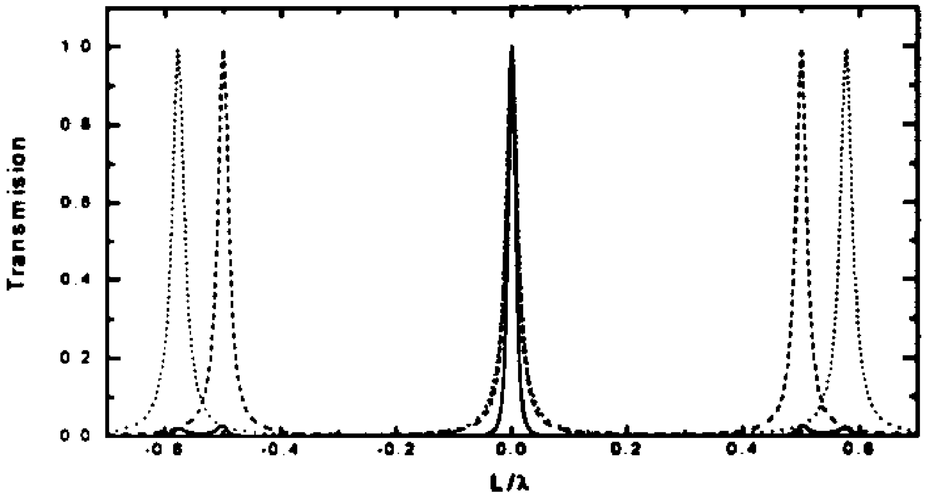

Fig. 3.4. Calculated transmission function eq. (3.9), (3.10a), and (3.10b) of TFPI as function of L_1/λ. The solid line is T_{tot}. The broken line is T_1 and the dotted line is T_2.

Fig. 3.4 is the transmission functions for single FPI_1, FPI_2 and tandem operation T_{tot}. The neighboring interference orders are suppressed. This tandem FPI also produces a higher resolution than a single n-pass FP interferometer.

3. Brillouin scattering apparatus

a) Specification of Sandercock TFPI

Fig. 3.5 shows the Brillouin scattering apparatus configuration for near backscattering. The interferometer is a six-pass Sandercock TFPI that consists of two FPIs with light passing each FPI three times. The corresponding finesses for the mirrors R=94% are F_r=37 and F_s=75, while for 6-pass (3×2) operation, we have F_6 ≈ 100. For this apparatus, L_1 is adjustable from 0 to 2.7 cm and ψ=18°.

b) Optical arrangement of the Brillouin scattering apparatus

A Coherent Innova 90 ion laser operates at 100 mW. The laser has a built in air-spaced etalon to select a single-mode of the 488 nm line. Beam splitter S_1 divides the laser beam into an excitation part and a reference part.

The excitation light field is vertically polarized (relative to the scattering plane). The beam is focused on the sample by lens L_1, mirrors M_1 and M_2. (In a 90° experiment, the laser beam is focused on the sample directly by lens L_1). The scattered light is collected at θ = 172° by the lens L_2 which focuses the light on the spatial filter pinhole SF_1. The aperture size, which defines the scattering volume, is adjusted according to the resolution requirement of each experiment. The lens L_3 collimates the scattered light before entering the TFPI. A polarizer P between L_3 and the TFPI selects the required polarization component. The mirrors M_3, and M_4, lens L_4, and corner-cube, complete the six-pass TFPI optics. Light that comes out of the TFPI passes an Amici prism and lens L_5 before it enters the final pinhole spatial filter SF_2 that is located in front of photomultiplier tube (PMT). The prism, L_5, and SF_2 together act to filter out light from Raman scattering, fluorescence from the sample, and ambient stray light. The instrumental response to input light polarized vertically and horizontally is $I_{VV}/I_{VH} = 1.23$.

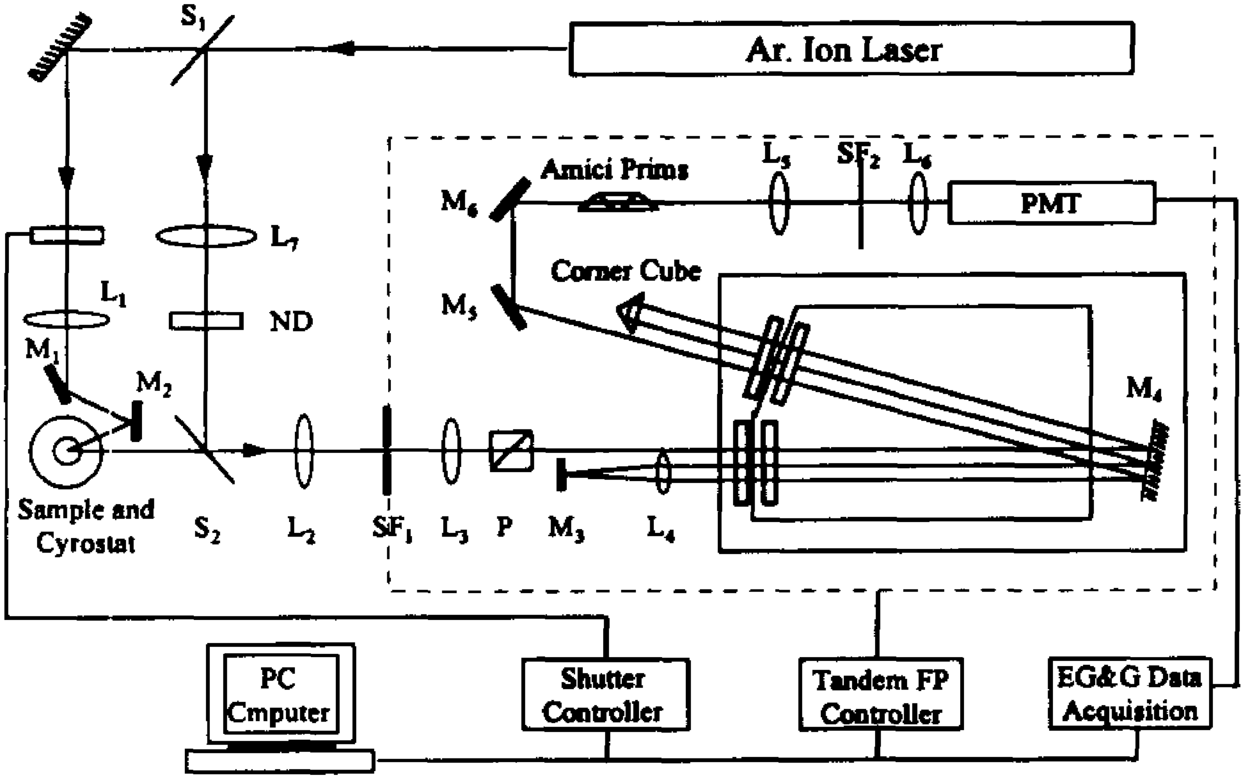

Fig. 3.5. Schematic illustration of the six-pass Sandercock TFPI Brillouin scattering apparatus.

Operation of this system requires a constant reference beam to stabilize the servo alignment control circuit of the TFPI. The reference beam is focused on the spatial filter SF_1 by passing lenses L_7 and L_2, and is superimposed on the scattered light by beam splitter S_2. The intensity of the reference beam is adjusted by the neutral density filter ND. Under normal conditions, the system can operate continually for days without realignment.

c) Shutter control and electronics.

A shutter SH placed in the light path before the sample is used to cut off the excitation beam to prevent the strong elastic scattering from overloading the PMT. The shutter is closed by computer control when the TFPI scans over the elastic scattering frequency region of the central order and neighboring orders. The shutter also serves as an overload protection in case very strong light illuminates the PMT.

The signal of the PMT, after passing a discriminator, is fed to the EG&G multichannel scaler (MCS) data acquisition adapter card in the PC computer. The result is displayed in real-time on the screen and can be saved on the hard-disk for data processing.

d) Protection against ambient interference

This Brillouin scattering apparatus is very sensitive to ambient vibration and temperature fluctuation. Efforts have been made to eliminate the influence of these factors. The whole set-up is mounted on a compressed air floating optical table (Modern Optics). The laser and TFPI are supported by anti-vibration rubber pads. The TFPI is enclosed in a plexiglas box to minimize the influence of air flow between the mirrors of FP etalon and temperature fluctuation. All parts within the dotted line in fig. 3.5 are enclosed in an aluminum chamber to block out ambient light. The only entrance of light is the pinhole of spatial filter SF_1.

4. Raman scattering apparatus

a) Optical arrangement and resolution

Depolarized Raman spectra were collected with a Spex 1401 double grating monochrometer equipped with holographic gratings.

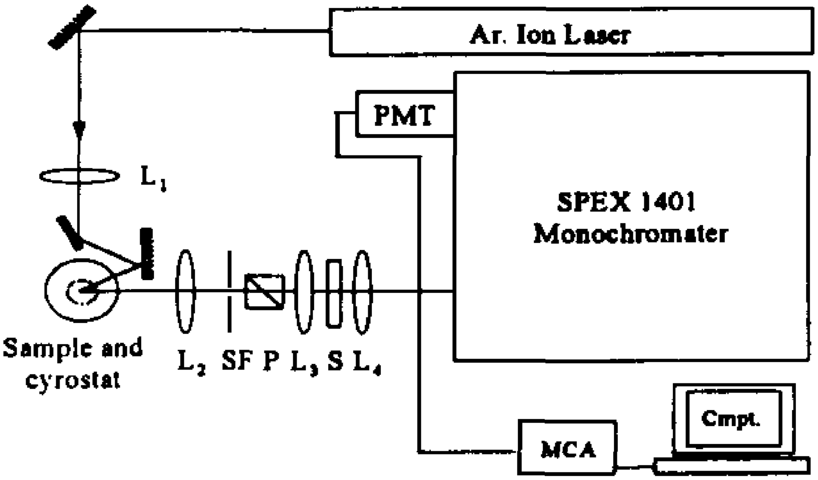

Fig. 3.6. The schematic diagram of Raman scattering apparatus.

Fig. 3.6 shows the Raman scattering apparatus. The excitation light is the 488 nm line of a Coherent 52 Argon laser. The excitation beam is focused on the sample by lens L_1. The excitation electric field is vertically polarized relative to the scattering plane (paper plane). Scattered light is collected at a near-backscattering angle of 172 °, the same as in the case of the Brillouin scattering, by lens L_2 and is focused on the spacial filter SF which selects the scattering volume of the sample. The polarizer P selects the polarization component of scattered light. The lens L_3 collimates the beam. A scrambler S is used to produce unpolarized light in order to average the polarization efficiency of the monochromater. The lens L_4 matches the entrance solid angle and focuses the beam on the entrance slit. The entrance, middle, and exit slits of the spectrometer are usually set to 100, 200, and 100 μm respectively. With these slitwidths, the spectral resolution is 1 cm^{-1}. The PMT signal is sent to the data acquisition adapter card as in the Brillouin scattering experiment.

5. Temperature control apparatus.

a) The importance of temperature control in LGT study.

It is has been pointed out that in the supercooled region the viscosity and relaxation dynamics are very sensitive to variation of temperature. A small change in temperature could lead to a large change in the spectrum. To get reliable results, one needs to have accurate temperature control in the experiments.

b) Cooling apparatus used in the experiment

An Oxford ND1754 cryostat was used to control the temperature in the range of 120 K to 350 K. The system was cooled down by liquid nitrogen. Temperature was regulated with an accuracy of 0.1 K by an Oxford ITC4 temperature controller. The sample holder was tightly screwed onto the cooling finger of the cyrostat. Cry-Con grease was placed on the bottom of the sample cell to keep good heat conduction between sample cell and holder. An additional thermistor was embedded in a hole at the bottom of the sample holder to monitor the approach of the sample temperature to equilibrium.

6. Ultrasonic Phase Sensitive Detection (PSD) Principle and Method

We studied the temperature dependence of the ultrasonic sound velocity C_0. The result is used in the generalized hydrodynamic study of PC. This work was carried out in cooperation with professor J. Toulouse and Dr. L.A. Knauss of Lehigh University.

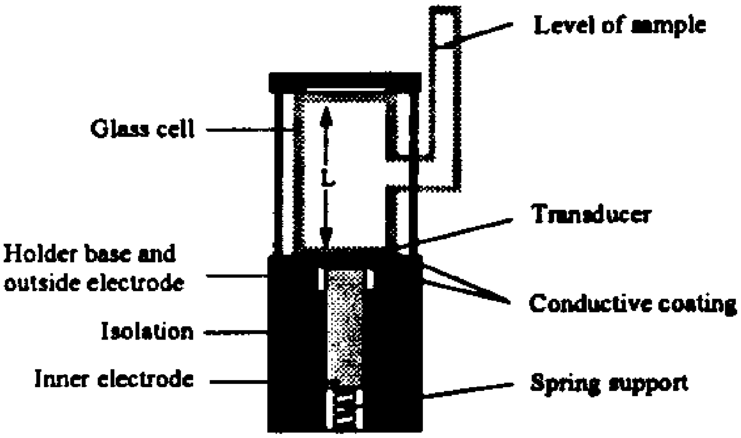

Fig. 3.7 Sample cell assembly for measuring the ultrasonic sound velocity.

a) Sample cell for the ultrasonic measurement

The glass sample cell used in the measurement of sound velocity was purchased from NGS Precision cells Inc.. It is a cylindrical shape with inner length L=20 mm and inner diameter D = 15 mm. The two flat windows are parallel with $\Delta L/L < 0.001$. The cell was cleaned by following the same procedure described in section A. The triply distilled sample was distilled directly into the cell which was flame sealed under vacuum.

The assembly of the ultrasonic cell and 5 MHz transducer is shown in fig. 3.7. The transducer, which serves as both the emitter and receiver of soundwaves, is glued onto the bottom window.

b) Principle of PSD measurement

The ultrasonic sound velocity C_0 is calculated from $C_0 = 2L/T_{rt}$. The purpose of the measurement is to determine the sound round trip time T_{rt}. The phase shift of sound wave is measured to determine the T_{rt}.

Fig. 3.8 shows the principle of the PSD techniques[61] . Signal generator produces a 5 MHz CW wave to the gated RF amplifier and multiplexer M_1. The gated RF amplifier modulates the CW signal and produces a series of pulses to drive the ultrasonic transducer. The transducer emits ultrasonic pulses that travel though the sample and are reflected back by the top window. The ultrasonic pulse may travel through the sample back and forth several times before it is totally attenuated. The transducer also serves as a receiver for the reflected ultrasonic signals. The output of the transducer, as shown at point A in fig. 3.8, is sent to the multiplexer M_2. The time interval t between the leading edge of neighboring pulses is the acoustic echo round-trip time T_{rt}. The local oscillator outputs a CW 65 MHz signal to M_1 and M_2. The output of M_1 is an Intermediate Frequency (I.F.) reference signal of 60 MHz. This I.F. reference signal is divided and fed into M_3 (0°) and M_4 (90°) by 0° and 90° phase shifters respectively. The signal from the transducer is mixed with the 65 MHz local oscillator signal at M_2 to produce pulses with 60 MHz oscillation. This signal is further mixed with the 60 MHz I.F. CW wave from M_1 at multiplexer M_3 and M_4 to produce in phase and quadrature DC outputs. The output of M_3 and M_4 is shown in the oscilloscope photo fig 3.9. The 0° and 90° phase shifters are adjustable to compensate the phase delay in the circuit and to optimize the outputs.

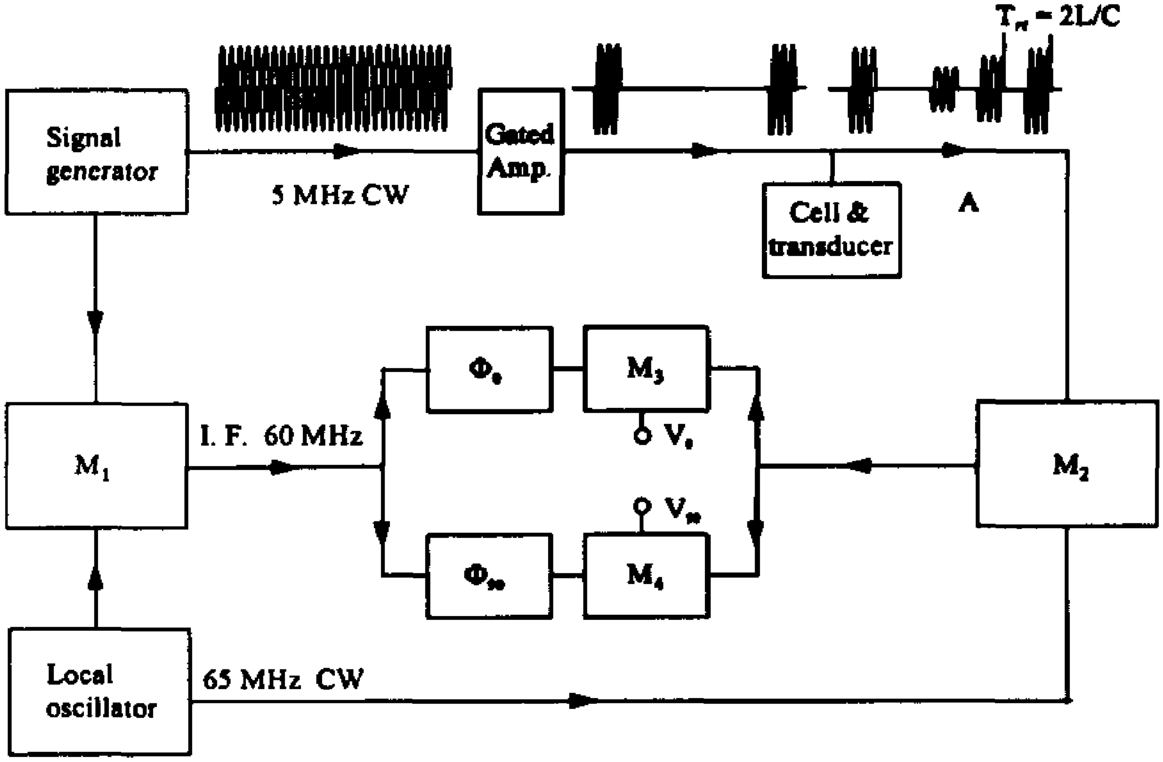

Fig. 3.8. Phase sensitive detection principle diagram.

Fig 3.9. The oscilloscope photo of output V_0 at M_3.

The phase difference of echo signal and reference signal at mixers M_3 and M_4 are measured and used to determine the round trip time T_{rt}. A detailed theoretical analysis of the measurement has been given out by Toulouse and Launay [62] and Petersen et al. [63] .

Finally, the sound velocity C_0 is calculated from

$$C_0(T)=2L/T_{rt}. \qquad (3.11)$$

The precision of the absolute velocity measurement was ~ 1% due to slight convection of the liquid. The relative velocity's change with temperature is obtained with a much better precision ~ 0.05%.

7. Photon correlation spectroscopy (PCS) and dielectric susceptibility measurements

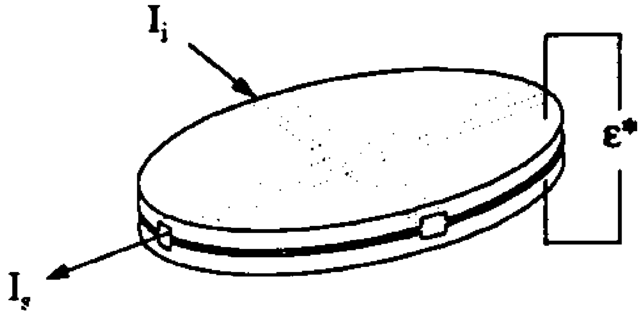

Fig. 3.10. Diagram of electrodes showing the structure and optical path.

The PCS and dielectric measurements are performed simultaneously to study the relaxation process of salol. The information on the relaxation time deduced from the data was used to test the universality of time scale prediction of MCT.

A schematic illustration of the experiment is shown in fig. 3.10. A flat plane capacitor which is immersed in the sample material is used to measure the dielectric susceptibility $\varepsilon''(\omega)$. The light scattering region is at the center of the two electrodes. Therefore the two measurements could be carried out in the same temperature environment.

a) Photon correlation spectroscopy

Fig 3.11 is a schematic diagram of the experimental PCS setup. A Spectra Physics Model 165 argon ion laser equipped with a single-mode etalon operating at 488 nm is used as the excitation source. The excitation field is vertically polarized in the scattering plane. The beam is focused at the center of the sample cell by lens L.

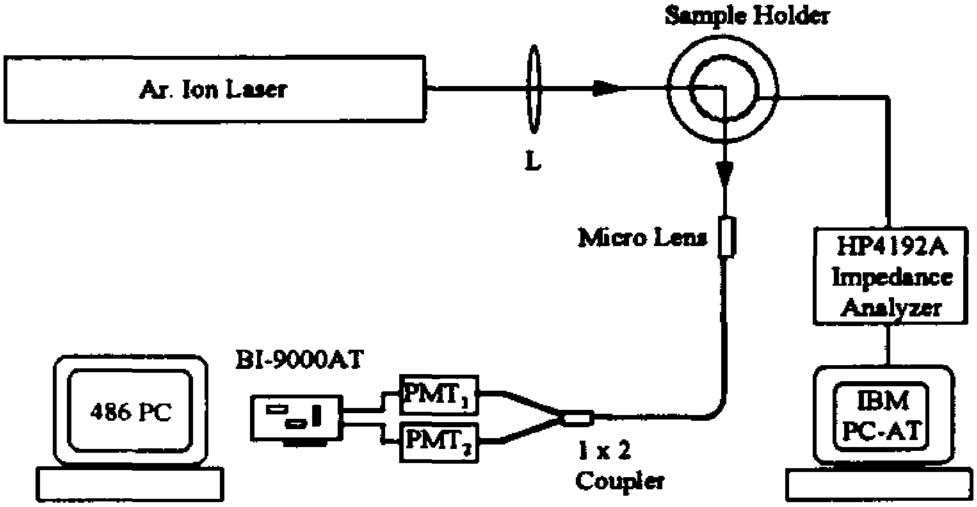

Fig. 3.11. Experimental setup for PCS and dielectric measurement.

Light scattering at 90° is collected by the fiber optic detection system. The fiber optic assembly which consists of micro-collection grin lens, 1 × 2 coupler and two FC connectors is made by OZ Optics (Carp, Ontario, Canada). The focal length of the micro-lens is about 30 cm. The FC connector sockets are mounted directly on the PM tube housings. The use of a fiber optic eliminates the pinholes and lenses used in the traditional photon correlation spectroscopy apparatus. The micro lens and single mode fiber together select the scattering region. This optic fiber detection system was tested on polystyrene.

The intercept to background ratio of the correlation function is 0.98, much closer to the theoretical maximum of 1.0 than can be achieved with conventional optics.

The signal from the PM tubes is sent to a BI-9000AT digital correlator made by Brookhaven Instruments Co. (Holtsville, NY). The BI-9000AT is an adapter card plugged into an IBM compatible computer. The special features of this correlator are that the delay times can be set to a logarithmic scale with a range from 0.1 microsecond to 1,000 seconds. This is important for the study of the stretched relaxation process in the liquid-glass transition. To explore the short time relaxation behavior, the cross correlation mode was used to avoid after-pulsing effects of the PM tubes. The highest temperature measurement is limited by the shortest delay time of the correlator.

b) Dielectric response measurements

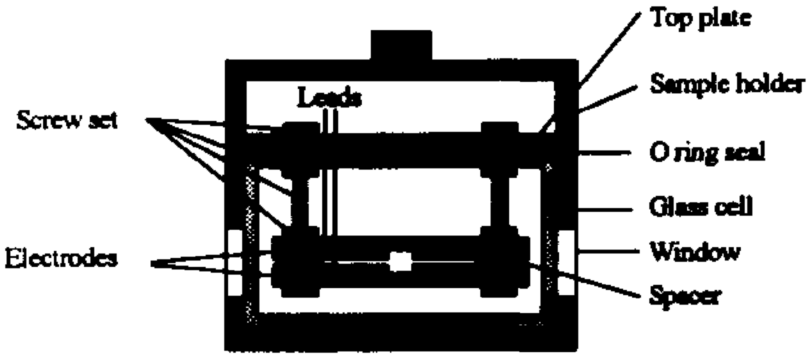

Fig. 3.12. The sample cell assembly for simultaneous PCS and dielectric measurements of Salol. The two electrodes are made of aluminum.

The dielectric data is measured by a HP4192A LF impedance analyzer. In this experiment, the effective frequency scanning region is from 10 Hz to 5 MHz. The impedance analyzer measures the capacitance C and dielectric loss D of the sample as functions of frequency.

Fig. 3.12 shows the structure of the sample cell assembly. The electrodes are made of Aluminum and are separated by three Macor spacers. There are two channels between the electrodes for the optical access path. The capacitance in air is 66 pF. The cell holder is made of copper and is screwed to the cooling finger of cyrostat.

The data acquisition process is controlled by an IBM PC via an IEEE 488 interface. The data are later transferred to the SUN Sparc workstation for processing. The imaginary part of the dielectric susceptibility is calculated from the eq. (2.52) $\varepsilon'' \propto C^*D$. The lowest temperature measured is constrained by the low frequency scan limit of the impedance analyzer.

C. DATA ACQUISITION AND ANALYSIS

1. Setting of temperature

a) Selection of the temperature range of the experiments

The supercooled liquid region of PC is located between T_m=218 K and T_g=160K. In order to study the evolution of the LGT dynamics, especially the stretching of the α-relaxation, the measured temperature range was selected to extend well into the liquid state at high temperature and the glass state at low temperature. Spectra were recorded at temperatures ranging from 350 K down to 135 K in 10 K steps for most cases. Data were collected fifteen minutes after the sample reached the desired temperature. This allows the sample enough time to reach thermal equilibrium.

b) Cooling procedure

Crystallization, if it occurred, would develop in the supercooled region. To avoid crystallization, the PC sample was reheated to a temperature above T_m to ~ 270 K after each spectrum was collected and then cooled to the next desired temperature.

2. Data acquisition and processing procedure

a) Selection of free spectral range and geometry.

Depolarized composite interferometric and Raman spectra were collected in the VH geometry at a scattering angle $\theta = 172°$. The mirror separations of TFPI were set to 0.4, 2.0, 7.5, and 26 mm with corresponding Free Spectral Ranges (FSR) of 375, 75, 20, and 5.77 GHz respectively. Raw data were smoothed in the MCS data acquisition board before being transferred to the VAX 11/780 computer for analysis.

b) Construction of composite spectrum

The procedure used to construct the composite spectra is illustrated in fig. 3.13. Fig. 3.13(a) is a typical depolarized near-backscattering TFPI spectrum obtained at 20

GHz FSR. For the interferometric data, the Stokes and anti-Stokes spectra were averaged to obtain a single spectrum as shown in fig. 3.13(b) (plotted on a log-log scale). The same procedure was followed at each FSR. For the Raman data, only Stokes spectra were recorded. A logarithmic interval averaging was performed for each individual spectrum. Fig. 13(b) shows the results for the Raman and four TFPI spectra. Finally, the five spectra were spliced together by adjusting the amplitude factors to match the overlapping regions. The resulting wide-frequency-range composite spectrum is shown in fig. 13(c). It covers a frequency range from 0.3 GHz to 4 THz.

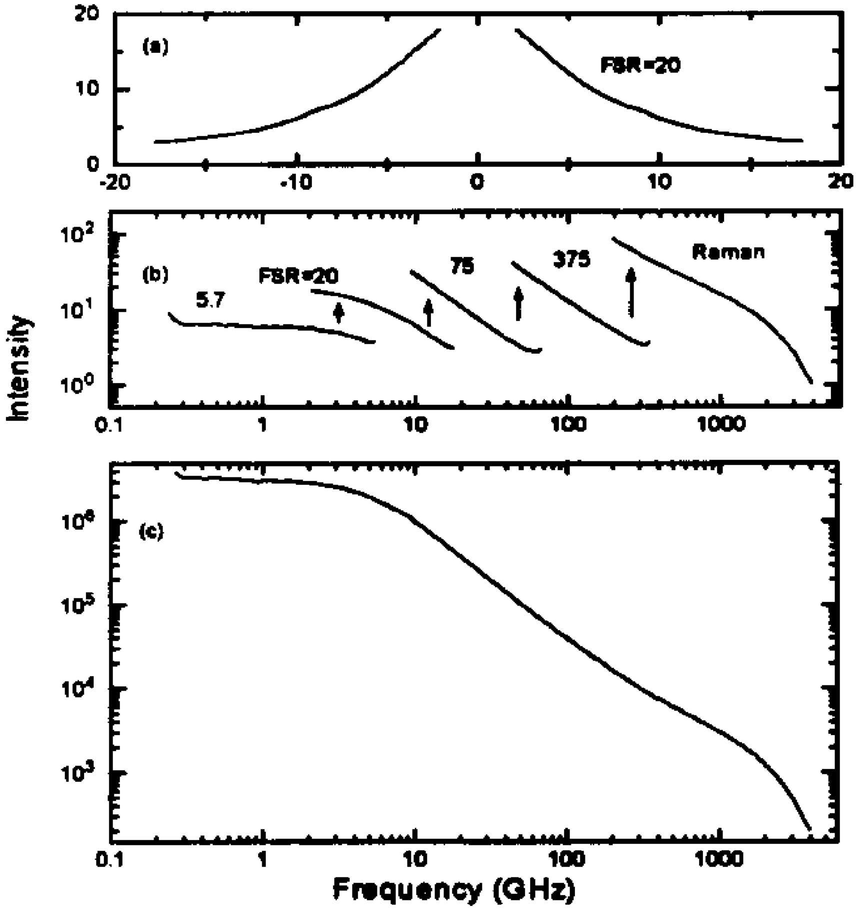

Fig. 3.13. Composite spectrum of PC at 280 K.

The composite spectrum shown in fig. 13 was obtained at $T = 280$ K. The same procedure was performed on data for other temperatures. During the data acquisition, the intensity of the Raman spectra and some of the interferometric spectra were carefully controlled to avoid drifting of the instrumental response. These spectra were used as a standard set to normalize the intensity of the other spectra.

c) Data fitting in the idealized MCT study

The data fitting in the idealized MCT study was performed on the Science Division's VAX11/780 mainframe computer. A non-linear least-square-fitting program "nllsq" of the PORT library was used to fit the spectra with theory. The program was originally written at Bell Laboratories. Later, it was modified in this lab by Dr. Gen Li during the MCT study of CKN and salol. When fitting the α peak, a Filon's procedure is used for Fourier transforming the stretched exponential function eq. (2.32) into a function in the frequency domain. Filon's procedure is able to produce a numerical function over a few decades frequency range that is needed to fit the stretched α-relaxation spectra.

d) Data fitting in the extended MCT study

In the extended MCT study, the data processing was performed on the Science Division's new SUN Sparc workstation. We developed a computer program combining a non-linear least squares fitting program and a numerical calculation program for the theoretical MCT $\chi''(\omega)$ to fit the spectra. The fitting program n2f.f is a FORTRAN program in the Port library. The numerical calculation program betamain.c was originally developed by Dr. Matthias Fuchs of the Technical University of Munich, Germany. The betamain.c program uses a variable step iteration method to solve the β-correlator eq. (2.34) efficiently in a large frequency region. This program is modified here as a subroutine of n2f.f, its numerical solution is supplied to n2f.f as the theoretical function in the fitting process. The n2f.f fits experimental data with this numerical solution in order to search for optimized fitting parameters. At each pass, these parameters are passed to the subroutine to calculate the next round of the numerical solution. This process is repeated until the optimized parameter set is found.

In both the interpolation fitting of the idealized MCT study and β-correlator fitting of the extended MCT study, a number of spectra at different temperatures were fitted globally to obtain a temperature-independent system exponent *a*.

e) $\chi^2 \neq 1$ *due to normalization factor*

The nonlinear least square fitting program seeks a set of parameter that minimize the function $f(x)=\Sigma(y_i-f_i)^2$ where y_i is the ith experimental data value and f_i is the corresponding theory value. The reduced χ^2 is defined as

$$\chi^2 = \Sigma_{i=1}[(y_i-f_i)^2/y_i/(n-n_p)]. \tag{3.12}$$

where n is the number of data points and n_p is the number of parameters. The χ^2 calculation is a criterion to test if the theoretical function agrees with the data. If the noise fluctuation obeys Poisson statistics, the fluctuation is $\Delta y_i=(y_i-f_i)=\sqrt{y_i}$. The reduced χ^2 is 1 if the theoretical function accurately describes the experimental data. Otherwise $\chi^2 > 1$. However, this holds only when the y_i are the experimental raw data. In the case where the raw data have been normalized, the reduced χ^2 will be scaled by the normalization factor. In the depolarized light scattering study, the individual Brillouin/Raman spectra have been normalized during the process of constructing the composite spectra. The normalization factor varies for different sections of the composite spectrum. In order to carry out the χ^2 testing, the ratio of each section of the composite spectrum to the corresponding raw data needs to be calculated. Then the value of the reduced χ^2 of this section of the spectrum could be compared with this ratio. In the ideal case, they should have the same value.

Fig. 3.14 is an example of the scaled factor to χ". The raw data is a section of a depolarized Brillouin spectrum. A linear fitting produced a $\chi^2 = 1.1403$. The raw data was scaled by a factor of 20 to produce scaled data. The scaled data was fitted with same function, and produced a $\chi^2 = 22.806$, which is 20 times of the result of raw data case.

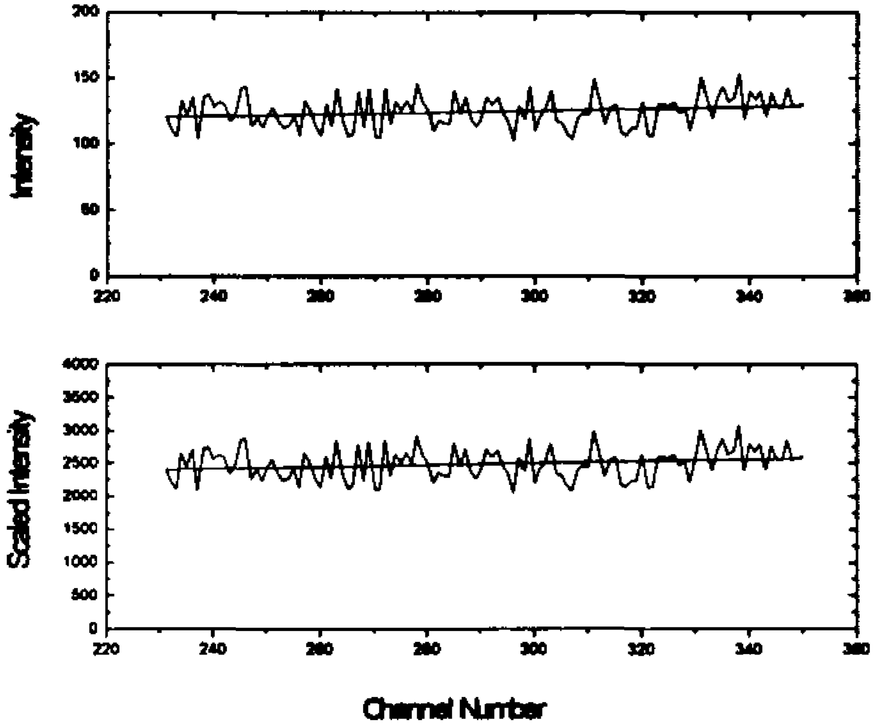

Fig. 3.14. The top plot is the raw data. The bottom one is the scaled data (by a factor of 20).

f) Fitting program list

The data fitting programs used in this work are stored in the Science Division's mainframe computer "scisun" directory: /home1/physics/hzc-grp/:

1. Fitting the α-peak with a stretched exponential model by using Filon's procedure.

   Directory: /home1/physics/hzc-grp/MCT/afa-beta-fit

Programs: **afafit.f, a-b.dat, and nllsqf.f**

2. **Fitting the β relaxation region with the idealized MCT interpolation model**

Directory: **/home1/physics/hzc-grp/MCT/afa-beta-fit**

Programs: **betafit.f and nllsqf.f**

3. **Fitting the β relaxation region with the extended MCT β correlator equation**

Directory: **/home1/physics/hzc-grp/Weimin/E_MCT_fit**

Programs: **emctn2f.f, efnc.c, beta.h, betaint.c, betafour.c, and readme**

IV. RESULTS AND ANALYSIS

A. GENERAL CHARACTERISTICS OF DEPOLARIZED LIGHT SCATTERING SPECTRA

1. θ =172° near-backscattering spectra

a) Intensity spectra I(ω), *Scaling behavior, and LA and TA modes*

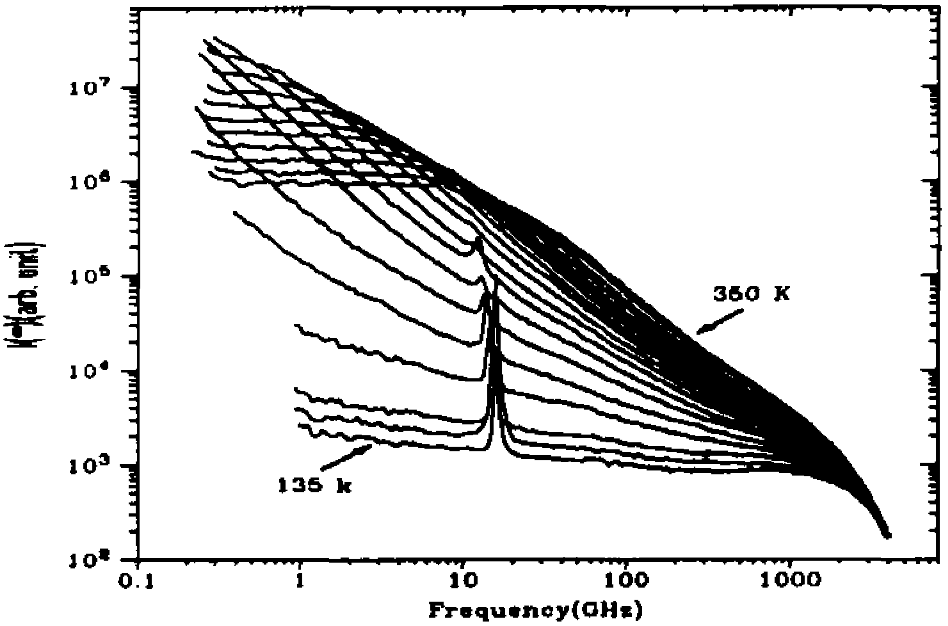

Fig. 4.1. Composite I_{VH} spectra of PC at θ =172°. The temperatures are (from top to bottom) 350, 330, 310, 295, 280, 270, 260, 250, 240, 230, 220, 210, 200, 190, 180, 170, 160, 150, and 135 K. The peaks around 12 GHz are due to leakage of the LA Brillouin mode through the imperfect polarizer.

A complete set of depolarized near-backscattering composite spectra at $\theta = 172$ ° is shown in fig. 4.1. These spectra span a frequency range of over four decade, from 0.3 GHz to 4 THz, and display a continuous evolution of the dynamics with decreasing temperature. At high temperatures the broad central peak extends up to several THz. It narrows continuously with decreasing temperature, while the high-frequency microscopic region above 1 THz is essentially temperature independent. Around 190 K, the spectra exhibit two distinct power law regions implying a two-step relaxation process as predicted by MCT. These are the general features of the spectra of fragile glassforming liquids. They have been found for CKN [14], salol [15], and OTP (Ortho-terphenyl) [64] . Similar characteristics have also been observed in neutron scattering spectra of several glassforming materials [65] , [66] , [67] , [68] . The narrow peaks near 12 GHz are the intense LA Brillouin modes, which leak slightly through the imperfect polarizer.

b) $\chi''(\omega)$ *spectra. Temperature dependence of* α *peak,* β *minimum, and Boson peak.*

The intensity spectra of fig. 4.1 were converted to susceptibility spectra $\chi''(\omega)$ through the relation

$$\chi''(\omega) = I(\omega)/[n(\omega,T)+1], \qquad (2.3)$$

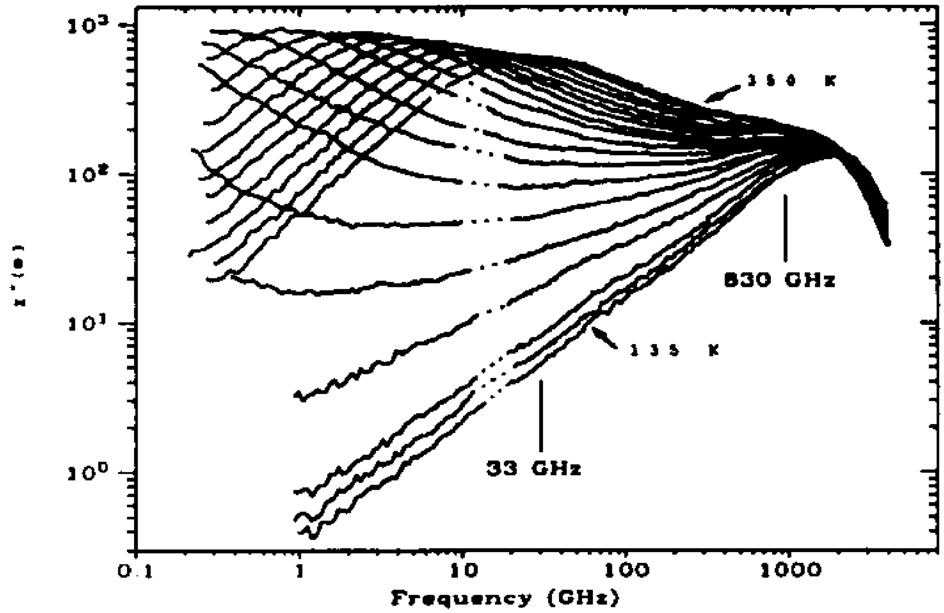

Fig. 4.2. Susceptibility spectra $\chi''(\omega)$ obtained from the data of fig. 4.1. The temperatures are the same as in fig. 4.1. At high temperatures, the α-peak merges with the β spectrum and both merge with the microscopic band. When the sample is cooled, the α peak moves away from the microscopic band and the β spectrum develops. The two vertical lines indicate the spectral range selected for the scaling analysis for $T < T_c$ as described in the text. The LA modes have been moved here for clarity.

where $n(\omega, T)$ is the Bose factor. These $\chi''(\omega)$ spectra, shown in fig. 4.2, exhibit the evolution of structural relaxation with decreasing temperature identified in other experimental studies and also predicted by MCT. The broad peak at low frequencies is the α-relaxation peak which is associated with the primary structural relaxation process. The α peak moves towards lower frequencies with decreasing temperature and disappears from the spectral window of our experiment at ~220 K. The weaker high frequency peak at ~ 1.6 THz is the microscopic band (sometimes called the boson peak). It shows a weak temperature dependence. At high temperatures, only the α peak and the microscopic band are visible. With decreasing temperature, as the α peak moves towards lower frequencies, the β-relaxation spectrum gradually develops in the intermediate-frequency region between the α peak and the microscopic band. At temperatures below ~200 K, the α peak and the minimum of the β-relaxation have moved out of the available spectral window.

2. $\theta = 90°$ spectra and the depolarization ratio

a) q independence of VH spectra

Another set of depolarized spectra was collected with scattering angle $\theta = 90°$. These spectra were very similar to the 172° spectra, except that they were weaker, and the transverse Brillouin components appeared for temperatures below ~190 K. The LA Brillouin components that appear because of imperfect polarization selection are also shifted to lower frequencies. The $\theta = 90°$ susceptibility spectra are shown in fig. 4.3. The α peak shows similar temperature dependence as found in the $\theta = 172°$ spectra. The close agreement between the two sets of spectra demonstrates that the relaxation process responsible for the observed depolarized light scattering is *q* independent in the small-wave-vector limit.

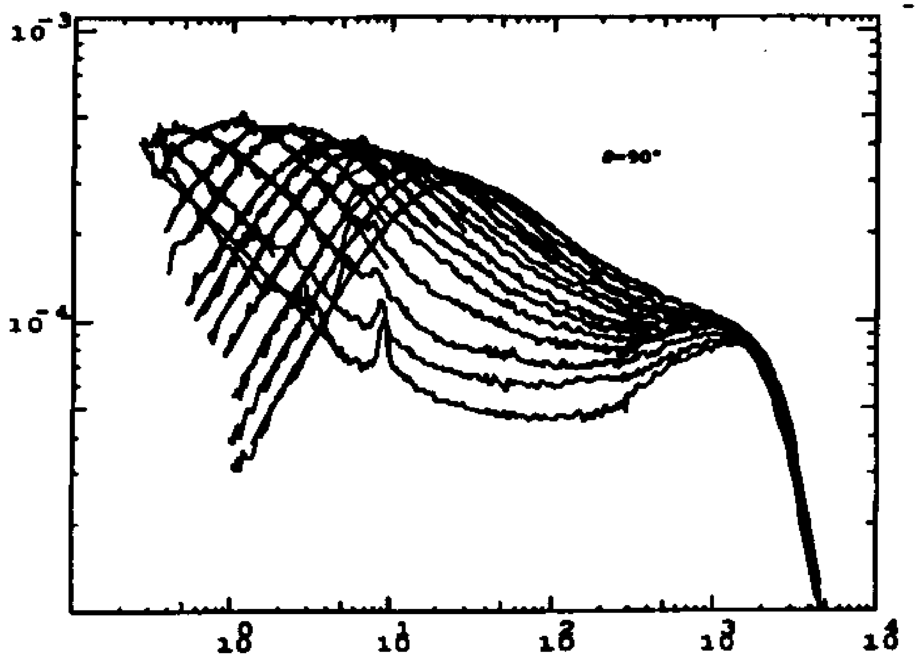

Fig. 4.3. The $\theta = 90°$ $\chi''(\omega)$ spectra. The temperatures are (from top to bottom) 350, 330, 310, 295, 280, 270, 260, 250, 240, 230, 220, 210, and 200K.

b) Depolarization ratio

The depolarization ratio, defined as the ratio of depolarized light scattering intensity to polarized light scattering intensity I_{VH}/I_{VV}, can be predicted if the scattering either is dipole-induced-dipole (DID) second-order scattering [14] or scattering due to orientational fluctuation of optically anisotropic molecules. For either case the predicted depolarization ratio is 3/4. We studied the depolarization ratio of PC. The polarized spectra were measured by Raman scattering and Brillouin scattering in the liquid state (T=295 and 230°K), supercooled region (T=200°K), and glass state (T=140°K). The results are similar to the depolarized spectra except for the Brillouin components. The depolarization ratio found was $I_{VH}/I_{VV} \approx 0.62$. The depolarization ratio has neither a significant frequency dependence nor appreciable temperature dependence.

B. TESTING OF THE IDEALIZED MCT

It is useful to begin the data analysis on the basis of the idealized MCT predictions, even though they are only an approximation to the complete theory. First, the equations are simple and easy to manipulate. Second, they provide estimates for T_c and λ, which are needed as a starting point for the extended MCT analysis. Due to the hopping process, which is ignored in the idealized MCT, discrepancy between experiment and theory should be expected at temperatures close and below T_c.

The tests of idealized MCT are focused on the scaling of spectra and the power-law temperature dependence of scaling parameters for both the α- and β-relaxation processes, the stretching of α-relaxation, and the transition crossover temperature T_c. The data analysis was performed on the $\chi''(\omega)$ spectra shown in fig. (4.2) which gives more reliable information than intensity spectra.

1. β-relaxation

a) Global interpolation fits of β relaxation spectra for $T > T_c$

According to MCT, the LGT singularity can be understood by studying the dynamics of the β-relaxation process. Therefore the tests begin with the interpolation approximation function of eq. (2.25). The results of these fits provide the PC exponent system parameter λ that will be used in other analyses.

The susceptibility spectra of fig. 4.2 exhibit a susceptibility minimum for temperatures between 190 K and 270 K, as expected for the β-relaxation process when $T > T_c$. The spectra in this temperatures range were fitted to the interpolation equation

$$\chi''(\omega)=\chi''_{\min}[(\omega/\omega_{\min})^{a}+(\omega_{\min}/\omega)^{b}]/(a+b) \qquad (2.25)$$

by using a non-linear least-square fitting program. The nine spectra for different temperatures were fitted simultaneously to eq. (2.25). This is called global fitting. For each spectrum $\omega_{\min}(T)$ and $\chi''_{\min}(T)$ were varied independently, but a single optimum value for the critical exponent a was found, with the exponent b constrained via eq. (2.20)

$$\lambda=\Gamma^{2}(1-a)/\Gamma(1-2a)=\Gamma^{2}(1+b)/\Gamma(1+2b). \qquad (2.20).$$

b) Fitting region

As an asymptotic solution of the mode coupling eqs. (2.4), (2.5), and (2.6), eq. (2.25) would be valid only within a limited frequency range around the minima. One could expect that $\omega_{\min}$ and $\chi''_{\min}$ would not depend on the fitting range selected, but this might not be true for the exponent a. Different fitting ranges were explored to study this effect.

Eight spectra from 200 K to 270 K were fitted globally. The result is shown in fig. 4.4. The low frequency limits of the fits are marked by lines a, b, ... f and the high frequency limits are marked by lines x, y, and z. The parameters $\omega_{min}(T)$ and $\chi''_{min}(T)$ were found to be independent of the fitting range. The resulting critical exponents a, which do depend on the range, are shown in Table I.

The results show that a does not depend significantly on the high frequency limit. The critical decay $(\omega/\omega_{min})^a$ reasonably describes the high frequency part of the β minimum region. However a increases if the low frequency limit is extended to lower frequency (from a to f).

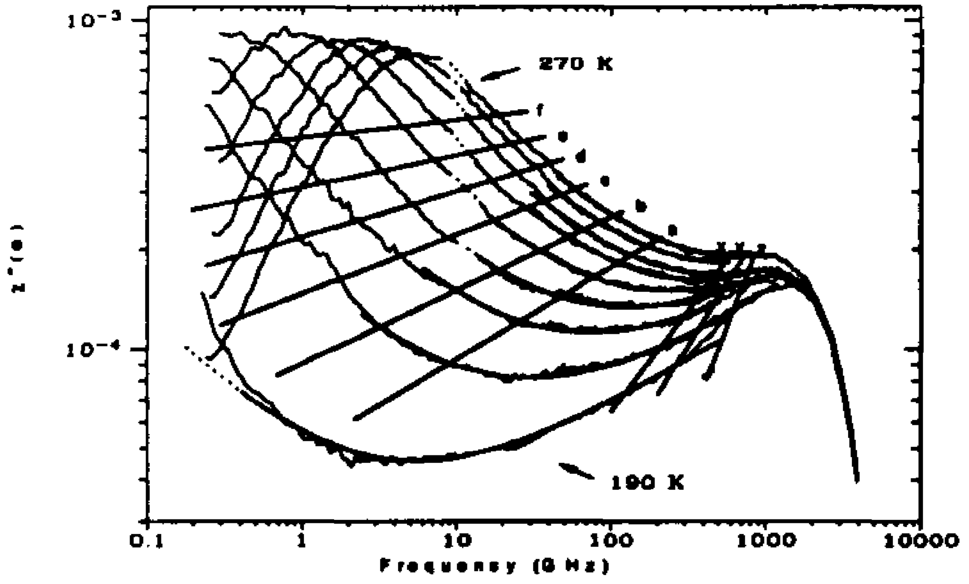

Fig. 4.4. The experimental susceptibility spectra for 190 ≤ T ≤ 270 K fitted by the idealized MCT interpolation equation (2.25) in the β-relaxation region with a=0.29 and b=0.50. (λ =0.78). For the 190 K curve, the MCT fit has been extended beyond the fitting region (dotted line) to illustrate the disagreement resulting from the neglect of hopping effects.

Table I. The critical exponent a for different fitting ranges.

	a		
	x	y	z
a	0.252	0.250	0.264
b	0.267	0.263	0.269
c	0.280	0.275	0.277
d	0.293	0.287	0.287
e	0.301	0.296	0.295
f	0.308	0.304	0.303

The exponent b increases as a increases due to the constraint of eq. (2.20). The result indicates that the exponent b of the von Schweidler decay $(\omega_{min}/\omega)^b$ increases when more of the high frequency tail of the α- peak is included in the β-spectrum region. For this reason, the fitting range must be limited to a small region around ω_{min}.

c) Expansion of scaling regions as T approaches T_c and the discrepancy between theory and experiment on the low frequency side of the β spectra.

To show the effect of the hopping process at low temperature, the 190 K spectrum was also included in the global fitting and shown in fig. 4.4. This fitting is performed in the range between the end points of fitted functions. The values of $\omega_{min}(T)$ and $\chi''_{min}(T)$ found from the fits are listed in Table II. The best fit of a was 0.29, from which b=0.50 and λ = 0.78.

In fig. 4.4 the frequency range over which the theory and experiment agree expands with decreasing T. The expansion verifies an important prediction of MCT concerning the approach towards the glass transition singularity. For 190 K the theory describes the data over a three-decade frequency interval. However, for frequencies below ~0.5 GHz at low temperatures, one notices that the data tend to lie above the idealized theory curves. This discrepancy is what one expects to happen near T_c as a result of neglecting the hopping processes.

d) Master function scaling fits for $T > T_c$

The region of the β-relaxation minimum could also be studied by fitting it to the master function. The master function of idealized MCT for the β-relaxation minimum region is obtained by solving the β correlator eq. (2.13) [43]. The solution for a set of control parameters λ and σ can be expresses as a combination of a few polynomials that is valid in a particular frequency range. The coefficients of each polynomial are tabulated [43].

The control parameter λ can take values between 0.4 and 1.0. σ, in this master function calculation, has the value of -1 and +1 indicating the liquid state and the glass state respectively.

The susceptibility master functions $\chi''_{\pm}$ (ω/ω_σ) were constructed by using this approach.

The $\sigma = -1$ curve is a generalized parabola that increases more steeply with decreasing λ. The minimum position does not occur exactly at $\omega/\omega_\sigma = 1$ but is slightly shifted depending on the value of λ.

The χ''_- (ω/ω_σ) spectra for three different choices of λ (with $\lambda = 0.71$, $\lambda = 0.78$, and $\lambda = 0.85$) were calculated and are plotted in fig. 4.5(a). $\lambda = 0.78$ is the value determined in the above interpolation fitting. The curves of $\lambda = 0.71$ and 0.85 were plotted for comparison. These two curves have been shifted horizontally and vertically to overlap the minima with the $\lambda = 0.78$ curve.

e) Master function scaling and error bar of λ

The nine spectra for $190 \leq T \leq 270$ K were scaled onto the $\chi''_-(\omega/\omega_\sigma)$ master function for $\lambda = 0.78$ as shown in fig. 4.5(a). The overlap of the spectra with the master function indicates that they obey the MCT scaling law. The values of $\omega_{\sigma-}$ and $\chi''_{\sigma-}$ found from the scaling fits are listed in Table II. The accuracy of the exponent parameter $\lambda = 0.78$ could be estimated by comparing the spectra to two other master functions for $\lambda=0.70$ and $\lambda=0.84$ which are also shown in fig. 4.5(a). The large disagreement between these two master functions and the spectra indicates that the precision for λ is λ=0.78±0.05 with the corresponding exponents $a = 0.29 \pm 0.03$ and $b = 0.50 \pm 0.09$. As in the case of the interpolation fits, fig. 4.5(a) shows that there are discrepancies on the low frequency side of the 190 K spectra.

f) Master function scaling fits for $T<T_c$

The master function χ''_+ for $T < T_c$ with of $\lambda = 0.78$ is plotted in fig. 4.5(b). A crossover (the "knee") separates the two parts of the spectrum, $\chi''_+(\omega) \propto \omega$ and $\chi''_+(\omega) \propto \omega^a$. The scaling analysis for $T < T_c$ is much less clear than for $T > T_c$ since there is no susceptibility minimum visible within the frequency range of the spectra. Futhermore, unlike CKN [14], for PC there is no obvious knee that could be used to scale these low temperature $\chi''_+(\omega)$ spectra. Furthermore, hopping effects imply much larger corrections to the idealized MCT results of eq. (2.30) for $T < T_c$ than for $T > T_c$ [52], [21]. To apply the idealized results for $T < T_c$, we proceeded as follows. We selected a center frequency of 166 MHz, which is one-tenth of the microscopic peak frequency, and performed the scaling analysis on the data in the range from 1/5 to 5 times this frequency (33 GHz to 830 GHz) indicated by the two vertical lines in fig. 4.2. For PC, as for salol [15], the crossover from $\chi''_+(\omega) \propto \omega$ to $\chi''_+(\omega) \propto \omega^a$ predicted by the idealized MCT is completely obscured (presumably by hopping effects) at low frequencies and by the microscopic structure at high frequencies. It was therefore not possible to carry out a scaling analysis with the

$\chi''_+(\omega)$ data alone as in the case of CKN [14]. Since the PC susceptibility spectra in this region are nearly linear on the log-log plot of fig. 4.2, we computed the average slope $d\log(\chi'')/d\log(\omega)$ in this range, and shifted the center of the data (at 166 GHz) to the point on the $\chi''_+(\omega)$ master curve having the same slope. This procedure produced the ω_σ and χ''_σ scaling values for $T < T_c$ listed in Table II.

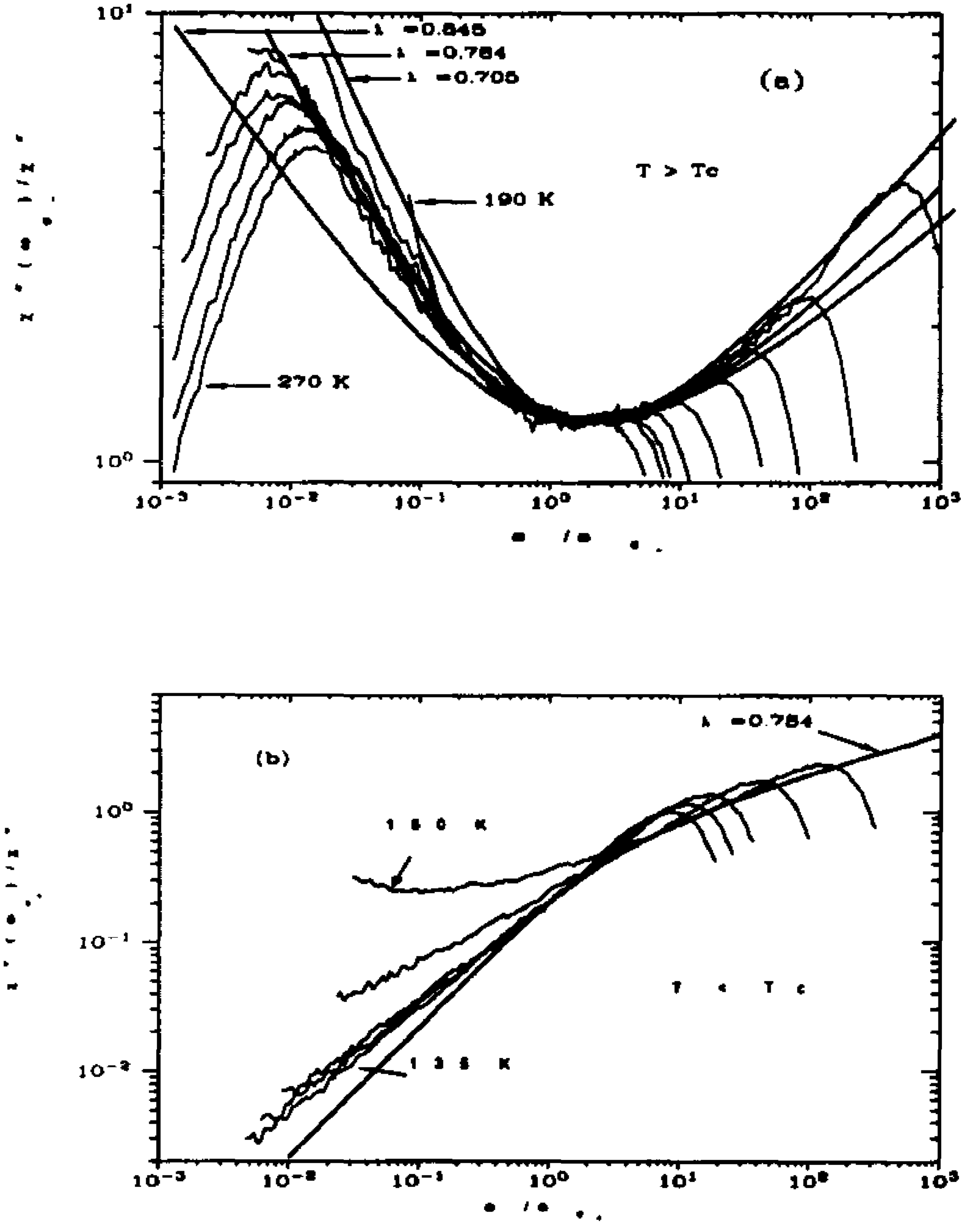

Fig. 4.5. Susceptibility spectra shifted to match the master functions $\chi''_{\pm}(\omega/\omega_\sigma)$ for λ=0.78. (a) ($T > T_c$): temperatures are, 190 K to 270 K in steps of 10 K. To demonstrate the accuracy of the exponent parameter λ, two other master functions with λ=0.70 and 0.84 are also plotted. (b) $T < T_c$: Scaling of the portion of the $\chi''(\omega)$ spectra between the vertical arrows in fig. 2 onto a λ =0.78 master function. Temperatures are 180, 170, 160, 150, and 135 K.

The scaling results are shown in fig. 4.5(b). Severe discrepancies are evident at low frequencies, as expected for the idealized MCT. The low-frequency discrepancies, seen in fig. 4.5(b) for $T = 135$, 150, 160, and 170 K as well as in fig. 4.5(a) for $T = 190$ K and 200 K, indicate the effects of activated transport (hopping) processes not included in the idealized MCT.

g) Power-law behavior of the scaling parameters of β-relaxation and T_c

One of the most important results of MCT is the power-law prediction of eqs. (2.26) and (2.27) for the T dependence of the scaling parameters: $\omega_\sigma^{2a}(T) \propto |\sigma|$; $\chi''_{\min} \propto |\sigma|^{1/2}$. Fig. 4.6 shows the frequency of the susceptibility minimum $\omega_{\min}$ for $T > T_c$ obtained from the interpolation fits as well as the scaling frequency $\omega_{\sigma\pm}$ for $T > T_c$ and $T < T_c$ obtained from the scaling fits to the master function, each plotted as ω^{2a} vs T to test the scaling-law prediction. Each set of data was fitted with a linear function $\omega^{2a} \propto |T-T_c|$ by least squares fitting. The T_c determined from these power-laws of $\omega_{\min}$, $\omega_{\sigma-}$, and $\omega_{\sigma+}$ are 186, 187, and 190 K respectively. The estimated T_c here is 188 ± 3 K. Since the minimum position of the master function depends on the value of λ, the $\omega_{\sigma-}(T)$ systematically fails below the $\omega_{\min}(T)$.

Similarly, in fig. 4.7, we plot $\chi''_{\min}{}^2$ and $\chi''_\sigma{}^2$ vs T. Good linear fits are obtained in both figures, all extrapolating to a common zero at $T_c = 187 \pm 5$ K.

Table II. Fit parameters for β and α relaxation in PC.

	β relaxation				α-relaxation		
T(K)	$\omega_{min}/2\pi$ (GHz)	χ''_{min}	$\omega_\sigma/2\pi$ (GHz)	χ_σ	$\omega_{max}/2\pi$ (GHz)	τ_α (ns)	β
350					27.5	4.85e-3	0.737
330					20.7	6.45e-3	0.734
310					14.8	9.31e-3	0.753
295					10.3	1.35e-2	0.788
280					7.19	2.00e-2	0.823
270	728	1.92	311	1.57	5.39	2.63e-2	0.825
260	598	1.83	244	1.51	3.83	3.69e-2	0.804
250	511	1.69	227	1.38	2.68	5.36e-2	0.827
240	381	1.63	162	1.33	1.56	8.86e-2	0.789
230	260	1.49	114	1.22	0.882	1.65e-1	0.803
220	122	1.34	51.9	1.10	0.319	4.37e-1	0.780
210	68.4	1.12	30.9	0.927		1.33	0.760
200	29.3	0.816	12.4	0.678			
190	5.60	0.455	2.19	0.380			
180			12.4	0.645			
170			39.4	0.844			
160			105	1.04			
150			151	1.14			
135			208	1.30			

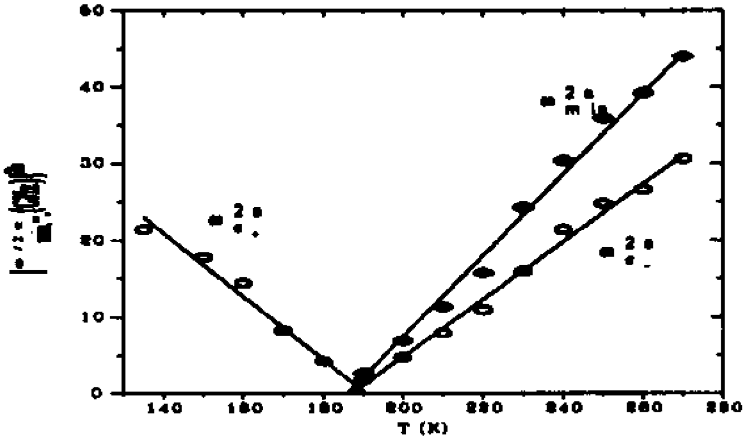

Fig. 4.6. $\omega_{\min}^{2a}$ vs T (♦, $T > T_c$) and $\omega_{\sigma-}^{2a}$ vs T (o). Extrapolation to $\omega = 0$ gives T_c=187±3 K.

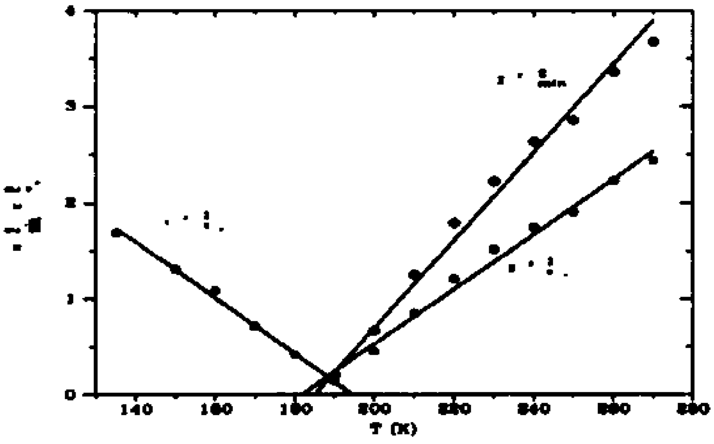

Fig. 4.7. $\chi''_{\min}{}^{2}$ vs T (♦, $T > T_c$) and $\chi''_{\sigma}{}^{2}$ vs T (o). Extrapolation to $\chi''=0$ gives T_c=187±5 K.

2. α-relaxation

a) Stretching and peak width of α-relaxation function.

The most important features of α-relaxation observed in supercooled glass-forming materials are the rapid increase of the relaxation time and strong non-Debye behavior of the relaxation function. As shown by MCT, the α–relaxation process depends on the microscopic structural details reflected in all the coupling constants $V^{(i)}$ of the memory function eq. (2.6). Although MCT does not predict an analytical function for the α-relaxation process, it was found that for $T > T_c$ the α-relaxation is governed by the scaling frequency ω_α. When the system is around the transition region, the correlation function obeys the time-temperature superposition principle and the α-peak position is controlled by the scaling frequency $\omega_\alpha \propto |T-T_c|^\gamma$ where $\gamma = 1/(2a) + 1/(2b)$.

A variety of phenomenological relaxation models has been proposed to quantitatively characterize the dynamics of α-relaxation. The single exponential Debye function predicts a symmetric susceptibility peak with a width of 1.14 decade. It can not describe the decay of glass forming materials which is stretched, with an asymmetric α-relaxation peak whose width is considerably larger than 1.14 decades. Although the MCT schematic F_{12} model predicts the stretching of the α-relaxation, it is not convenient to use it to fit the experimental spectra. The Cole-Davidson model, Havriliak-Negami model, etc.

have been used to study the stretching process in order to extract information that could be compared with predictions of MCT and configuration-space percolation theory (CSPT) [69], [70]. The generally accepted relaxation function is the stretched exponential (or KWW) function

$$\Phi(t) \propto \exp[-(t/\tau_\alpha)^{\beta_K}]. \qquad (2.32)$$

τ_α is the structural relaxation time and $\beta_K \leq 1$ is the stretching exponent. The scaling prediction of MCT eq. (2.31) is automatically satisfied by eq. (2.32) if β_K is independent of temperature. MCT shows that eq. (2.32), while not an exact solution of the MCT equations, provides a quite accurate representation of the α-relaxation spectrum.

b) Stretched exponential model fitting

In the frequency domain there is no analytical function for the stretched exponential model. Therefore, a numerical Fourier transformation of eq. (2.32)

$$\chi''(\omega)=(A\omega/k_BT)\,\mathrm{Re}\{\mathrm{F.T.}[\exp[-(t/\tau_\alpha)^{\beta_K}]\} \qquad (4.1)$$

was used to fit the spectra.

In the susceptibility spectra of fig. 4.2, α peaks are clearly visible for temperatures above 220 K. These α peaks were fitted to eq. (4.1) with amplitude A, τ_α, and β_K treated as fitting parameters. The value of τ_α is related to the peak position by $\omega_{max} = \omega_\alpha = 1/\tau_\alpha$, because $\omega_\alpha\tau_\alpha \leq 1$ for stretched exponential decay. For PC, the value of $\omega_\alpha\tau_\alpha$ can be directly calculated from Table II, which is about 0.9.

The high frequency tail of the α peak overlaps with the low frequency wing of the β-relaxation spectrum. In this part of the spectrum the stretched exponential decay gradually transforms to the von Schweidler power-law decay. The fitting region must therefore be limited in order to avoid interference from β-relaxation.

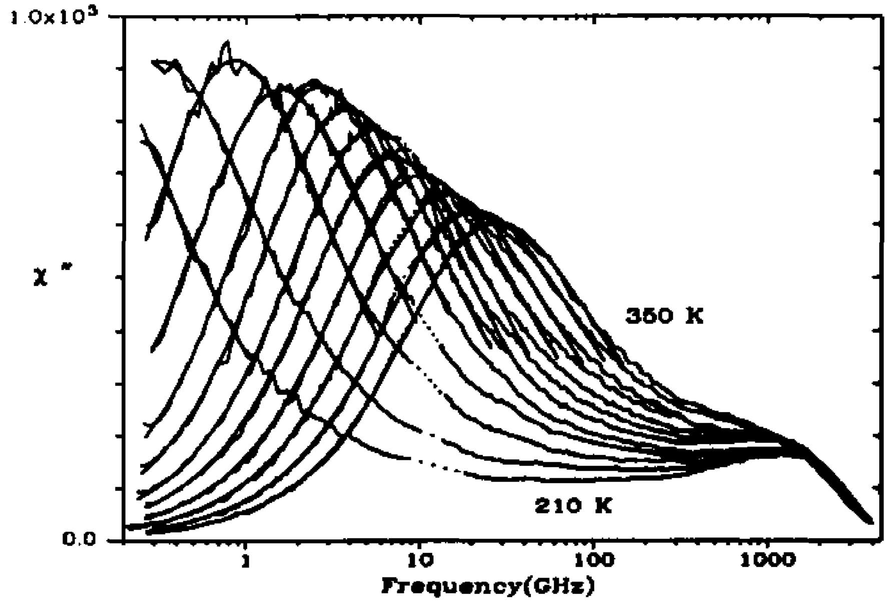

Fig. 4.8. α-relaxation region of the $\chi''(\omega)$ spectra of fig.4.2 fitted with eq. (3.2) for temperatures (from top to bottom) 350, 330, 310, 295, 280, 270, 260, 250, 240, 230, 220, 210, and 200 K.

Fig. 4.8 shows the susceptibility spectra for temperatures between 210 K and 350 K together with the fits to eq. (4.1). (note that the χ'' scale is linear in contrast to figs. (4.2)-(4.5).) The fit results for β_K, τ_α, and ω_{max} at each temperature are listed in Table II. Note that the high-frequency wings of the α peaks fall systematically above the fits, due to the onset of the β-relaxation process. (A different interpretation of this difference, not involving MCT, was suggested by Dixon et al. [71])

c) Temperature dependence of β_k

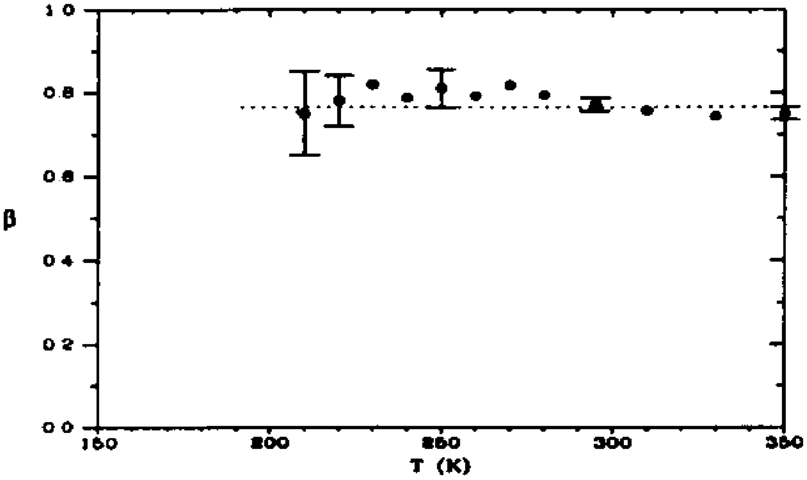

Fig. 4.9 Stretching constant β_k from the fits in fig. 4.8. The constant β_k fit indicated by the dashed line gave β_k= 0.77 ± 0.05.

The stretching constant β_K found from these fits is plotted against temperature in fig. 4.9. The data indicate that $\beta_K = 0.77 \pm 0.05$ with no evidence of a systematic increase with increasing temperature. Borjesson et al.[38] also found a temperature-independent β_K from their Brillouin scattering study of PC, although with a somewhat smaller value (β_K = 0.55). (Note that MCT predicts that β can be different for different physical variables.) The temperature-independent β_K indicates that the α-relaxation process obeys the time-temperature superposition principle eq. (2.31) predicted by the MCT. The value of $\beta_K < 1$ provides a critical test for the MCT and CSPT predictions. The CSPT predicts a Debye relaxation in the high-temperature liquid state with a stretching exponent $\beta = 1$ that decreases with decreasing T towards a non-Debye relaxation in the glass state with β = 1/3 [69], [70]. The above result $\beta_K = 0.77$ independent of T supports the prediction of MCT that α-relaxation is stretched even in the high-temperature liquid state and disagrees with the CSPT prediction.

d) Power law of α-relaxation time

The MCT prediction for the temperature-dependence of $\omega_{max}=1/\tau_\alpha$ is given by eq. (2.33)

$$(\omega_{max})^{1/\gamma} \propto (T-Tc). \tag{2.33}$$

The values of a and b found from the analysis of the β-relaxation process in the preceding section fix $\gamma=1/2a+1/2b=2.74 \pm 0.35$. In fig. 4.10 we plot $\tau_{\alpha}^{-1/2.74}$ vs T. The data show the predicted linear temperature dependence. Fitting of the data to a linear function of $\tau_{\alpha}^{-1/2.74} \propto (T-T_c)$ (Solid line), yields T_c=186±3 K, which agrees, within experimental error, with the results obtained from the analysis of the β-relaxation region.

e) Comparison of τ_{α} with viscosity results.

To further test the MCT prediction of eq. (2.33), the published viscosity data [24] was converted to viscous relaxation time τ_{η} with the Stokes-Einstein relation: $\tau_{\eta} = 4\pi R^3 \eta / 3 k_B T$, fixing R=1.7Å to match τ_{η} *with* τ_{α} at high temperatures. The high-temperature data, again plotted as $\tau_{\eta}^{-1/2.74}$ vs T, are approximately linear, and extrapolate to zero at Tc=188±3 K, close to the τ_{α} result. The fit is also shown in fig. 4.10 along with a fit of relaxation time of dielectric data.

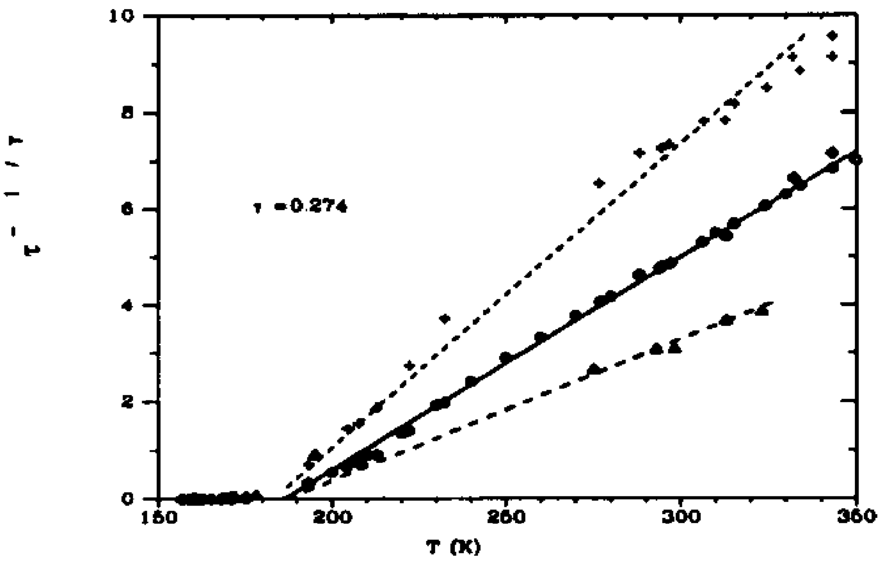

Fig. 4.10. The α-relaxation time obtained from the fits in fig. 4.8 plotted as $\tau_\alpha^{-1/\gamma}$ with γ=2.74 vs T (o). The best straight line fit gave T_c =186 K. Viscosity data (♦) [24] was converted to relaxation time τ_η by using the Stokes-Einstein relation $\tau_\eta = 4\pi R^3\eta/(3k_BT)$. (▲) are scaled from dielectric data [26], [22], [25], [28]. (+) are scaled τ values calculated from the same viscosity data [24], but using the Maxwell relation $\tau = \eta/G_\infty$. G_∞ is obtained by $G_\infty=\rho V_{TA}^2$. V_{TA} was determined from 90° depolarized spectra (temperature from 125 K to 190 K) and extrapolated to high temperature by assuming a linear temperature dependence. All three plots give a critical temperature around 185 K.

C. TESTING OF EXTENDED MCT

1. Fitting the β correlator spectra with λ fixed.

The idealized MCT discussed in section 4.B is a convenient but incomplete approximation to the full MCT. It produced characteristic system parameters T_c and λ.

However, systematic discrepancies appeared at the low frequency side of the spectra both below and close to T_c. This discrepancy has been observed in CKN and salol as well.

The idealized MCT predicts a complete structural arrest at T_c. The extended MCT includes ergodicity-restoring activated transport processes and replaces the sudden structural arrest by a gradual crossover from liquid dynamics to glassy dynamics; the α peak and susceptibility minimum both exist at all temperatures. In the extended MCT, the theoretical β-correlation function is determined by four parameters a, $h_1(T)$, $\sigma(T)$, and $\delta t_0(T)$ in eq. (2.34).

An extended MCT analysis of CKN and salol data corrected the deviations found with the idealized MCT in the low frequency wing of the β relaxation spectra [21]. The study was carried out for λ in the range determined by the $\delta = 0$ fits with arbitrarily chosen $t_0=(1/2\pi)$ ps. The exponent parameter a was fixed at a chosen value for all spectra of different temperatures, and the three parameters $h(T)$, $\sigma(T)$ and $\delta t_0(T)$ were varied to optimize the fit at each temperature to

$$\chi''(\omega) = h_{ls}\,\chi''(\omega,\sigma,\delta t_0) \tag{4.2}$$

by overlapping the calculated theoretical curve on the spectra and visually inspecting the agreement between them. A few sets of theoretically calculated curves with different a were compared with spectra to estimate the best value of λ.

The fits determined that in the vicinity of T_c both $h_{1s}(T)$ and $\sigma(T)$ could be represented by linear functions of T, while δt_0 was approximated by an Arrhenius function. It was also found that the optimum exponent parameter λ was slightly larger than for the idealized theory. Most importantly, it determined the width of the transition region ΔT and a trajectory in the (σ, δt_0) plane.

2. Extended MCT fits for PC

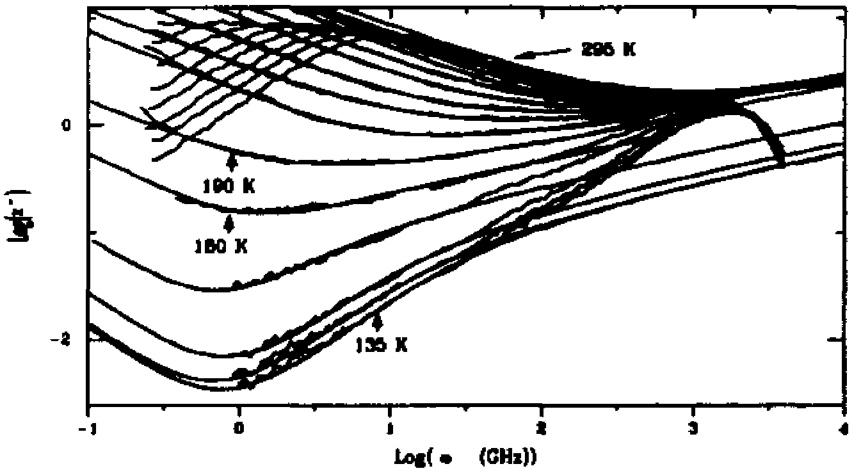

Fig. 4.11. Susceptibility spectra $\chi''(\omega)$ of PC fitted by $\delta \neq 0$ β-relaxation functions of the extended MCT. The fits use the same exponent $a = 0.29$ corresponding to $\lambda = 0.78$ obtained in the interpolation fits. The temperatures are (from top to bottom) 295, 280, 270, 260, 250, 240, 230, 220, 210, 200, 190, 180, 170, 160, 150 and 135 K. The arrows at 180 and 190 K indicate the growing effects of hopping processes in the crossover region.

An extended MCT analysis was carried out for PC following the above procedure, as has been reported [72]. The best fit was found for $\lambda = 0.78$. The fits are shown in fig.

4.11. Note that inclusion of $\delta \neq 0$ eliminated disagreements of the idealized MCT fits found in fig. 4.4 and fig. 4.5. The values of σ and δt_0 found from these fits are given in Table III.

Fig. 4.12(a) shows the separation parameter $\sigma(T)$ found from the fits together with the σ_0 lines determined from the δt_0 values via $\sigma_0 = \delta t_0^{2a/(1+2a)}$. The zero of $\sigma(T)$ defines the critical temperature $T_c = 179 \pm 2$ K. The crossover region is ~ 10 K. The amplitude $h_{ls}(T)$ is shown in fig. 4.12(b). Although the temperature dependence of h_{ls} in the vicinity of T_c is steep, it is still well represented by a linear function of T as found for CKN and salol.

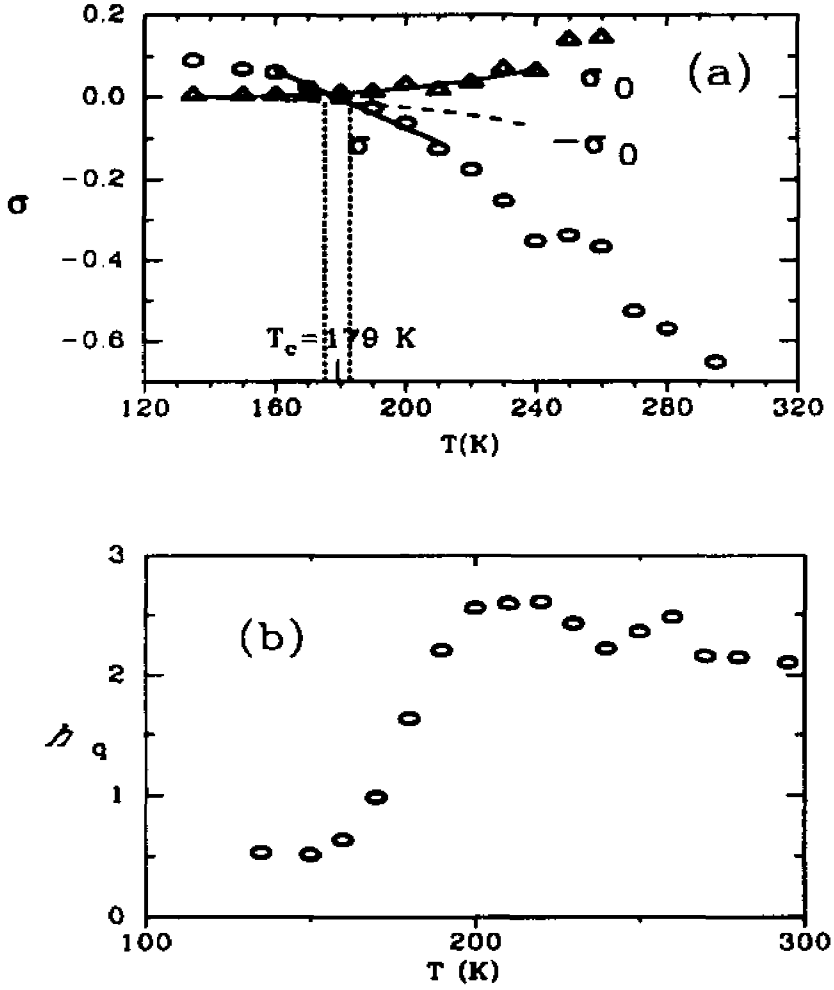

Fig. 4.12. (a) shows the separation parameter σ (o) and the hopping-induced scale ± σ_0 (Δ). The heavy straight solid line is a linear fit for $\sigma=A(Tc-T)$ in the temperature range $160 \leq T \leq 210$ K with $T_c = 179$ K. The solid line is an Arrhenius fit to σ_0 in the same temperature range. The dashed line is the $-\sigma_0$. The vertical dotted lines at $T = 175$ K and $T = 185$ K are estimated boundaries of the transition region. (b) The critical amplitude $h(T)$ vs. T determined from the extended MCT fits.

Table III. Fitting parameters for extended MCT analysis [t_0=(1/2π)ps]

T(K)	σ	δt_0	h
135	0.0904	7.16e-7	0.527
150	0.0692	6.92e-7	0.513
160	0.0622	1.03e-6	0.636
170	0.0283	1.50e-6	0.982
180	0.0039	5.55e-6	1.64
190	-0.0247	7.56e-6	2.20
200	-0.0618	9.14e-5	2.56
210	-0.126	1.78e-5	2.60
220	-0.176	1.24e-4	2.61
230	-0.253	7.07e-4	2.43
240	-0.353	5.86e-4	2.22
250	-0.339	4.73e-3	2.36
260	-0.367	5.23e-3	2.48
270	-0.527		
280	-0.571		
295	-0.652		

3. Global non-linear least square extended MCT fit of the β region of $\chi''(\omega)$ spectra.

Fitting the spectra with the visual inspection method produced useful preliminary results. To study this problem more objectively, a nonlinear least squares fitting was performed on the computer to improve the preliminary visual method results. In the fitting, the theoretical function was provided by numerically solving the β-correlator equation eq. (2.34) in each iteration.

a) Comparison of five fitting ranges

For $T > T_c$, the fitting program globally fits eight spectra from 250 K down to 180 K. For each spectrum, the values of σ, δt_0 and h_{ls} are varied independently, but the system-dependent exponent a is common for all spectra. The fitting is a time consuming process due to the iteration calculation of the differential-integral β-correlator equation.

As pointed out in the discussion of idealized MCT fitting, the α peak and the Boson peak enter the β-relaxation region gradually. There is no clear-cut boundary between the two relaxation regions. Five different fitting regions were explored to study this effect as shown in fig. 4.13. For cases (a), (b), and (c), the region is determined by arbitrarily drawn straight lines. In case (d), the high and low frequency limits of the fitting region are taken as one decade above and one decade below ω_{min}, respectively (some of the regions are shorter due to the presence of the boson peak). In case (e), the range is determined by the scaling region of the $\delta=0$ master function fitting described in section 4B.

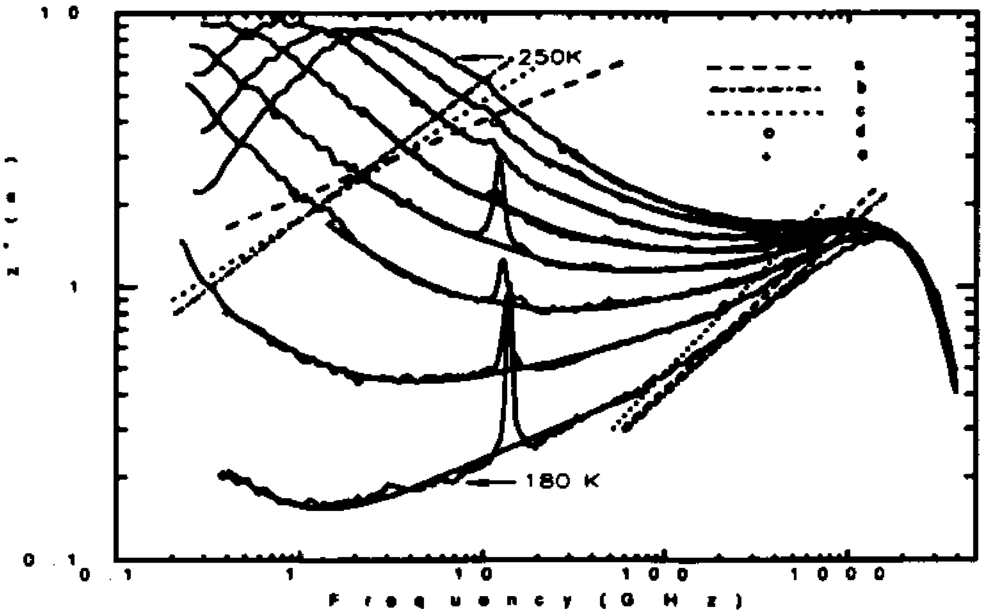

Fig. 4.13. Global fitting. The fitting regions are marked by line a, b, c, and point d, and e. Temperatures are from 180 to 250K in steps of 10 K.

The critical exponents a from these different cases are $a_a=0.236$, $a_b=0.252$, $a_c=0.264$, $a_d=0.255$, and $a_e=0.266$. The corresponding exponent parameters λ are from 0.89 to 0.82. Comparing the fitted functions with data in all these cases, the case (e) is the best one, because deviations of the spectra at the ends of the fitted curves show a consistent tendency to fall below the fitted theoretical curves for all temperatures. The value of a_e = 0.266 is smaller than the one found in the idealized MCT fits, due to the correction of the hopping effect.

b) Fits for $T < T_c$,

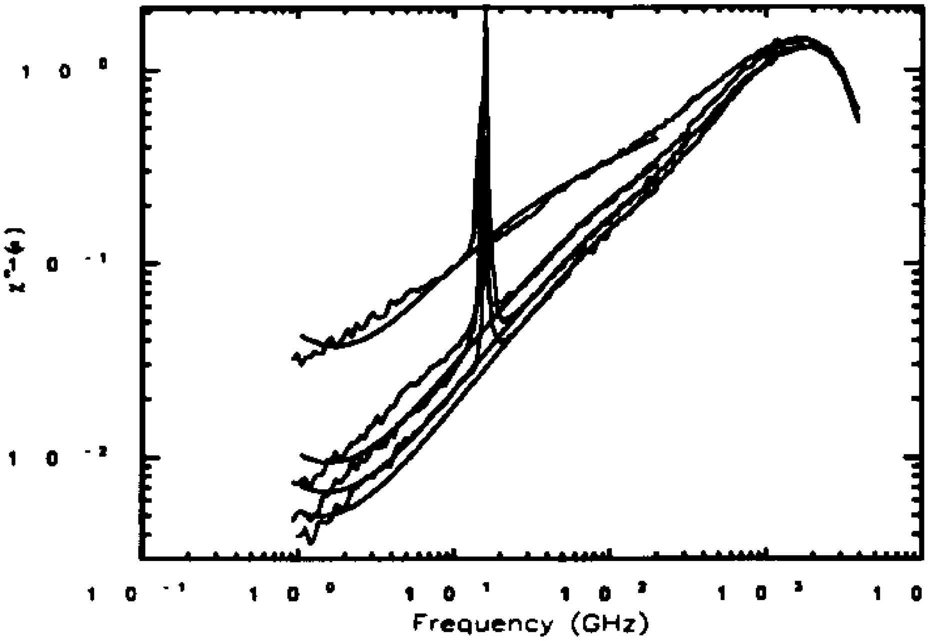

Fig. 4.14. Extended MCT fits with $a=a_e=0.266$. The temperatures are (from top to bottom) 170, 160, 150, and 135 K.

For $T < T_c$, the spectra do not show either the knee or the minimum in the frequency region studied. The fitting of spectra therefore was carried out individually for temperatures from 170 to 135 K. For each spectrum, σ, δt_0, and h_{1s} are fitting parameters. The exponent a is fixed to the value obtained in the $T > T_c$ global fitting case (e) a_e=0.266.

About one decade of the low frequency part of the spectrum was chosen as the fitting region. Fig. 4.14 shows the fitted results.

The average slope of the fitted curve agrees with the data. On the low frequency side, the fits are systematically below the spectra. Changing the value of a basically produced the same results. The fits provided the $\sigma(T)$, $\delta t_0(T)$, and $h_{ls}(T)$ for the glass state.

c) *Effects of the fitting region on $\sigma(T)$, $\delta t_0(T)$ and $h_{ls}(T)$*

The optimized fitting parameters σ and δt_0.for both liquid and glass states are plotted, as a function of temperature, in fig. 4.15.

The results obtained with different fitting regions are essentially consistent. The change of fitting range does not change the optimized fitting parameters for temperature around T_c. Deviations between the fitting parameters due to using different fitting regions become significant only when T is far from T_c. For $140 < T < 240$ K, the separation parameter $\sigma(T)$ was found to vary linearly with temperature as discussed in the theory.

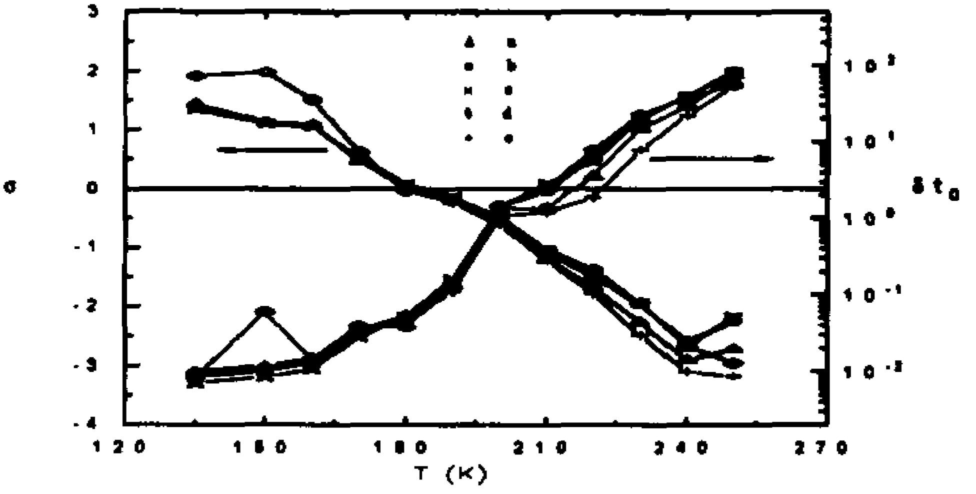

Fig. 4.15. Temperature dependence of σ (*T*) and $\delta t_0(T)$ of five fitting ranges.

d) Arrhenius law for the hopping parameter δt_0 and transition region ΔT_c

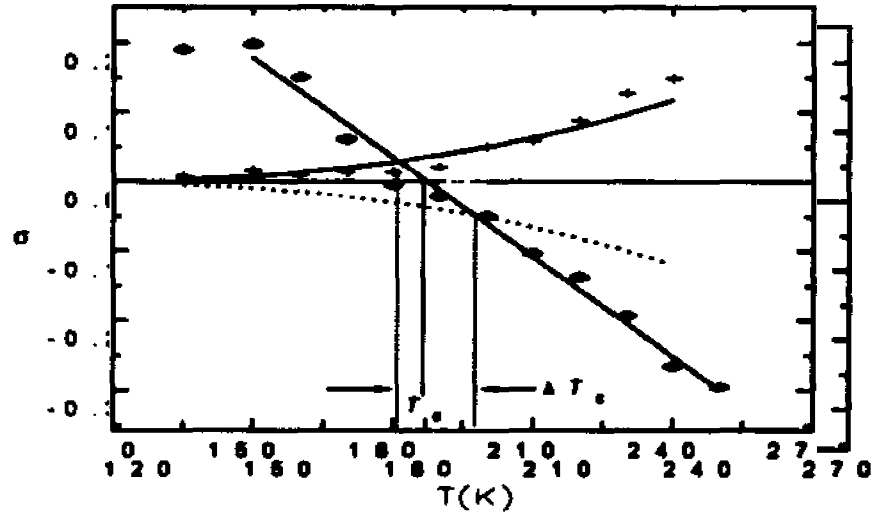

Fig. 4.16. The separation parameter σ(*T*) determines the critical temperature T_c and the transition region ΔT_c.

The parameters obtained from fit (e) were used to determine the critical temperature T_c and the width of the transition region ΔT_c. The result is shown in fig. 4.16. The separation parameter σ was fitted with a linear function $\sigma \propto (T-T_c)$. It yielded T_c = 187 ± 3 K, which is somewhat higher than the T_c found in the visual inspection fitting, but basically agrees with the previous idealized MCT study estimates.

Since in the extended theory, the hopping effect results from thermally activated process [73], the hopping rate δt_0 follows the Arrhenius law $\delta t_0 \propto \exp(E/T)$. This prediction has been tested in visual inspection fits of CKN, salol, and PC. To explore other possibilities, a Volger-Fulcher law $\delta t_0 \propto \exp(E/(T-T_0))$ fitting was performed. The crossover temperature T_0 and activation energy E were fitting parameters. It was found that T_0 and E are strongly correlated and the fitted result is not stable. Therefore the hopping rate δt_0 was fitted with an Arrhenius function.

Both $\delta t_0(T)$ and the fitted results are converted into the hopping-induced scale σ_0 via $\sigma_0 = (\delta t_0)^{(2a)/(1+2a)}$ to determine the transition region ΔT_c. The crossing points of σ_0 and $-\sigma_0$ with $\sigma(T)$ determine the low and high limits of the transition region. The result is plotted in fig. 4.16. ΔT_c is found to be ~ 18 K which is slightly larger than the result of the visual inspection fitting.

e) Two parameter scaling law, Trajectory in σ, δt_0 parameter space

This fitting also established the system trajectory in the (σ, δt_0) parameter space that is followed by the system from the liquid region throughout the transition region, and into the region of glassy dynamics as the temperature is decreased. The trajectory is plotted in fig. 4.17. It crosses different scaling lines where $\delta t_0 = C|\sigma|^{(1+2a)/2a}$ as T decreases so that simple T-scaling does not apply. This explains why the idealized MCT scaling is only an approximate.

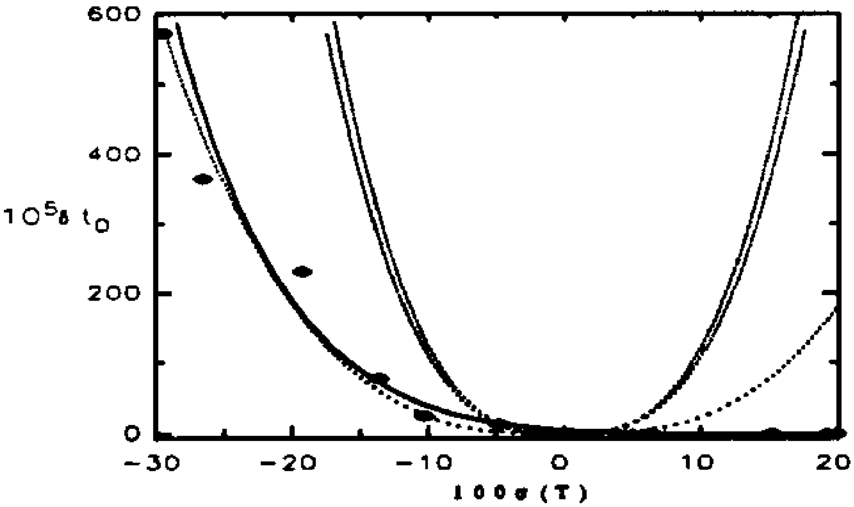

Fig. 4.17. Trajectory of the system in (σ, δt_0) parameter space.

When hopping terms are included, the α-relaxation peak will exist below T_c and the susceptibility spectra therefore continue to show a minimum. This could be seen from the 180 K spectrum in fig. 4.13. Taking $T_c = 187$ K and $\Delta T_c = 18$ K, the system is in the glass side of the transition region at 180 K. However, the spectrum shows a minimum that is the characteristic of liquid dynamics. The 180 K spectrum provides evidence that for $T < T_c$ the α–relaxation still exists as it does in dielectric susceptibility data. It is the hopping process that causes the a-relaxation to occur for $T < T_c$.

f) Comparison of extended fits with idealized fits.

It is interesting to compare the fitting results of the two versions of MCT. The critical exponent a found in the extended MCT fitting is about 0.27 which is slightly smaller than the value found in the idealized fits (a=0.29). In the extended theory, both the hopping process and von Schweidler decay (ω^{a}) contribute to the low frequency part of the β-relaxation region. The contribution from the hopping process compensates for the smaller contribution from the von Schweidler decay.

g) Test of the effect of h_{ls} on the exponent a by $\log[\chi''(\omega)] \propto \log(\omega_{a})$

The amplitude $h_{ls}(T)$ is shown in fig. 4.18. h_{ls} is a constant when the system is in the glass state. Around the transition region, h_{ls} increases linearly with increasing temperature. As the system enters the liquid state, h_{ls} reaches another constant value. The linear temperature dependence of h_{ls} in the transition region agrees with the prediction of extended MCT. The increase of $h_{ls}(T)$ with increasing of T can be understood by considering the cancellation effect of the DID model [74] .

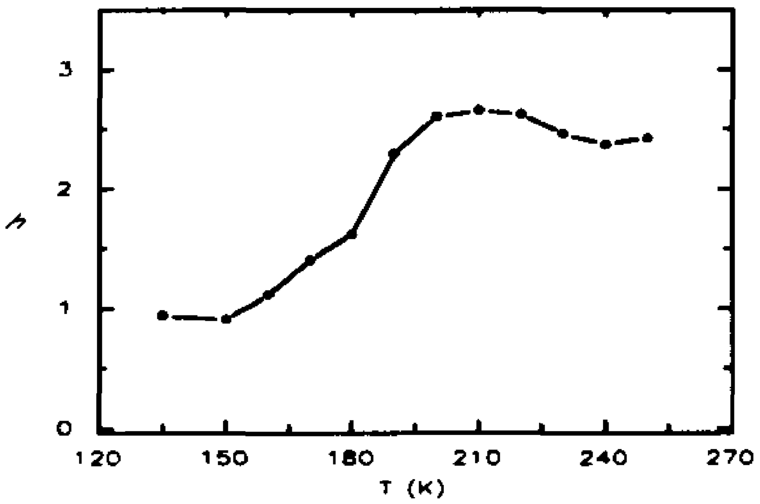

Fig. 4.18. The T dependence of $h_{ls}(T)$ found in the extended MCT analysis case (e).

The idealized MCT prediction of eq. (2.28) $\chi''(\omega) = h_{ls}\ |\sigma|^{1/2}\chi''_{\pm}(\omega/\omega_\sigma)$, with h_{ls} assumed to be constant, leads to the prediction that a_{eff}, the slope of $\log(\chi''_{min})$ vs. $\log(\omega_{min})$, should be equal to a.

Fig. 4.18 shows that $h_{ls}(T)$ is actually dependent on T; therefore, χ''_{min} will increase faster than $|\sigma|^{1/2}$ and a_{eff} should be larger than a. This result $a_{eff} > a$ was found in our previous studies of CKN and salol, and was explained on the basis of the temperature dependence of h_{ls}(T) [21].

In fig. 4.19 we show the experimental [log(c"min), log (wmin)] values for PC by open circles, with a linear fit that gave aeff = 0.32. A straight line with slope a=0.29, the value found in idealized theory analysis, passing through the lowest point is also shown to illustrate that $a_{eff} > a$.

We recalculated the predictions of eq. (2.28) with $a = 0.29$ including the temperature dependence of $h_{ls}(T)$ shown in fig. 4.18. The results are shown by the o symbols in fig. 4.19. Thus the apparent failure of eq. (2.28) is eliminated when the T dependence of $h_{ls}(T)$ found in the extended MCT analysis is included.

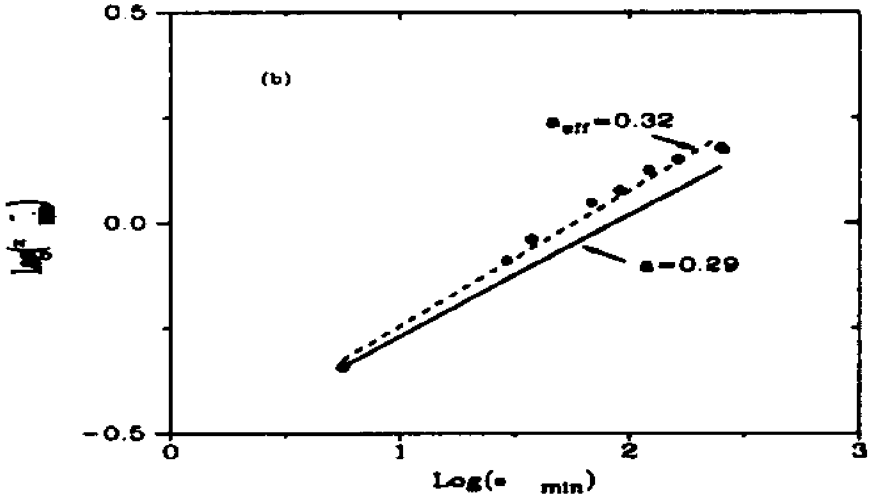

Fig. 4.19. Double logarithmic plot of χ''_{min} vs ω_{min} with the experimental values shown by (◊). A linear fit shown by the broken line gave $a_{eff} = 0.32$, in clear disagreement with the idealized MCT prediction $a_{eff}=a= 0.29$ shown by the solid line. (o) indicated the modification of the prediction when the temperature dependence of $h(T)$, shown in fig. 4.18 is included as discussed in the text.

D. HYDRODYNAMIC STUDY OF LA MODE

1. Hydrodynamic theory study of fq factor and previous experiments.

a) Review the relation of f_c with C_0 and C_∞

Fuchs, Gotze, and Latz [16] noted that the non-ergodicity parameter $f_q(T)$ can be determined in the $q \to 0$ limit by

$$f_0 = 1 - (C_0/C_\infty)^2, \qquad (2.41)$$

where C_0 and C_∞ are the sound velocities measured below or above the α-relaxation frequency region. The square-root cusp of $f_q(T)$ for any q determines T_c. C_0 and C_∞ can be determined from the LA mode of Brillouin spectra by fitting with the generalized hydrodynamic theory. Elmroth, Borjesson, and Torell's study of PC determined T_c as 270 K [17]. This result is questionable because it is ~ 60 degree higher than the melting temperature T_m. Three aspects of the experimental and data analysis procedures may have contributed to their high value of T_c. First, the I_{vv} spectra were analyzed directly without subtraction to remove anisotropic scattering contributions; second, C_0 and C_∞ were both treated as free fitting parameters; and third, structural relaxation was represented by an α-relaxation only model (Cole-Davidson) so that β-relaxation effects were ignored. We therefore further studied this problem by using the generalized hydrodynamic theory.

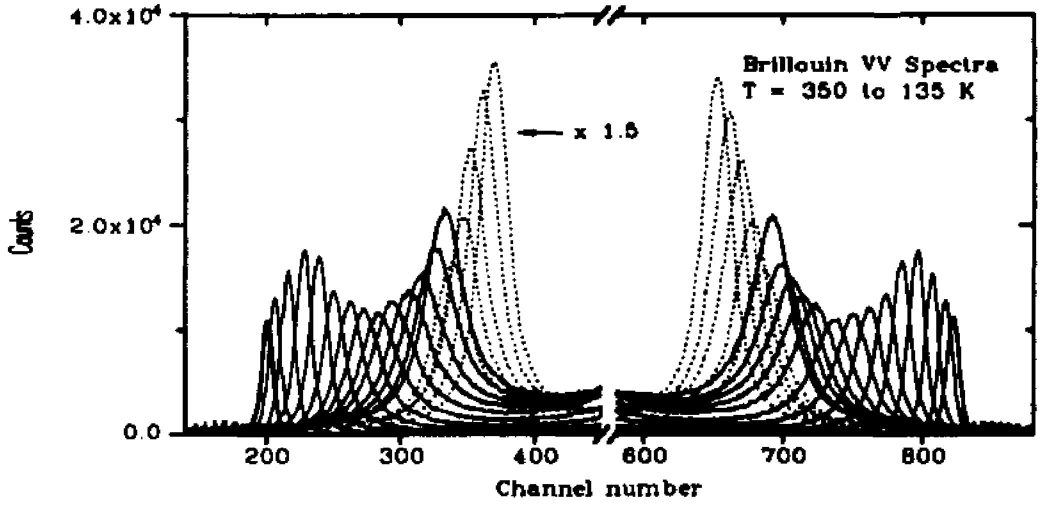

Fig. 4.20. The raw data of VV scattering of Brillouin spectrum. Temperatures are the same as in fig. 4.1.(The intense elastic component has been removed by a shutter.)

2. Polarized Brillouin Scattering Experiment on PC

a) Experimental procedure , I_{VV}, I_{VH}, I_{LA} spectra.

We recorded $\theta = 172$ ° VV and VH tandem interferometric spectra of PC with a mirror separation of 6 mm (FSR = 25 GHz). The raw data of the I_{VV} spectra are shown in fig. 4.20.

The I_{VV} spectra include contributions from the scattering of longitudinal density fluctuations I_{LA}, anisotropic scattering from orientational fluctuations, and second-order

DID scattering [14], while the I_{VH} spectra contain the orientational and second-order anisotropic scattering only. The pure I_{LA} spectra can be obtained by subtraction:

$$I_{LA} = I_{VV} - KI_{VH} \tag{4.3}$$

where K is a constant determined from the depolarization ratio at frequencies well above the Brillouin peak [19]. For PC, we found K=1.24.

Fig. 4.21 shows the I_{VV} and I_{VH} spectra for T=250 K, and the corrected I_{LA} spectrum found with eq. (4.3). Note that the I_{LA} spectrum is qualitatively different from the uncorrected I_{VV}

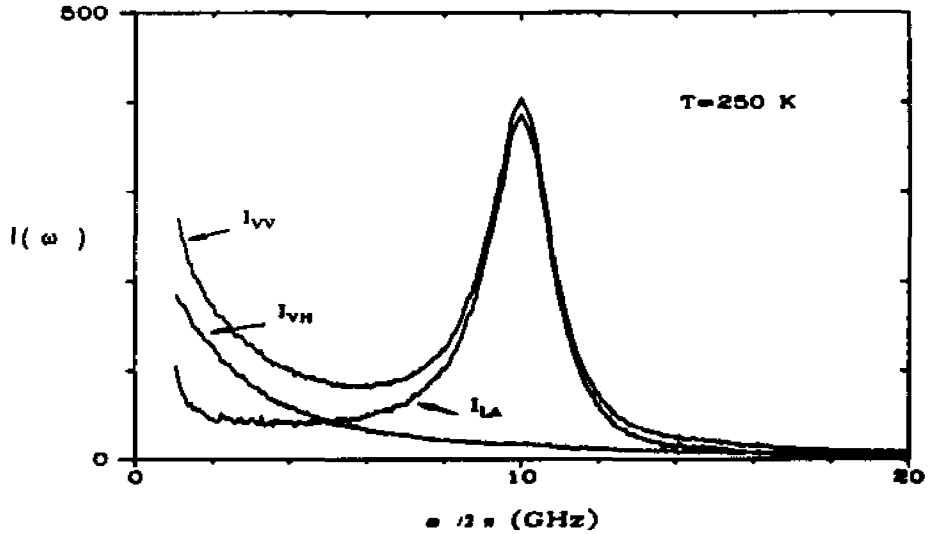

Fig. 4.21. θ = 172 ° I_{VV} and I_{VH} Brillouin spectra for T=250 K and the longitudinal spectrum I_{LA} found with eq. (4.3). Note that the subtraction strongly modifies the shape of the spectrum for frequencies below the Brillouin peak.

spectrum at frequencies below the Brillouin peak, indicating that orientational and second-order scattering processes make significant contributions to I_{VV}.

b) Fitting function.

The spectrum of longitudinal fluctuations including the interaction of LA modes with structural relaxation was fitted with

$$I(\omega) \propto \frac{S(q,\omega)}{S(q)} = \frac{\omega_0^2(\gamma_0 + m''(\omega))}{\pi\{[\omega^2 - \omega_0^2 + \omega m'(\omega)]^2 + [\omega(\gamma_0 + m''(\omega))]^2\}} \tag{2.37}$$

where $\omega_0 = C_0 q$, and γ_0 is a regular damping constant. The dynamics of structural relaxation enters eq. (2.37) via the complex memory function $m(\omega)$.

We first used the conventional Cole-Davidson model and later constructed a hybrid model to represent the memory function in this study. The Cole-Davidson (CD) function is

$$\omega m(\omega) = \Delta^2[(1 - i\omega\tau_{CD})^{-\beta_{CD}} - 1] \tag{2.39}$$

where Δ^2, τ_{CD}, and β_{CD} are treated as adjustable fitting parameters.

c) Independently determined C_0 and β

In order to reduce the number of free parameters in eqs. (2.37) and (2.39), we fixed β_{CD}, γ_0, and $C_0(T)$ leaving I_0, Δ^2, and τ_{CD} as the three free fitting parameters. From the fits to α-relaxation peaks discussed in Sec. 4.B.2, we found $\beta_K = 0.77$. This β_K is converted to the Cole-Davidson stretching exponent β_{CD}=0.68 via the equation $\beta_K = 0.683\ \beta_{CD} + 0.316$ [30]. The fitting produces the τ_{CD}. The corresponding conversion for τ_K is $\tau_K = \tau_{CD}.(1.184\beta_{CD} - 0.184)$. The conversed value of τ_K is listed in Table IV. From the width of the LA Brillouin peak at 125 K (the lowest temperature studied) we determined $\gamma_0/2\pi$=0.1 GHz. We assumed that β_{CD} and γ_0 are independent of temperature in this CD model fitting.

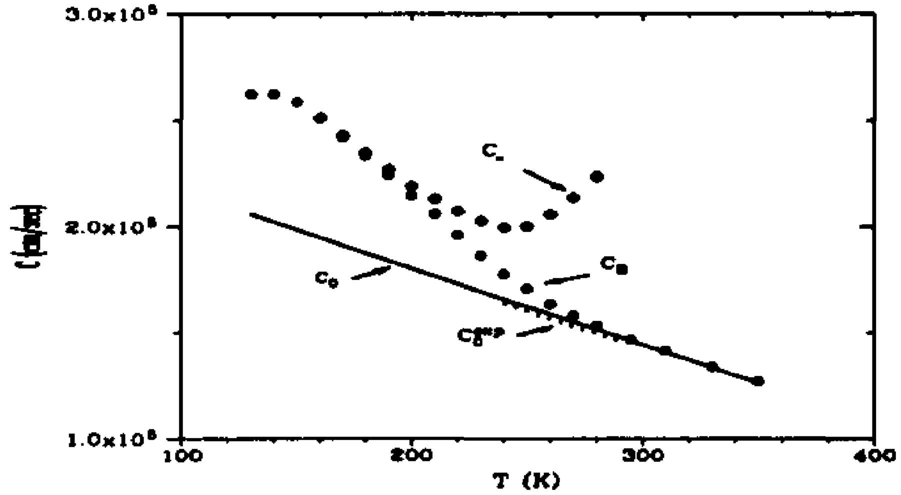

Fig. 4.22. Sound velocity C_0 from ultrasonic measurements (dotted line), C_B from Brillouin peak positions (∘), C_∞ from the fits of fig. 14 (•). The solid line is the adjusted C_0 used in the fits of fig. 4.23.

To determine independently the low-frequency sound velocity $C_0(T)$, ultrasonic measurements were performed at 5 MHz for temperatures between 293 and 240 K by using the PSD method described in Chapter III. Ultrasonic measurements at 5 MHz and 15 MHz down to 213 K showed measurable dispersion beginning at ~ 230 K, indicating that measurements at $T \leq 230$ K were no longer determining C_0 due to the rapidly increasing relaxation time. Therefore the measured C_0 values in the range 293 K to 240 K, where no dispersion was observed, were fitted with a linear function, which gave

$$C_0(T) = 2507.5 - 3.612T \quad \text{(m/sec)} \tag{4.4}$$

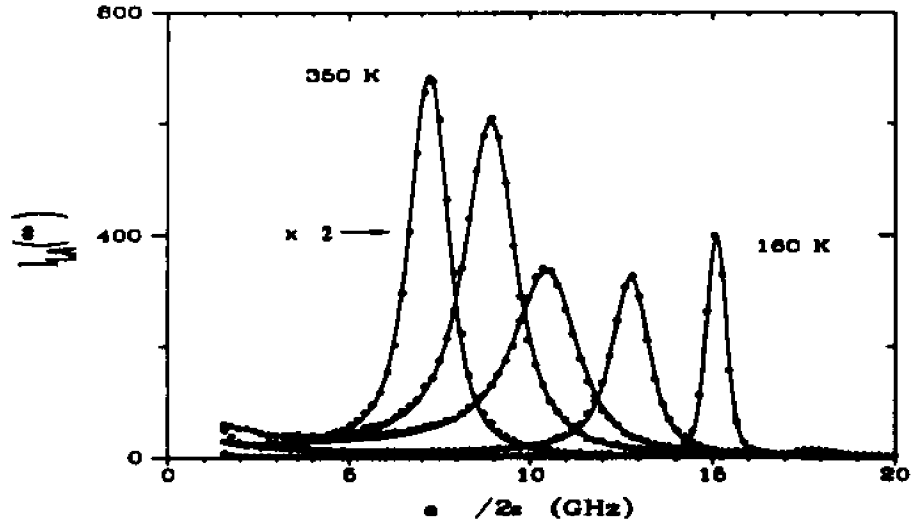

Fig. 4.23. Fits of I_{LA} spectra to the generalized hydrodynamic results eq. (2.37) with the Cole-Davidson model as memory function. I_0, Δ^2, and τ_{CD} are fitting parameters, with β_{CD} fixed at 0.68 (from β_{α} =0.77). Temperatures are (from left to right): 350, 280, 240, 200 and 160 K. (•) are experimental data, solid lines are the fitted results.

shown by the dashed line in fig. 4.22. (This C_0 result differs by about 1% from that reported by Masood et al. [31]) The ultrasonic $C_0(T)$ in eq. (4.4) was used in the fitting, but with a slight correction by +0.85%, which is within the experimental error of the ultrasonic measurement, in order to obtain agreement between ω_B and C_0 at high temperatures. Fits for five temperatures are shown in fig. 4.23. The resulting values of τ_{CD}, τ_K, Δ^2, and $C_\infty=[C_0{}^2 + (\Delta/q)^2]^{1/2}$ are listed in Table IV. The C_∞ values are also plotted in fig. 4.22 along with C_0 and with C_B determined from the positions of the Brillouin peaks. The nonergodicity parameter $f_0(T)_{CD}$ computed with eq. (2.41) and the Cole-Davidson relaxation model is shown in fig. 4.24 by (◊). Note that the fits shown in Fig. 4.23 are quite good, despite the fact that the fit parameters and $f_0(T)$ values are rather different from those in ref [17]. This demonstrates the extreme difficulty of inferring the memory function from conventional Brillouin scattering spectra.

Table IV. Fit parameters for the LA mode with CD memory function.

T(K)	τ_{CD}(ns)	τ_k(ns)	Δ	C_0(cm/s)	C_∞(cm/s)	f_0
160	4.03	2.50	91.3	1.95e5	2.52e5	0.398
170	1.20	0.746	80.9	1.91e5	2.43e5	0.380
180	0.412	0.256	71.7	1.88e5	2.35e5	0.362
190	0.204	0.127	63.1	1.84e5	2.27e5	0.342
200	0.102	6.36e-2	55.0	1.81e5	2.19e5	0.322
210	5.65e-2	3.63e-2	49.9	1.77e5	2.13e5	0.311
220	3.45e-2	2.15e-2	45.4	1.73e5	2.07e5	0.301
230	2.32e-2	1.40e-2	43.0	1.70e5	2.03e5	0.299
240	1.60e-2	9.92e-3	42.9	1.66e5	2.00e5	0.309
250	1.15e-2	7.12e-3	47.7	1.63e5	2.01e5	0.343
260	7.23e-3	4.48e-3	59.2	1.59e5	2.06e5	0.405
270	5.06e-3	3.14e-3	73.9	1.55e5	2.14e5	0.472
280	3.55e-3	2.20e-3	92.0	1.50e5	2.24e5	0.540

d) The problem of using the Cole-Davidson model as memory function.

The use of the Cole-Davidson approximation, or any model for $m(\omega)$ which neglects β-relaxation contributions to $m(\omega)$, will generally result in fit parameters of questionable physical significance. This is because the parameters used to model the α-relaxation must be severely distorted to account for the β-relaxation as well once the α peak frequency is below the Brillouin peak [19]. But introducing additional parameters results in fits which may be even less reliable. One therefore seeks to represent $m(\omega)$ by a function that includes the β-relaxation process.

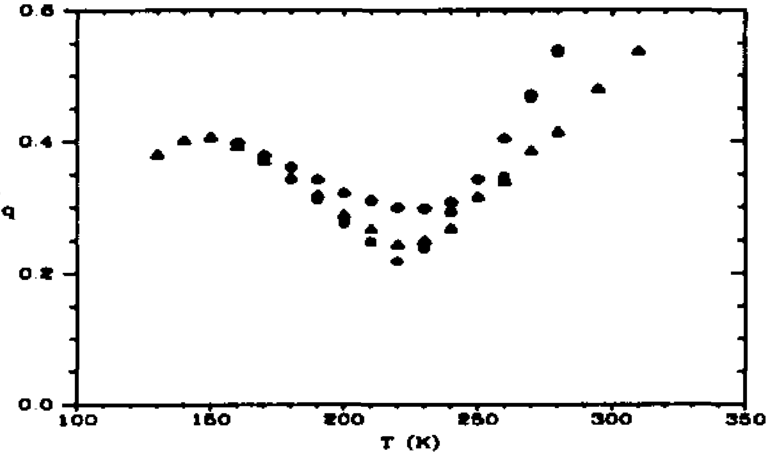

Fig. 4.24 Nonergodicity factors $f_{CD}(\Diamond)$, $f_B(o)$, and $f_\rho(\Delta)$ deduced from fitting parameters of the three different fitting methods [CD, hybrid with B'' free and γ_0 fixed, hybrid with B'' fixed and $\gamma_0(T)$ following a linear temperature dependence, respectively] with eq. (2.41). The three results overlap on the low temperature side. There are minima in all three curves around 220 K.

e) Comment on empirical memory function

In our Brillouin scattering study of CKN [19], an empirical memory function $m(\omega)$ containing both α- and β- relaxation contributions was constructed by identifying $m''(\omega)$ with the depolarized light scattering spectrum. It was based on the assumption that the structural relaxation dynamics probed by the LA mode are identical to the dynamics responsible for the depolarized light scattering. For CKN, this ansatz was justified by the observation that the α-relaxation peak in the depolarized spectrum crosses the LA mode at the temperature where the LA mode linewidth is a maximum, so that τ_α is about the same for both processes.

f) Measurement of ω_{LA}, $\Delta\omega_{LA}$, *and* ω_{max}

However, this is not the case for PC. Fig. 4.25 shows the temperature dependence of the LA mode peak frequency ω_{LA}, width $\Delta\omega_{LA}$, and the α peak frequency ω_{max} of the depolarized light scattering spectrum of PC. The width of the LA mode is maximum at $T \approx 240$ K, while the crossover of the LA mode frequency and the α peak frequency is at $T \approx 290$ K. At 240 K, τ_α (Brillouin) determined by $\omega_{LA}\tau_\alpha = 1$ is about five times shorter than τ_α of the depolarized spectrum. Similar results have been observed in the studies of di-2-ethylhexyl phthalate [75] and salol [18].

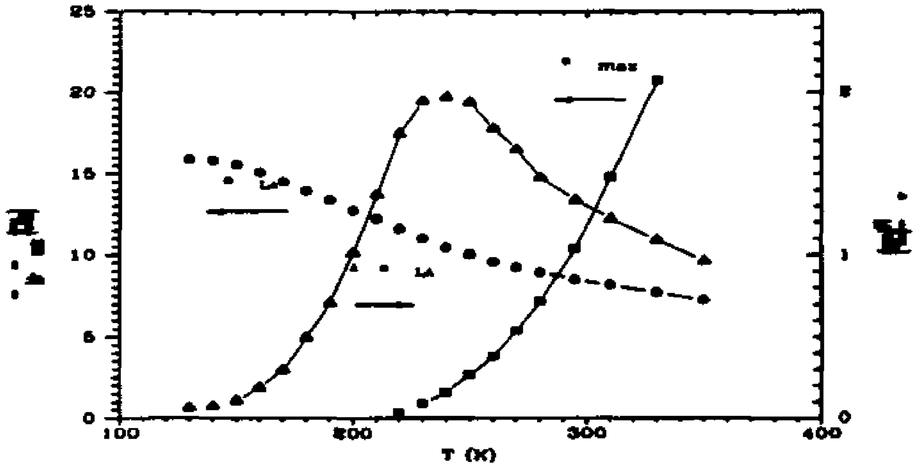

Fig. 4.25. Temperature dependence of the LA mode ω_{LA} and linewidth $\Delta\omega_{LA}$, and the α-relaxation peak ω_{max}. The maximum width of the LA mode occurs at T ~ 240 K. At this temperature, the α-peak frequency is about five times smaller than the LA mode peak frequency.

g) Hybrid memory function model

Since for PC the depolarized light scattering spectrum and the LA mode seen in the Brillouin scattering spectrum evidently reflect different structural relaxation dynamics, the use of the empirical model for $m(\omega)$ cannot be justified for PC. We have therefore made a preliminary attempt to find $m(\omega)$ by combining the Cole-Davidson expression for the α-relaxation with the MCT prediction for the critical decay which is the high-frequency power law wing of the β-relaxation spectrum. The resulting hybrid model for $m(\omega)$ is

$$m(\omega)=m_{CD}(\omega)+B\omega^{a} \tag{4.5}$$

where B is a (complex) parameter and $m_{CD}(\omega)$ is the CD function of eq. (2.39). (The real and imaginary parts of B are proportional to the cosine and sine parts of the Fourier transform of t^{-a}.

In fig.4.26, we plot τ values for PC from several different experiments. (o) is the τ_{CD} from our CD-model fits. (□) are the τ_α results from the depolarized spectra. Note that the τ_{CD} values fall below the τ_α values and the discrepancy increases at low temperatures. MCT predicts that while τ_α for different processes may be different, all should follow a common temperature scale. We therefore fixed τ_{CD} by taking the ratio of τ_α to τ_{CD} at 240

K where τ_{CD} is set by ω_{LA} and τ_α is set by the position of the α peak ω_{max}, and then divided τ_α at each temperature by this same ratio which is 5. The resulting τ'_{CD} is shown in fig. 4.26 by the dot-dash curve.

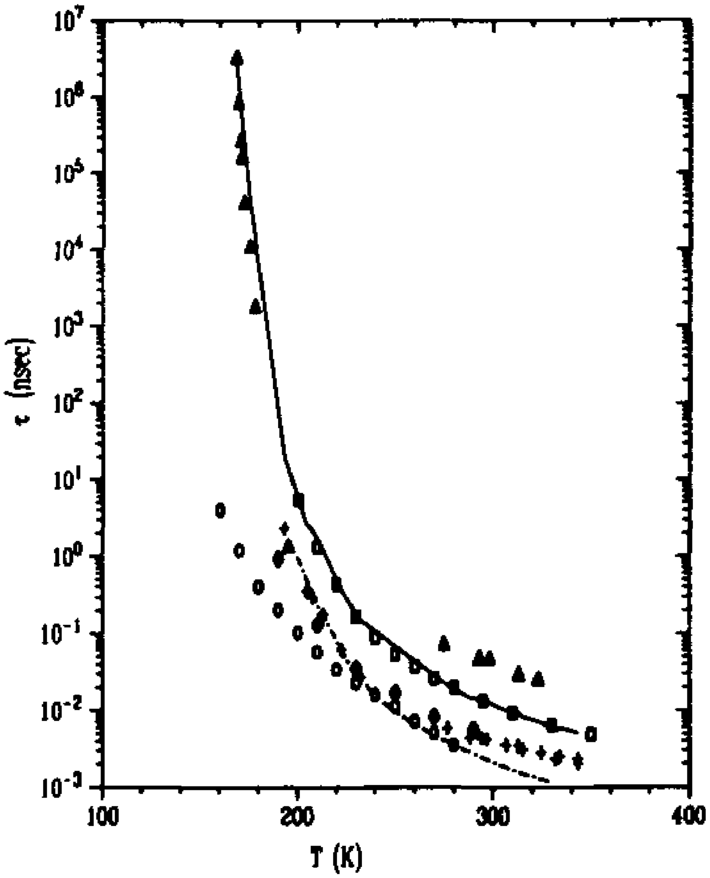

Fig. 4.26. Relaxation time τ_α for PC from various experiments: depolarized light scattering (□), τ_{CD} (o) from the fits of fig. 4.23. The solid line is τ_η calculated from viscosity data [34] by using the Stokes-Einstein relation with $R=1.7$ Å. (+) is $\tau_{\eta M}$ calculated from viscosity data using the Maxwell method. The (·-·-) line is the calculated τ'_{CD} value used in the hybrid model fits discussed in the text. (▲) are results from dielectric measurements [25], [22], [26], [28]. (♦) are neutron scattering results [37].

With this τ'_{CD}, we carried out fits with the hybrid model with β_{CD}=0.68, the same as in the pure CD fitting, and with a=0.29 obtained in the β-relaxation analysis in Section 4B1. The fitting parameters were I_0, Δ^2, and B''. This hybrid model gave reasonable fits, but the temperature dependence of the resulting Δ^2, as in the pure CD model analysis, still had an anomalous increase for temperatures higher than – 230 K. We also found that Δ^2 and B'' are strongly correlated. Fitting with fixed B'' by constraining it to follow a linear temperature dependence with adjustable slope was also attempted, but reasonable fits for each spectrum in the whole temperature range could not be obtained. We also tried using fixed B'', allowing γ_0 to follow a linear temperature dependence. The fits were reasonable but Δ^2 still had an anomalous temperature dependence as in the other cases.

3. Non-ergodicity factor

a) Analysis of temperature behavior of non-ergodicity factor.

Fig. 4.24 shows the nonergodicity factors f_0 deduced from the fits via eq. (2.41) for the three different analyses. The f_q minima observed near 220 K in Fig. (4.24) are not believed to be significant. There is no evidence for a cusp near 187 K which is expected to occur if eq. (2.41) is valid. (The only apparent feature is a minimum around 230 K) These results indicate that the hybrid model of eq. (4.5) (or the constrained parameters employed in the fitting procedure) may not be adequate to describe $m(\omega)$. Although a more flexible model could be obtained by also allowing β_{CD} to vary freely, experience suggests that increasing the number of fitting parameters would produce fits of dubious significance. We therefore conclude that the determination of T_c from Brillouin scattering experiments via eq. (4.1) is not reliable unless the memory function can be independently determined.

E. TRANSVERSE ACOUSTIC (TA) MODE AND BOSON PEAK

1. Measurement of TA mode.

a) Transverse acoustic mode and shear relaxation time

In fluids containing optically and mechanically anisotropic molecules, the transverse velocity couples to the molecular orientations, and therefore can produce a transverse acoustic (TA) mode. The TA mode can only exist as a propagating underdamped excitation when the shear modulus relaxation time is larger than the relaxation time of the density fluctuation. The scattered light due to the TA mode is depolarized, i.e. polarized in the scattering plane. It is exactly forbidden at $\theta = 180°$ scattering angle. For these reasons, a well-defined transverse mode can only be seen at low temperatures in a depolarized non-backscattering geometry.

Fig. 4.27 shows the $\theta = 90°$ depolarized spectra. The peaks appearing at frequencies below 6 GHz are the transverse acoustic (TA) Brillouin modes. The frequency and linewidth of the TA modes were determined by nonlinear least squares fitting to

Lorentzian model and are plotted in fig. 4.28. The peak frequency ω_{TA} decreases and the linewidth increases with increasing temperature.

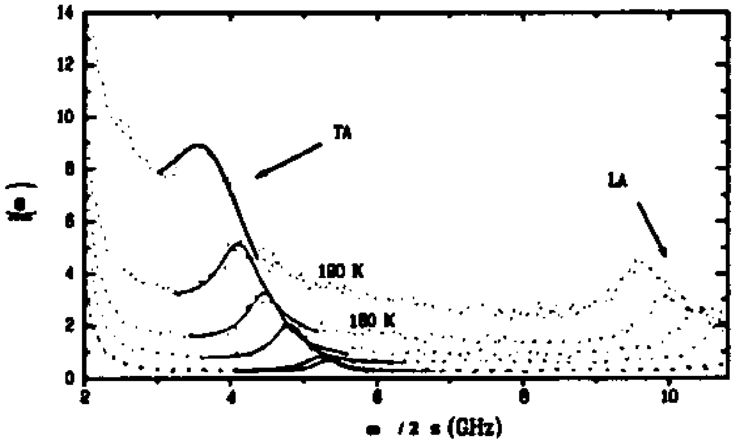

Fig. 4.27. I_{VH} 90° scattering Brillouin spectra at T= 190, 180, 170, 150, 145, and 125 K. The solid lines are fits of the data.

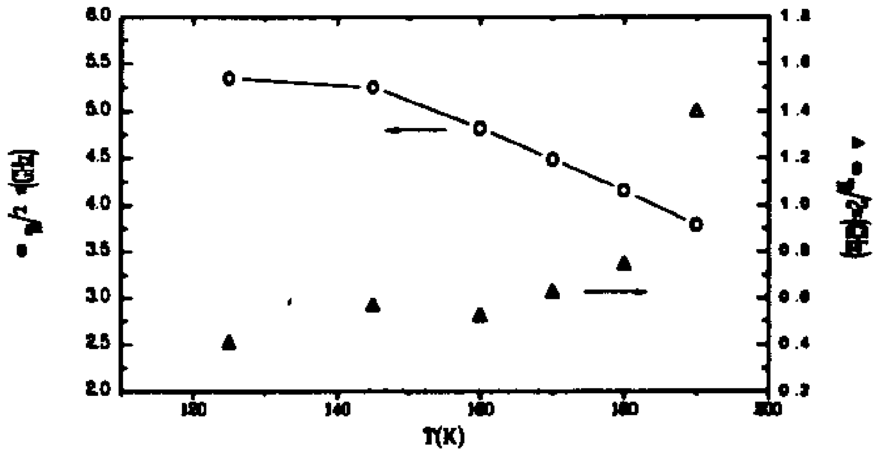

Fig. 4.28. The TA mode peak frequency (o) and line width (Δ).

A remarkable result is that the transverse mode remains underdamped well above T_g. Since the mode is very weak, accurate measurements of linewidth and intensity are

A remarkable result is that the transverse mode remains underdamped well above T_g. Since the mode is very weak, accurate measurements of linewidth and intensity are difficult in this system. The transverse acoustic velocity V_{TA} can be extracted from the frequency shift by $\omega_{TA} = V_{TA}\, k\sin(\theta/2)$. k is the wave-vector of scattered light.

The viscous relaxation time τ of the primary α relaxation can be related to η through the Maxwell equation $\tau = \eta / G_\infty$. G_∞ is the high-frequency shear modulus which could be obtained by extrapolating $G = \rho V_{TA}^2$ to high temperature.

F. BOSON PEAK

The broad Boson peak or microscopic band located around 1.2 THz in fig. 4.2 is a general feature of glassforming materials. It is nearly temperature independent. Despite its apparent universality and the large number of experimental and theoretical publications about it, the origin of the Boson peak remains unclear. A few different explanations have been proposed to explain the origin of the Boson peak.

In the past, the Martin-Brenig theory [76] proposed a disordered-crystal model. The model predicts that the low frequency spectrum, due to acoustic modes, follows $I(\omega) \propto \omega^2$ and the Boson peak position is determined by the correlation length of the static disorder. However, this model fails to correctly predict the depolarization ratio and the intensity of the spectra [77].

The MCT microscopic model relates the Boson peak to the characteristic liquid frequency Ω_q that is determined by the static structure factor S(q) and the thermal velocity. A light scattering study of this model was presented [77].

The molecular vibration model relates the Boson peak to the internal vibrational modes of a molecular crystal. The disordered structure of the glass perturbs the external vibrational modes and results in the broad Boson peak. This intrinsic relation has been studied in the molecular glassformer salol by using Raman scattering. The double-peak feature of the Boson peak in supercooled liquid salol corresponds quite closely with the observed vibrational mode of crystalline salol [15].

G. SIMULTANEOUS PHOTON CORRELATION AND DIELECTRIC EXPERIMENT ON SALOL

1. α-relaxation scale universality

The physical properties of a material depends on its structure. The structural relaxation can be studied by various techniques. Although neutron scattering, light scattering, ultrasonic and dielectric measurement etc. explore different physical variables, the corresponding spectra show some common features. The relaxation times τ obtained from the experiments depend on the temperature sensitively and all show similar anomalous behavior with extremely strong temperature dependence when the temperature is in the supercooled region. The strong temperature dependence of τ_α makes it difficult to accurately compare results obtained in different experiments.

MCT predicts that for any two measurements of the relaxation time, τ_A and τ_B, one finds

$$\tau_A(T)/\tau_B(T) = C_{AB}. \tag{4.6}$$

where C_{AB} is temperature independent. This is the universality of time scale prediction. The universality of time scale suggests that all α-relaxation dynamics of different variables have the same physical origin.

Various methods have been used to explore if there is a common relaxation dynamics and how it is coupled to different physical variables, such as the study performed on CKN [78].

To gain an understanding of this problem requires accurate values of the relaxation time. Fig. (4.29) shows τ_α values of salol from different measurements. These data indeed indicate that τ_α obtained from different measurements seems to follow a smooth function. However, due to the sensitive temperature dependence of τ_α, it is extremely difficult to compare τ_α values from different experiments to tell if they obey the universality prediction. (We also note that τ_α extracted from recent LA Brillouin scattering experiments fall below this curve as for PC [18]).

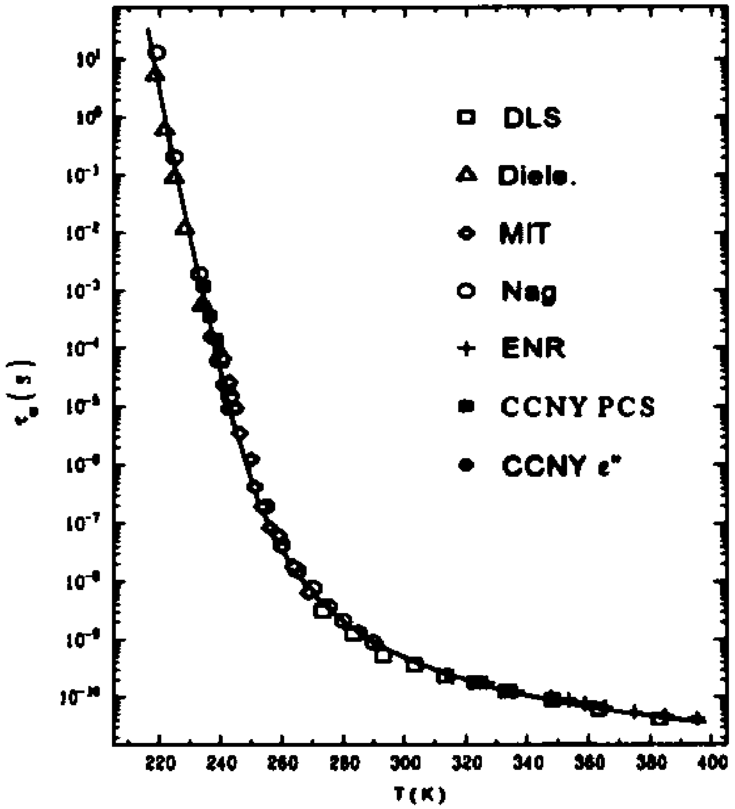

Fig. 4.29 The τ(*T*) values of salol measured by (□) DLS [15], (Δ) PCS by Sidebottom and Sorensen [79], (◆) forced light scattering [80], (o) dielectric measurements by Dixon et al. and Nagle et al. [71], (+) Brillouin scattering by Enright & Stoicheff [81], (■, and ●) simultaneous PCS and dielectric measurement of this work respectively. The line is guide for eye. All data follow the same trend, but small differences are masked by the logarithmic scale.

2. Experiment and Results

This experiment is designed to study α-relaxation time scale universality. We designed a sample cell which could be used to measure both the dielectric susceptibility and the light scattering correlation function simultaneously in a common temperature environment. The structure of the sample cell and experimental procedure are described section III.B.8. The dielectric relaxation time $\tau_{\alpha d}$ determined from the dielectric data and the light scattering relaxation time $\tau_{\alpha,pcs}$ determined from the photon correlation function were compared to test the universal time scale prediction.

Restrictions set by the measurement ranges of the two instruments limited the temperature interval common to both techniques to 234K to 242K. To study the relation between the relaxation times determined from the two measurement, both the dielectric spectrum and photon correlation function data are fitted with the stretched exponential model

$$F(t) = B\cdot\exp[-(t/\tau_{\alpha,PCS})^{\beta}]. \tag{4.7}$$

The imaginary part of dielectric constant ε"(ω) is fitted with

$$\varepsilon''(\omega) \propto \omega F.T.[(F(t)] \tag{4.8}$$

where F.T. is the Fourier transform of F(t). The fitting parameters are $\tau_{w\varepsilon}$, β_ε, and an amplitude factor B. The fitting range is the full width of the peak at half amplitude. The results of the fitting is shown in fig. (4.30). The spectra are essentially consistent with the measurement of Nagel [71] except that there is a small temperature shift, which presumably results from temperature calibration of the cryostat.

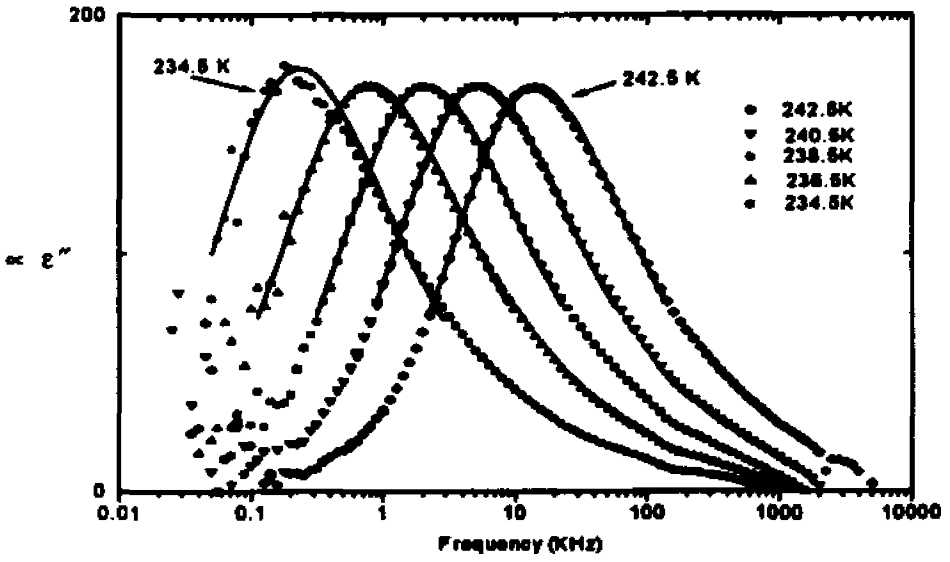

Fig. 4.30 Dielectric data and fits for 5 temperatures. Points are experimental data and the solid lines are fitted function.

The photon correlation data obtained with I_{VV} polarization shown in fig. 4.31 were analyzed, assuming the homodyne case; the data C(t) are fit with

$$(C(t)-C(\infty))/\,C(\infty) = F(t)^2. \tag{4.9}$$

with F(t) given by eq. (4.7). τ_ω, β_{pcs}, and B are fitting parameters. The results for the fitting are shown in fig. (4.31).

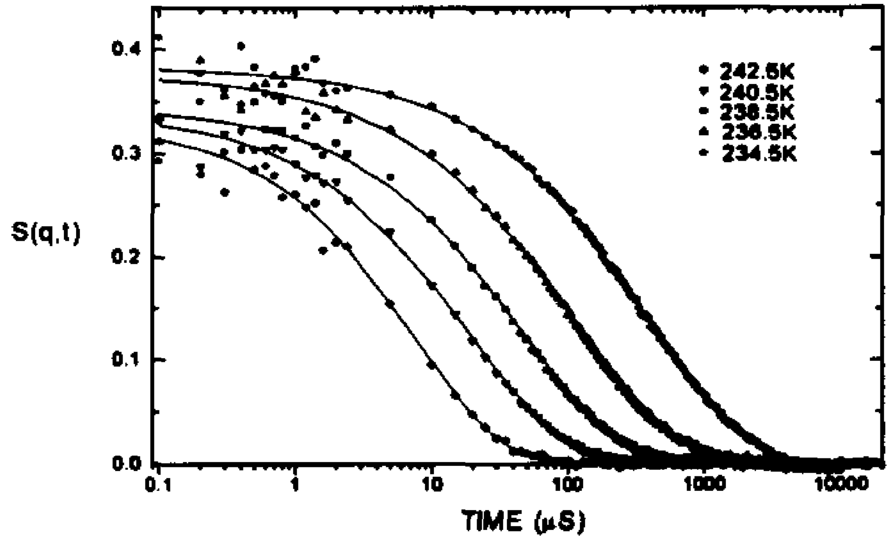

Fig. 4.31 PCS data and fits for 5 temperatures corresponding to the temperatures of the dielectric measurement. The points are experimental data and the solid lines are fitted functions.

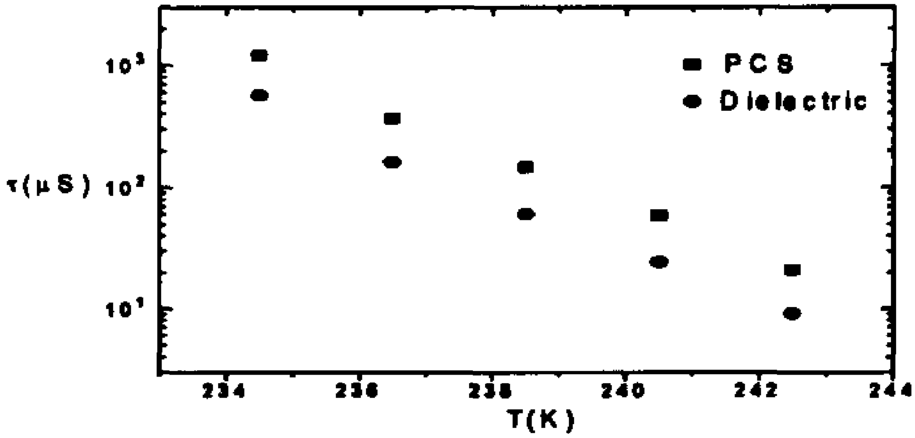

Fig. 4.32 τ_{pcs} and τ_ε vs. temperature.

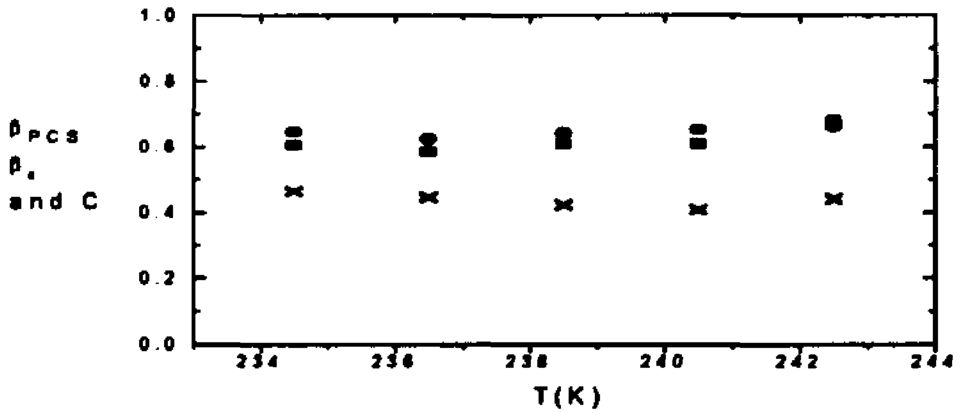

Fig. 4.33 β_{pcs} (•)and β_t (•), and the ratio $C=\tau_t/\tau_{pcs}$ (×) obtained from the measurements.

Fig. (4.32) shows the $\tau_{\alpha,t}$, $\tau_{\alpha,pcs}$ values from the fits to both sets of data. The almost equal separation between τ_{pcs} and τ_t implies a constant proportionality factor between them as predicted by eq. (4.6). Fig. (4.32) shows β_t, β_{pcs} and the relaxation time ratio $C_{pcs,t}$

.

The β values obtained from the two measurements are nearly temperature-independent and they agree with previously reported dynamic light scattering (DLS) [15] and PCS studies [77] . The ratio $C_{t,pcs}$ is found to be ~ 0.4 and is constant in the measured temperature region. This supports the universality of time scale prediction of MCT, although only in a limited temperature range.

To further compare the results of these two measurements, two α-peaks for temperature 242.5 K and 236.5 K were constructed by using the fitted parameter $\tau_{\alpha,pcs}$ and

β_{pcs} and were plotted in fig. (4.34) with the dielectric results for spectra of 236K and 240K. The constructed PCS α-peaks are very similar to the dielectric peaks except that the peaks position are shifted.

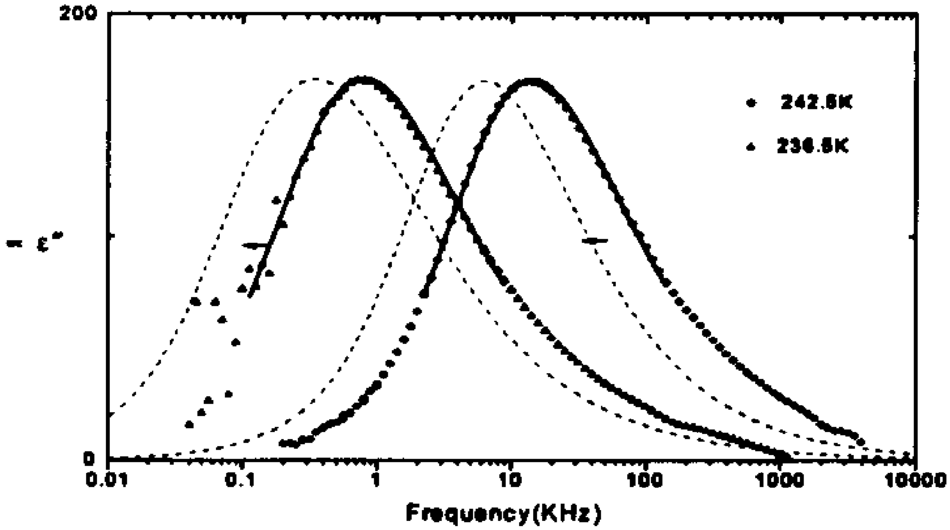

Fig. 4.34. Comparing the ε"(ω) peak and the constructed PCS α-peak by using the parameters obtained in fitting PCS data. The points are dielectric data, the solid lines are fits of dielectric spectra, and the dotted lines are calculated α-relaxation spectra.

It is often assumed that "structural relaxation" represents an intrinsic process in any given material and should therefore not depend on the particular experimental technique used to study it. In the context of MCT, however, structural relaxation is viewed as the slow fluctuations associated with the density fluctuation modes, as indicated in Eq. (2.6). The primary contribution to m(t) is $V^{(2)}$. For probes with $q \to 0$, Eq. (2.6) becomes

$$m_x(t) = \Sigma_q \, C_x(q) \, \Phi_q(t) \, \Phi_{-q}(t), \tag{4.10}$$

where the subscript x refers to the specific probe. Because the coupling constants $C_x(q)$ will, in general, depend on the probe, the weighted average over pairs of modes in Eq. (4.10) need not produce the same m(t) for all probes. Therefore the relaxation rates from these two experiments may have different values, but they will change the same way with temperature.

V. CONCLUSIONS

A. DEPOLARIZED LIGHT SCATTERING STUDY: TWO VERSIONS OF MCT

In this experimental study we used depolarized light scattering spectroscopy, Brillouin spectroscopy, ultrasonic measurement, dielectric response measurement and photon correlation spectroscopy to test the predictions of MCT. Two fragile glassforming materials, PC and salol, were studied. The spectra obtained revealed many features common to fragile glassforming material.

1. Depolarized light-scattering

Comparing first-order light scattering with neutron scattering, light scattering explores the long wavelength limit of the dynamic structure factor $S(q, \omega)$ while neutron scattering can study a large range of q values. Depolarized near-backscattering spectroscopy suppresses both LA and TA Brillouin components, allowing weak second order light scattering from pairs of q', q-q' modes and scattering from the rotational dynamics to be observed. It provides considerably better signal-to-noise ratios than neutron scattering measurements. The composite $\chi''(\omega)$ spectra from 0.3 GHz to 4 THz frequency are especially useful for studying the glass transition since (i) they cover the whole dynamic region of the α- and β- relaxation for $T > T_c$, and (ii) they revealed the evolution of the α-peak with changing temperature, therefore the relaxation time τ_α and the stretching of the α-relaxation process could be quantitatively determined over a large temperature range.

Data were analyzed by non-linear least squares fitting programs on mainframe computers. Most analyses have employed the idealized version of the theory which produced qualitatively good fits, confirming many of the MCT predictions. But the fits also indicated some disagreement for temperatures near and below the crossover temperature T_c. Analysis with the extended MCT produced substantial improvement in the fits, confirming the importance of the current (or hopping) terms neglected in the original idealized version of the theory.

2. β-relaxation

Data analysis of $\chi''(\omega)$ spectra in the region of the minima for 190 K $\leq T \leq$ 270 K based on the interpolation equation of the idealized MCT (eq. (2.37)) produced acceptable fits with the exponent parameter $\lambda = 0.78$. Extrapolation of the scaling quantities $\omega_{min}{}^{2a}$ and $\chi''_{min}{}^{2}$ vs. T produced a first estimate of $T_c = 185 \pm 5$ K.

The β-relaxation master function was then constructed by using $\lambda = 0.78$ found in the interpolation analysis. Scaling the $\chi''(\omega)$ spectra minima region onto the master function confirmed the λ value and indicated that λ falls between 0.75 and 0.81. The scaling quantities $\omega_{\sigma\text{-}}(T)$ and $\chi_{\sigma\text{-}}(T)$ were determined. Extrapolation of $\omega_{\sigma\text{-}}(T)$ and $\chi_{\sigma\text{-}}(T)$ to zero produced $T_c = 186 \pm 3$ K.

For $T < T_c$ the 'knee" predicted by the idealized MCT was not observed in PC. The data processing was therefore performed by comparing the slope of the data with the slope of the computed master function $\chi_+''(\omega)$. This analysis produced an estimate of T_c = 190 K for $T < T_c$, which is reasonably consistent with the result of the $T > T_c$ analysis within the experimental error.

Discrepancies in the low frequency part of the $\chi''(\omega)$ spectra for temperatures close to and below T_c were observed, which suggests that the idealized MCT is not complete.

3. α-relaxation

The α-relaxation peak of the $\chi''(\omega)$ susceptibility spectra exhibits rapid slowing down with decreasing temperature. The α peaks were fitted with a stretched exponential function. The temperature dependences of the α peak frequency ω_α and the stretching exponents β_K were deduced.

The resulted ω_a vs. T follows the power-law prediction of MCT. $\omega_a^{1/\gamma}(T)$ shows a linear temperature dependence and extrapolation to zero led to the estimate $T_c = 185 \pm 3$ K.

The stretching parameter β_k was found to be ~ 0.78 and is temperature-independent from 210 K to 350 K. This implies that the α-relaxation dynamics obey the time-temperature superposition principle in this temperature range as predicted by MCT. The CSPT prediction of β=1 at high temperature was not observed.

4. Extended MCT study

The β minimum region of the $\chi''(\omega)$ spectra was further analyzed using the extended MCT. The numerical solution of the β correlator equation of the extended MCT was used as the theoretical function in the non-linear least squares fitting of the β minimum region. The fits provided significant improvement for the fits of the low frequency region of the spectra around T_c.

The global fitting of the $\chi''(\omega)$ spectra determined the optimized critical exponent $a = 0.27$. $\sigma(T)$ determined by these fits shows a linear behavior as predicted by the theory. Tc determined from $\sigma \propto (T-T_c)$ is 187 ± 3 K, which agrees with the idealized MCT analysis very well. $\delta t_0(T)$ was found to follow an Arrhemius law. The transition region ΔT

extends over ~18 K which is similar to the result for salol but is much smaller than CKN [21]. The fitting also found that $h_u(T)$ factor depends on temperature, as predicted by the extended MCT.

5. The critical temperature T_C

The crossover temperature T_c is indicated by a variety of anomalies of the spectrum when approached from either below or above. It marks the transition from liquid-state dynamics to glass-state dynamics. The existence of a characteristic temperature $T_c = 187 \pm 5$ K for PC was confirmed from the above MCT analyses of α- and β- relaxation spectra. This value is consistent with the results found from neutron scattering, dielectric measurements, and viscosity measurements. It was found that $T_c > T_g$, which agrees with the results of previous investigations of many fragile glassformers.

By comparing these results with our previous studies of CKN and salol, we conclude that the simple molecular glass former PC follows the same crossover pattern, suggesting that the scaling behavior observed in these materials may well be universal for fragile glass-forming materials.

6. Comparison of PC results with other glassforming materials

The depolarized light scattering spectra of PC described in this thesis revealed the two-step relaxation process and its evolution with temperature during the liquid-glass transition. The slowing down of the α-relaxation and the development of the β-relaxation region with decreasing temperature are the common features observed in the dynamics of glassforming materials. These features have also been observed in our studies of CKN and salol. The spectra of OTP also exhibit the similar characteristics. These studies show that T_c is above T_g. The parameters of the MCT analysis for these materials are summarized in the following table.

Table V. MCT analysis parameters of some glassforming materials

Material	Fragility	T_g(K)	T_c(K)	T_m(K)	T_c-T_g	a	b	λ	β
CKN	93	333	378	~438	45	0.27	0.46	0.81	0.55
Salol	79	218	256	315	38	0.33	0.64	0.71	0.84
PC	104	160	187	218	27	0.29	0.50	0.78	0.77
OTP	81	243	290	329	47	0.31	0.52	0.73	0.60

B. POLARIZED BRILLOUIN SCATTERING STUDY: GENERALIZED HYDRODYNAMICS THEORY

Polarized Brillouin scattering experiments were performed as part of our investigation of the supercooled liquid dynamics of PC, and also in an attempt to elucidate the result reported by Elmroth et al. in which T_c found from a Brillouin scattering experiment was inconsistent with neutron scattering results.

1. Memory function models

Conventional Brillouin scattering has primarily explored the longitudinal and transverse acoustic modes and their interaction with primary α-relaxation. In this experiment, the LA Brillouin spectra of PC were fitted with generalized hydrodynamic theory. Three different relaxation memory function models, the CD model, empirical model and hybrid model were used in order to deduce the non-ergodicity factor to determine T_c. However, it was found that the PC spectra could not be adequately described by either the CD model or empirical memory function due to the fact that the primary relaxation time τ_α determined from the depolarized spectra is about five times longer than that of the relaxation process coupling to the longitudinal acoustic modes. We attempted to fit the spectra with a hybrid memory function which would approximate the function predicted by MCT, but the results were inconclusive.

In this study and other reports, it was found that the polarized spectra could be accurately described by generalized hydrodynamic theory with a single relaxation time structural relaxation process or essentially any other form of relaxation function. It is therefore hard to extract meaningful information from this kind of study. At this point we tentatively conclude that the determination of T_c from Brillouin scattering experiments is not generally reliable.

C. PCS AND DIELECTRIC LOSS SPECTROSCOPY STUDY OF THE α TIME-SCALE-UNIVERSALITY PREDICTION

The simultaneous measurement of dielectric loss spectrum and photon correlation spectrum was carried out in order to test the universality of α-relaxation time scale prediction of MCT. The result shows that the relaxation times determined from these two techniques have similar temperature dependence, differing only by a constant factor. This result suggests that these two relaxation processes are coupled. It supports the MCT point of view that different physical variables only project out different components of the same underlying structural relaxation modes.

D. CONCLUDING REMARKS

In this thesis I have presented detailed light-scattering studies of the liquid-glass transition in Propylene Carbonate designed to test the prediction of MCT. In these studies, I have carried out for the first time a systematic fit of the extended MCT using global nonlinear least-squares fitting procedures. Before concluding, it seems worthwhile to briefly state how these studies and previous related experiments bear on the overall question of the liquid- glass transition.

It has been understood for many years that in a liquid each molecule is somewhat localized in a cage formed by its immediate neighbors, so that it executes local vibrational motion before finding a path out of the cage leading to long-distance transport motion. It is this long-range motion that slows down drastically as the liquid-glass transition is approached. The local motion within the cage, resembling a zone-boundary acoustic phonon with strong damping, is relatively insensitive to temperature. MCT finds another mesoscopic time range between the fast microscopic and slow transport regimes in which the beta-relaxation dynamics take place. Computer simulations have indicated that the dynamics involved correspond essentially to collective rearrangements of the cage. MCT makes its strongest predictions about the dynamics in this region. These predictions, based on asymptotic expansions about the singularity associated with the ergodic-nonergodic transition at Tc, are very clear in the idealized theory but inconsistent with experiments. Therefore, the inclusion of hopping processes as done in the extended theory, is necessary for realistic comparisons. So far, however, extended MCT analyses have been carried out for only three materials: the mixed salt Calcium Potassium Nitrate (CKN), and the molecular glassformers Salol and PC. It is obviously desirable to do further studies on other materials so that the systematics of the liquid-glass transition can be further clarified.

In this work, many central predictions of the MCT have been verified experimentally, but others remain to be tested. In particular, the form of the $\chi''(\omega)$ spectra at temperatures below T_c has not yet been fully explored. Nevertheless, the physical mechanism embodied in the MCT appears to control the dynamics of supercooled liquids including the detailed form and temperature dependence of the susceptibility spectra, the existence of a crossover singularity, and the two-power-law decay. It therefore seems likely that the MCT does correctly describe the essential physics of supercooled liquid dynamics.

Finally, we note that the origin of the depolarized scattering analyzed in this work is still uncertain. In a recent study of salol we found that second-order DID scattering from pairs of density fluctuation modes is much weaker than first-order scattering from orientation fluctuations. The relative importance of these two mechanisms for PC has not yet been determined.

MCT predicts that all dynamical processes that couple to the density should exhibit dynamical behavior characterized by the same β-correlator G(t) in the vicinity of T_c. This prediction justifies our data analysis based on the asymptotic results of MCT. Detailed analysis of the orientational dynamics in supercooled liquids including translation-rotation interactions are currently in progress which will allow future data analysis to be compared directly to actual microscopic predictions of MCT.

BIBLIOGRAPHY

[1] C.A. Angell, J. Phys. Chem. Solids 49, 863 (1988).

[2] R. Bohmer, K.L. Ngai, C.A. Angell, and D.J. Plazek, J. Chem. Phys. 99, 4201 (1993)

[3] S.P. Das, G.F. Mazenko, S. Ramaswamy and J.T. Toner, Phys. Rev. Lett. 54, 118 (1985).

[4] W. Gotze, preprint, Liquids, Freezing and the Glass Transition, eds. J.P.Hansen et al, North-Holland, Amsterdam, (1989).

[5] S. S. Chang and A. B. Bestul, J. Chem. Phys. 56, 503 (1972).

[6] R. J. Greet and D. Turnbull, J. Chem. Phys. 47, 2185 (1967).

[7] C.A. Angell and L.M. Torell, J. Chem. Phys. 78, 937 (1983).

[8] R.D. Mountain, J. Res. NBS 70 A, 207 (1966).

[9] R. D. Mountain, Rev. Mod. Phys. 38, 205 (1966).

[10] M. Soltwisch, J. Sukmanowski and D. Quitmann, J. Chem. Phys. 86, 3207 (1987).

[11] Bengtzelius, W. Gotze and A. Sjolander, J. Phys. C17, 5915 (1984).

[12] E. Leutheusser, Phys. Rev. A 29, 2765 (1984).

[13] F. Mezei, W. Knaak, and B. Farago, Phys. Rev. Lett. 58, 571 (1987).

[14] G. Li, W.M. Du, X.K. Chen, H.Z. Cummins, and N.J. Tao, Phys. Rev. A 45, 3867 (1992).

[15] G. Li, W.M. Du, A. Sakai, and H.Z. Cummins, Phys. Rev. A 46, 3343 (1992).

[16] M. Fuchs, W. Gotze and A. Latz, Chem. Phys. 149, 185 (1990).

[17] M. Elmroth, L. Borjesson, and L.M. Torell, Phys. Rev. Lett. 68, 79 (1992).

[18] C. Dreyfus, M.J. Lebon, H.Z. Cummins, J. Toulouse, B. Bonello, and R.M. Pick, Phys. Rev. Lett. 69, 3666 (1992).

[19] G. Li, W.M. Du, J. Hernandez, and H.Z. Cummins, Phys. Rev. E 48, 1192 (1993).

[20] P. Taborek, R. N. Kleiman, and D. J. Bishop, Phys. Rev. B 34, 1835, (1986).

[21] H. Z. Cummins, W.M. Du, M. Fuchs, W. Gotze, S. Hildebrand, A. Latz, G. Li, and N.J. Tao, Light Scattering Spectroscopy of the Liquid-Glass Transition in C_aKNO_3 and Molecular Glass Salol: Extended Mode Coupling Theory Analysis, Phys. Rev. E, 47, 4223 (1993).

[22] J.R. Huck, G.A. Noyel, L.J. Jorat and A.M. Bondeau, J. Electrostatics 12, 221 (1982).

[23] L. Simeral and R.L. Amey, J. Phys. Chem. 74, 1443 (1970).

[24] A. Bondeau and J. Huck, J. Phys. (Paris) 46, 1717 (1985).

[25] E.A.S. Cavell, J. Chem. Soc. Faraday Trans. II 70, 78 (1974).

[26] G. P. Johari and M. Goldstein, J. Chem. Phys. 53, 2372 (1970).

[27] L.J. Jorat, G.A. Noyel, and J.R. Huck, IEEE Trans. Electrical Insulation 26, 763 (1991).

[28] R. Payne and I.E. Theodorou, J. Phys. Chem. 76, 2892 (1972).

[29] H. Cachet, M. Fekir, and J.C. Lestrade, Can. J. Chem. 59, 1051 (1981).

[30] C.P. Lindsay and G.D. Patterson, J. Chem. Phys. 73, 3348 (1980).

[31] A.K.M. Masood, R.A. Pethrick, A.J. Barlow, M.G. Kim, R.P. Plowiec, D. Barraclough, and J.A. Ladd, Adv. Molecular Relaxation Processes 9, 29 (1976).

[32] A. Schonhals, F. Hremer, A. Hofmann, E. W. Fisher, and E. Schlosser, Phys. rev. Lett. 70, 3459, (1993).

[33] S. Havriliak and S. Negami, J. Polym. Sci. Polym. Symp. 14, 89 (1966).

[34] L. Borjesson, M. Elmroth, and L.M. Torell, J. Non-cryst. Solids 131-133, 139 (1991).

[35] H.Z. Cummins, J. Hernandez, W.M. Du, and G. Li, Phys. Rev. Lett. 73, 2935 (1994).

[36] Schonhals et al. Phys. rev. Lett. 73, 2936 (1994).

[37] L. Borjesson and W. S. Howells, J. Non-cryst. Solids 131-133, 53 (1991).

[38] L. Borjesson, M. Elmroth, and L. M. Torell, Chem. Phys. 149, 209 (1990).

[39] J. R. Huck, G. A. Noyel and L.J. Jorat, Conf. Publ. Nb289 5th ICDMMA, Canterbury, IEE Loudon 328, (1988).

[40] A. Einstein, Ann. Phys. 33, 1275 Holland (1910).

[41] W. Hayes, and R. Loudon, in: Scattering of Light by Crystals, John Wiley & Sons, New York, (1978).

[42] W. Gotze and L. Sjogren, Rep. Prog. Phys. 55, 241 (1992).

[43] W. Gotze, J. Phys. Condens. Matt. 2, 8485 (1990).

[44] U. Bengtzelius, Phys. Rev. A 34, 5059 (1986).

[45] G. Buchalla, U. Dersch, W. Gotze and L. Sjogren, J. Phys. C 21, 4239 (1988).

[46] W. Gotze, Z. Phys. B 56, 139 (1984).

[47] S.P. Das and G.F. Mazenko, Phys. Rev. A 34, 2265 (1986).

[48] W. Gotze and L. Sjogren, J. Phys. C 21, 3407 (1988).

[49] W. Gotze and L. Sjogren, Z. Phys. B65, 415 (1987).

[50] M. Fuchs, W. Gotze, S. Hildebrand, and A. Latz, J. Phys. Condens. Matt. 4, 7709 (1992).

[52] M. Fuchs, W. Gotze, I. Hofacker and A. Latz, J. Phys. Condens. Matt. 3, 5047 (1991).

[53] B. J. Berne and R. Pecora, Dynamic Light Scattering, Wiley, New York, (1976).

[54] J. D. Jackson Classical Electrodynamics 2nd Edition John Wiley & Sons, Inc. New York, (1975).

[55] H.Z. Cummins, G. Li, and W. M. Du, Phys. Rev. E. (in press) (1995).

[56] N.J. Tao, G. Li and H.Z. Cummins, Phys. Rev. B 43, 5815 (1991).

[57] M. Born and E. Wolf, "Principles of Optics" 5th ed. Pergamon Press, Oxford, (1975).

[58] D.S. Bedboroagh and D. A. Jackson, J. Phys. E. Instrum. 11 473 (1978).

[59] J. R. Sandercock, in "Proc. 2nd Int. Conf. on Light Scattering in Solids" edited by M. Balkanski, 9 (1971).

[60] J. R. Sandercock, Solid State Commun. 26 547 (1978).

[61] J. Toulouse and C. launay, Rev. Sci. Instrum. 59, 492 (1988).

[62] J. Toulouse, 1987 Ultrasonoc Symposium Proceedings IEEE, 407, (1987).

[63] G. L. Petersen, B. Chick, and W. Junker, 1975 Ultrasonic Symposium Proceedings IEEE Cat. #75 CHO 994-4SU.

[64] W. Steffen, A. Patkowski, H. Glaser, G. Meier, and E.W. Fischer, Phys. Rev. E (to be published).

[65] M. kiebel, E. Bartsch, O. Debus, F. Fujara, W. Petry, and H. Sillescu, Phys. Rev. B. 45, 10301 (1992).

[66] B. Frick, B. Farago and D. Richter, Phys. Rev. Lett. 64, 2921 (1990).

[67] D. Richter, B. Frick and B. Farago, Phys. Rev. Lett. 61, 2465 (1988).

[68] F. Fujara and W. Petry, Europhys. Lett. 4, 921 (1987).

[72] W.M. Du, G. Li, and H.Z. Cummins, Light Scattering Study of Propylene Carbonate by Extended Mode Coupling Theory, APS annual meeting (1994).

[73] L. Sjogren, Z. Phys. B 79, 5 (1990).

[74] M. Fuchs, H.Z. Cummins, W.M. Du, W. Gotze, A. Latz, G. Li, and N.J. tao, Philosophical Magazine B. 75, 771, (1995).

[75] G. Floudas, J.S. Higgins and G. Fytas, J. Chem. Phys. 96, 7672 (1992).

[76] A.J. Martin and W. Brenig, Phys. Status Solid B 64, 163 (1974).

[77] N. J. Tao, G. Li, and H. Z. Cummins, Phys. Rev. B 45, 686 (1992).

[78] M. Grimsditch and L. M. Torell, in Dynamics of disordered Materials, D. Richter et al. Editors, Springer Verlag, Berlin 196 (1989).

[79] D.L. Sidebottom and C.M. Sorensen, Phys. Rew. B 40, 461 (1989).

[80] Y. Yang and K.A. Nelson, Phys. Rev. Lett. 74, 4883 (1995).

[81] G.D. Enright and B.P. Stoicheff, J. Chem. Phys. 64, 3658 (1976).